

WASM: Minerals, Energy and Chemical Engineering

**Fundamental Study of CO<sub>2</sub> Adsorption from  
Natural Gas using Activated Carbon**

Allan Hua Heng Sim  
0000-0003-0168-171X

This thesis is presented for the Degree of  
Doctor of Philosophy  
of  
Curtin University

January 2023



# Declaration

To the best of my knowledge and belief this thesis contains no material previously published by any other person except where due acknowledgment has been made. This thesis contains no material which has been accepted for the award of any other degree or diploma in any university.

*Allan Sim*

Signature: .....

Name: Allan Sim Hua Heng

Student ID: 14358625

Date: 27.01.2023





# Abstract

This proposed PhD project focuses on addressing the fundamental mechanism of carbon dioxide ( $\text{CO}_2$ ) adsorption within activated carbon (AC), which plays an important role in natural gas purification. A better understanding of the mechanism is necessary to develop  $\text{CO}_2$  adsorption and separation technologies in the natural gas industry based on the AC. The AC possesses complex physical structure and chemical properties, including wide pore size distributions and surface heterogeneity. Thus, it is difficult to understand the underlying mechanisms.

With the development of computational technology, molecular simulation has gained increasing application in investigating the mechanisms of gas adsorption in nanoporous materials, which can provide a microscopic perspective on adsorption behaviours and can be important compensation to experimental measurement, especially for certain conditions that are hard to accomplish. For instance, measurement of multicomponent adsorption in nanopores and preparation of the AC at a specified length with uniform pore sizes and structure. The main tool applied in this project is Monte Carlo simulation, with the Grand Canonical ensemble that could mimic the process of commonly used volumetric adsorption method in reality, and with the canonical ensemble that can be applied to obtain the thermodynamic properties with the selected potential models, which are critical for ensuring the reliability of the simulated results.

A systematic study of  $\text{CO}_2$  adsorption was conducted with the AC, which was constructed with simple but representative pore models (e.g. uniform slit pore, wedge pore, etc.). Adsorption behaviours of  $\text{CO}_2$  at subcritical conditions are firstly investigated in a wedge pore model. These insights can be useful information for natural gas purification under subcritical conditions hence facilitating the designing and optimizing of suitable carbon adsorbents. For a given wedge pore, there exists a critical temperature for the occurrence

of stepwise desorption. Low temperature facilitates the formation of ordered structures in the wedge pore and hence the steps of the desorption branch. As temperature increases, disordered structures are likely to occur at the wide end and then proceed at the narrow end, until propagated to the entire pore. Moreover, having corrugation on the interior solid surface also results in different mechanisms due to the change in the actual pore size distribution and the interference to the force field inside the pore.

To ensure the reliability of the simulation results, the selection of a reliable CO<sub>2</sub> potential model is vital. A systematic Monte Carlo simulation was then conducted to evaluate the performance of two commonly used potential models of CO<sub>2</sub>, i.e. the simple 1C-LJ and the TraPPE 3C-LJ+3Q models, in different scenarios including bulk phase, adsorption on graphite surface and in carbonaceous pores. A special investigation on the occurrence of step-wised hysteresis in a wedge shaped pore has been observed with other simple gases. It reveals the consideration of shape and quadrupole of CO<sub>2</sub> plays an important role in the description of the phase equilibria and adsorption behavior, especially at temperatures below the triple point.

The adsorption of pure N<sub>2</sub>, CO<sub>2</sub>, CH<sub>4</sub> and their binary mixtures were eventually evaluated using the reliable CO<sub>2</sub> potential model compared with experimental data at 273 and 298K for the ACs. A uniform slit pore and a (equivalent pore volume) wedge pore simulated with GCMC, and the IAST method were used to predict the adsorbed amounts of each gas in the CO<sub>2</sub>/CH<sub>4</sub> and CO<sub>2</sub>/N<sub>2</sub> mixtures. The molecular simulation in the slit and wedge pore can predict the selectivity well. However, the IAST provided poor predictions, particularly at higher pressures. At high pressure, the combination of the slit pore model fitted the experimental data mostly well and agrees well with the IAST. However, at low pressure, the predictions of single and binary equilibria with a single wedge pore model showed better agreement with the experimental data and were comparable with those predicted using the IAST method. Therefore, the wedge pore model can be treated as an alternative model for representing the non-uniform pore size distribution in the AC.

# List of Publications

## Journal papers (\*Co-first author)

1. Liu\*, X., **AHH. Sim\***, and C. Fan. (2022) Low temperature adsorption of CO<sub>2</sub> in carbonaceous wedge pores: A Monte Carlo simulation study. *Adsorption*. <https://doi.org/10.1007/s10450-022-00363-x>
2. Liu\*, X., **AHH. Sim\***, and C. Fan. (2022) Effects of Potential Model of CO<sub>2</sub> on its Bulk Phase Properties and Adsorption on Surfaces and in Pores. *Molecular Simulation*, <https://doi.org/10.1080/08927022.2022.2086276>
3. **AHH. Sim**, X. Liu and C. Fan. (2022) Adsorptive Separation of Carbon Dioxide at Ambient Temperatures in Activated Carbon. *Carbon Capture Science & Technology*, <https://doi.org/10.1016/j.ccst.2022.100062>

## Conference papers

1. **AHH. Sim**<sup>°</sup>, and C. Fan. (2022). Binary Mixture Adsorption of CO<sub>2</sub>/CH<sub>4</sub> in Activated Carbon. The 31st Thai Institute of Chemical Engineering and Applied Chemistry Conference (TIChE), Thailand, March 15, 2022.  
<sup>°</sup>Award: Best conference oral presentation (TIChE 2022)
2. **AHH. Sim**, and C. Fan. (2022). Adsorption of CO<sub>2</sub>/N<sub>2</sub> in Activated Carbon. 19th Asian Pacific Confederation of Chemical Engineering (APCChE) Congress, Malaysia, Aug 9, 2022.

## Poster presentation

1. **AHH. Sim**, and C. Fan. (2022). Adsorption of CO<sub>2</sub>/CH<sub>4</sub> Mixtures in Activated Carbon. The 1<sup>st</sup> Annual WASM: MECE HDR Conference, Curtin University, Perth, July 22, 2022.



# Acknowledgements

My deepest appreciation to my principal supervisor, Dr. Chunyan Fan, for her support, endless patience, guidance, motivation and encouragement throughout this thesis. She gave me the freedom to perform my thesis and encouraged me to explore my possibilities of the research direction. She also has provided an opportunity to participate in an international event, which is beneficial for my research perspective. I am indebted to Dr. Chunyan Fan for her time spent supervising my study, for her effort in reviewing and revising my thesis and for her valuable suggestion and feedback. I gained all valuable skills, attitudes and knowledge from her and those positively influence my future research career. It was my pleasure to conduct this PhD study under her supervision. Following this, my sincere gratitude goes to Dr. Xiu Liu for her kind guidance, advice, and knowledge sharing about my thesis topic.

Moreover, I would like to express my sincere gratitude to my thesis chairperson, my co-supervisor and PhD milestones examiners: Prof. San Ping Jiang, Dr. Li Dong, Prof. Shaomin Liu and Dr. Arash Arami-Niya for their critical and constructive comments on the contents demonstrated in this thesis. Also, a massive appreciation goes to my friendly friends and colleagues: Manoj, Sweta, Shakir, Juntao, Yurong and many other student fellows studying at Curtin University for their support throughout my PhD candidature.

I would like to thank Curtin International Postgraduate Research Scholarship (CIPRS) for financial support during my PhD candidature. This PhD research project was supported by resources provided by the Pawsey Supercomputing Centre with funding from the Australian Government and the Government of Western Australia.

Finally, I would like to express my love and cares to my beloved family for their everlasting love and continuous encouragement throughout this thesis. I am so thankful to have you all in my life.



# Contents

<b>Declaration</b>	<b>iii</b>
<b>Abstract</b>	<b>v</b>
<b>List of Publications</b>	<b>vii</b>
<b>Acknowledgements</b>	<b>ix</b>
<b>List of Figures</b>	<b>xv</b>
<b>List of Tables</b>	<b>xxiii</b>
<b>1 Introduction</b>	<b>1</b>
1.1 Background and Motives . . . . .	1
1.2 Literature Review . . . . .	4
1.2.1 Potential models of CO <sub>2</sub> . . . . .	4
1.2.2 Bulk phase equilibria for CO <sub>2</sub> . . . . .	6
1.2.3 Adsorption of CO <sub>2</sub> in activated carbon . . . . .	7
1.2.4 Adsorption of CO <sub>2</sub> -containing mixture in activated carbon . . . . .	10
1.3 Thesis Objectives . . . . .	13
1.4 Thesis Organization . . . . .	14
<b>2 Theory and Simulation</b>	<b>15</b>
2.1 Monte Carlo Simulation . . . . .	15
2.1.1 Grand canonical Monte Carlo . . . . .	16
2.1.2 Bin-canonical Monte Carlo . . . . .	17
2.1.3 Isobaric-isothermal (NPT) . . . . .	19
2.2 Thermodynamic Property Calculations . . . . .	19
2.2.1 Potential energy . . . . .	19

2.2.2	Chemical potential . . . . .	23
2.2.3	Pressure . . . . .	23
2.2.4	Evaporation (sublimation) heat . . . . .	24
2.2.5	Surface tension . . . . .	25
2.2.6	Adsorption isotherm . . . . .	25
2.2.7	Isosteric heat . . . . .	27
2.2.8	Henry constant . . . . .	28
2.3	Selectivity in binary mixtures . . . . .	28
2.4	IAST . . . . .	29
2.5	Simulation Systems . . . . .	29
2.5.1	Adsorption systems . . . . .	30
<b>3</b>	<b>Adsorption of CO<sub>2</sub> in Wedge Pores</b>	<b>33</b>
3.1	Introduction . . . . .	33
3.2	Theory and Simulation . . . . .	34
3.2.1	Wedge pore model . . . . .	34
3.2.2	Potential model . . . . .	34
3.2.3	Monte Carlo simulation details . . . . .	34
3.3	Results and Discussion . . . . .	35
3.3.1	CO <sub>2</sub> adsorption in the reference wedge pore at 150K . . . . .	35
3.3.2	Effects of temperature . . . . .	38
3.3.3	Effects of pore length . . . . .	38
3.3.4	Effects of angle . . . . .	40
3.3.5	Effects of corrugation . . . . .	42
3.4	Summary . . . . .	48
<b>4</b>	<b>Effects of CO<sub>2</sub> Potential Model</b>	<b>49</b>
4.1	Introduction . . . . .	49
4.2	Theory and Simulation . . . . .	50
4.2.1	Potential models . . . . .	50
4.2.2	Simulation systems . . . . .	50
4.2.3	Monte Carlo simulation . . . . .	50
4.3	Results and Discussion . . . . .	51
4.3.1	VSE/VLE of CO <sub>2</sub> . . . . .	51
4.3.2	Adsorption on graphitic surface . . . . .	53
4.3.3	Adsorption in slit pores . . . . .	57
4.3.4	Adsorption in wedge pores . . . . .	60



---

4.4	Summary . . . . .	63
<b>5</b>	<b>Adsorptive Separation of CO<sub>2</sub></b>	<b>65</b>
5.1	Introduction . . . . .	65
5.2	Theory and Simulation . . . . .	66
5.2.1	Potential models . . . . .	66
5.2.2	Simulation systems . . . . .	66
5.2.3	Monte Carlo simulation . . . . .	66
5.3	Results and Discussion . . . . .	67
5.3.1	Activated carbon Norit R1 Extra . . . . .	67
5.3.2	Activated carbon Norit RB2 . . . . .	75
5.4	Summary . . . . .	82
<b>6</b>	<b>Conclusions and Recommendations</b>	<b>85</b>
6.1	Conclusions . . . . .	85
6.2	Recommendations . . . . .	87
	<b>References</b>	<b>89</b>
	<b>Appendices</b>	<b>107</b>
	<b>Appendix A Two Layers Two Humps</b>	<b>109</b>
	<b>Appendix B Two Layers Three Humps</b>	<b>111</b>
	<b>Appendix C Pore Size Distribution of Activated Carbon</b>	<b>115</b>
	<b>Appendix D Comparison of Potential Profiles</b>	<b>117</b>
	<b>Appendix E Reprinted with Permission</b>	<b>119</b>



# List of Figures

Figure 1.1.	IUPAC hysteresis loops classification (Thommes et al. 2015). . . . .	7
Figure 1.2.	de Boer classification for hysteresis loops (de Boer 1973). . . . .	8
Figure 1.3.	Schematic representations for an activated carbon (Rosalind 1951) (a) non-graphitizing carbon; (b) graphitizing carbon; (c) slit pore model; (d) wedge pore model. . . . .	9
Figure 2.1.	Schematic diagram of a phase equilibria system. . .	30
Figure 2.2.	Schematic diagram of a graphitic surface. . . . .	31
Figure 3.1.	Schematic diagram of a corrugated wedge pore. . . .	34
Figure 3.2.	(a) Isotherm and (b) isosteric heat of 1C-CO <sub>2</sub> adsorption at 150K in the reference wedge pore of SH=2nm, L=10nm and $\alpha=5^\circ$ , with the lines as guide to the eye. . . . .	36
Figure 3.3.	Snapshots of evolution of CO <sub>2</sub> adsorption at 150K in the reference wedge pore of SH=2nm, L=10nm and $\alpha=5^\circ$ : (a) adsorption and (b) desorption. The points from A to J are as labelled in Figure 3.2. . .	37
Figure 3.4.	Isotherms of CO <sub>2</sub> adsorption at various temperatures in the reference wedge pore of SH=2nm, L=10nm and $\alpha=5^\circ$ with (a) absolute pressure in log scale and (b) reduced pressure. Isotherms in (b) for 155K, 160K, 173K, 194.7K and 216.6K have been shifted up by $n \times 25$ kmol/m <sup>3</sup> , respectively. . . . .	39

Figure 3.5.	Snapshots at saturated pressures and various temperatures in the reference wedge pore of SH=2nm, L=10nm and $\alpha=5^\circ$ . . . . .	40
Figure 3.6.	Isotherm for CO <sub>2</sub> at 150K in the wedge pores of lengths 10 and 15nm, SH=2nm and $\alpha=5^\circ$ . . . . .	41
Figure 3.7.	Snapshots of (a) just after condensation; (b) at 15 kPa for CO <sub>2</sub> at 150K in wedge pore of lengths 10 and 15nm, SH=2nm and $\alpha=5^\circ$ . . . . .	41
Figure 3.8.	Isosteric heat curves for CO <sub>2</sub> adsorption at 150K (a) in the reference wedge pore ( $\alpha=5^\circ$ ) of SH=2nm and L=10nm, (b) in the corrugated pore with two double-layers humps grafted at the domains III and IV (see isotherm in Figure 3.13) . . . . .	42
Figure 3.9.	Isotherm for CO <sub>2</sub> at 150K in wedge pore of angles $\alpha = 1^\circ, 2.5^\circ$ and $5^\circ$ , SH=2nm, (a) L=10nm; (b) L=15nm. . . . .	42
Figure 3.10.	Snapshots at 10kPa and 150K in wedge pore of $\alpha = 5^\circ, 2.5^\circ$ and $1^\circ$ , SH=2nm, L=10nm. . . . .	43
Figure 3.11.	Isotherms of adsorption in pores with two pairs of double-layers humps grafted on the pore walls at domains and junctions. . . . .	44
Figure 3.12.	Isotherms of adsorption in pores with three pairs of double-layers humps grafted on the pore walls at different locations. . . . .	45
Figure 3.13.	Isotherms for CO <sub>2</sub> at 150K in wedge pore having two humps with two layers at domains (well depth = 28K and 0K). . . . .	47
Figure 3.14.	Snapshots of CO <sub>2</sub> adsorption at 150K in the wedge pore containing two layers two humps (well depth = 0K) corresponding to the points A to J in Figure 3.13. The dashed lines are labelled at the same positions as in Figure 3.2, i.e. the positions of the junctions. . . . .	47

Figure 4.1.	Thermodynamic properties of 1C-LJ and TraPPE 3C-LJ potential models at various temperatures obtained with Bin-CMC as compared to the experimental data, (a) liquid (solid)–vapour coexistence curve in linear scale, (b) liquid (solid)–vapour coexistence curve in semi-log scale, (c) vapour pressure in linear scale, (d) vapour pressure in semi-log scale, (e) evaporation (sublimation) heat and (f) surface tension. Statistical uncertainties are smaller than the size of the symbols used in the above figures. . . . .	52
Figure 4.2.	Profile of solid-fluid potential energy versus the distance between the mass center of CO <sub>2</sub> molecule to the solid surface, 3C-LJ model is parallel to the surface to maximize the potential. . . . .	54
Figure 4.3.	Comparison of adsorption isotherms on graphitic surface at temperatures of (a) 194K and (b) 273K for both models and monolayer snapshots of CO <sub>2</sub> for (c) 1C-LJ model at 150K and (d) 3C-LJ model at 194K, both at P <sub>0</sub> . . . . .	55
Figure 4.4.	Comparison of adsorption isotherms (on a logarithmic scale) on graphitic surface at various temperatures for (a) 1C-LJ and (b) 3C-LJ models. . . . .	57
Figure 4.5.	Comparison of adsorption isotherms at 298K for 1C-LJ and 3C-LJ models in slit pores with the pore size of (a) 2 nm and (b) 3.5 nm. . . . .	58
Figure 4.6.	Comparison of isotherms at temperature T1 for 1C-LJ and 3C-LJ models in slit pores with the pore size of (a) 2 nm and (b) 3.5 nm. . . . .	59
Figure 4.7.	Comparison of adsorption isotherms at temperature T2 for 1C-LJ and 3C-LJ models in slit pores with the pore size of (a) 2 nm and (b) 3.5 nm. . . . .	60
Figure 4.8.	Comparison of adsorption isotherms for 1C-LJ and 3C-LJ models in the wedge pore at various temperatures: (a) 298 K, (b) T1, (c) T2. The pores are 8.5 nm in axial length. . . . .	61

- Figure 4.9. Snapshots of CO<sub>2</sub> molecules in the reference wedge pore at saturation vapor pressures for (a) 1C-LJ model (at temperatures below triple point) and (b) 1C-LJ (at temperatures above triple point). . . . . 61
- Figure 4.10. Isotherms of CO<sub>2</sub> adsorption corresponding to the reduced pressure for the reference wedge pore at various temperatures using (a) 1C-LJ model (triple point = 172K) and (b) 3C-LJ model (triple point = 216K). . . . . 63
- Figure 5.1. The chemical potential of CO<sub>2</sub> at 273K as functions of (a) pressure in log-scale; (b) density in linear scale. Circles are plotted from the EOS of Johnson et al. and the solid line is taken from NPT. . . . 67
- Figure 5.2. Pore size distribution of Norit R1 Extra and Sorbonorit B4 carbons, obtained by interpretation of argon adsorption at 87K using the current approach. The inset shows the PSD using the conventional infinite wall thickness model [Reprinted (adapted) with permission from T. X. Nguyen, S. K. Bhatia, Characterization of pore wall heterogeneity in nanoporous carbons using adsorption: the slit pore model revisited, *J. Phys. Chem B* 108 (37) (2004) 14032–14042. doi:10.1021/jp049048f. Copyright 2022 American Chemical Society]. . . . . 68
- Figure 5.3. Experimental data of pure N<sub>2</sub>, CH<sub>4</sub> and CO<sub>2</sub> on AC Norit R1E at  $T = 298\text{K}$  (Dreisbach et al. 1999). Prediction of data with the adsorption isotherms in a slit and wedge pore: (a) absolute pressure and (b) absolute pressure in log scale. . . . . 70
- Figure 5.4. The profile of pairwise interaction between two fluid molecules. For CO<sub>2</sub>, the axis of the two molecules lies in the same plane, and perpendicular to each other, the distance between two carbon atoms varied. 70

- Figure 5.5. The profile of the selected fluid molecular interact with the graphite surface, simulated with Bojan potential. For  $\text{CO}_2$ , the axis of the molecule lies parallel to the graphite surface, and the distance between the two changes by shifting the whole molecule above the surface. . . . . 71
- Figure 5.6. Adsorption isotherms of  $\text{CO}_2/\text{CH}_4$  mixture at  $T = 298\text{K}$  in a slit pore, wedge pore and predicted values from IAST for the pressures ranging from 93kPa to 6.077MPa, and the adsorbed amounts of  $\text{CO}_2$  and  $\text{CH}_4$  from their mixture [symbols: experimental data (Dreisbach et al. 1999), solid lines: theoretical model, red: total adsorbed amount of  $\text{CO}_2$  and  $\text{CH}_4$ , blue: adsorbed amount of  $\text{CO}_2$ , green: adsorbed amount of  $\text{CH}_4$ ]. . . . . 73
- Figure 5.7. Adsorption isotherms of  $\text{CO}_2/\text{N}_2$  mixture at  $T = 298\text{K}$  in a slit pore, wedge pore and predicted values from IAST for the pressures ranging from 93kPa to 6.077MPa, and the adsorbed amounts of  $\text{CO}_2$  and  $\text{N}_2$  from their mixture [symbols: experimental data (Dreisbach et al. 1999), solid lines: theoretical model, red: total adsorbed amount of  $\text{CO}_2$  and  $\text{N}_2$ , blue: adsorbed amount of  $\text{CO}_2$ , green: adsorbed amount of  $\text{N}_2$ ]. . . . . 74
- Figure 5.8. Selectivity of  $\text{CO}_2$  over  $\text{CH}_4$  or  $\text{N}_2$  at  $T = 298\text{K}$  on AC Norit R1E at approximately 50%  $\text{CO}_2$  with experimental data (Dreisbach et al. 1999) (symbols). 76

- Figure 5.9. Pore size distribution of Norit RB2, ROW 0.8 and ROX 0.8 carbons, obtained by interpretation of argon adsorption at 87K using the current approach. The inset shows the PSD using the conventional infinite wall thickness model [Reprinted (adapted) with permission from T. X. Nguyen, S. K. Bhatia, Characterization of pore wall heterogeneity in nanoporous carbons using adsorption: the slit pore model revisited, *J. Phys. Chem B* 108 (37) (2004) 14032–14042. doi:10.1021/jp049048f. Copyright 2022 American Chemical Society]. . . . . 77
- Figure 5.10. Experimental isotherms of the pure gases CO<sub>2</sub> and CH<sub>4</sub> on AC Norit RB2 at  $T = 273\text{K}$  (Goetz et al. 2006). Adsorption isotherms in a slit and wedge pore: (a) absolute pressure and (b) absolute pressure in log scale. . . . . 79
- Figure 5.11. Experimental isotherms of the pure gases CO<sub>2</sub> and CH<sub>4</sub> on AC Norit RB2 at  $T = 298\text{K}$  (Goetz et al. 2006). Adsorption isotherms in a slit and wedge pore: (a) absolute pressure and (b) absolute pressure in log scale. . . . . 79
- Figure 5.12. Adsorption isotherms of CO<sub>2</sub>/CH<sub>4</sub> mixture at  $T = 273\text{K}$  in a slit pore, wedge pore and predicted values from IAST for the pressures of 0.1, 0.5 and 1MPa, and the adsorbed amounts of CO<sub>2</sub> and CH<sub>4</sub> from their mixture [blue: total adsorbed amount of CO<sub>2</sub> and CH<sub>4</sub>, red: adsorbed amount of CO<sub>2</sub>, green: adsorbed amount of CH<sub>4</sub>]. . . . . 80
- Figure 5.13. Adsorption isotherms of CO<sub>2</sub>/CH<sub>4</sub> mixture at  $T = 298\text{K}$  in a slit pore, wedge pore and predicted values from IAST for the pressures of 0.1, 0.5 and 1MPa, and the adsorbed amounts of CO<sub>2</sub> and CH<sub>4</sub> from their mixture [blue: total adsorbed amount of CO<sub>2</sub> and CH<sub>4</sub>, red: adsorbed amount of CO<sub>2</sub>, green: adsorbed amount of CH<sub>4</sub>]. . . . . 81



Figure 5.14.	Selectivity of CO <sub>2</sub> over CH <sub>4</sub> at $T =$ (a) 273K and (b) 298K on AC Norit RB2 at approximately 20% CO <sub>2</sub> . . . . .	82
Figure A.1.	Snapshots for CO <sub>2</sub> adsorption at 150K in wedge pore having two humps located (a) at domains; (b) at junctions; SH=2nm, L=10nm and $\alpha=5^\circ$ . . . . .	110
Figure B.1.	Snapshots for CO <sub>2</sub> adsorption at 150K in wedge pore having three humps located (a) at domains; (b) at junctions; SH=2nm, L=10nm and $\alpha=5^\circ$ . . . . .	113
Figure C.1.	Reprinted (adapted) with permission from T. X. Nguyen, S. K. Bhatia, Characterization of pore wall heterogeneity in nanoporous carbons using adsorption: the slit pore model revisited, <i>J. Phys. Chem B</i> 108 (37) (2004) 14032–14042. doi:10.1021/jp049048f. Copyright 2022 American Chemical Society. . . . .	115
Figure D.1.	The comparison of the potential profiles of a single Lennard-Jones fluid particle with the conventional Steele potential model and the Bojan potential, which is composed of three graphene layers, and with the same length as the pore models applied in Chapter 5, i.e. L=8.5nm. . . . .	117
Figure E.1.	Reprinted (adapted) with permission from Xiu Liu, Allan Hua Heng Sim & Chunyan Fan Low temperature adsorption of CO <sub>2</sub> in carbonaceous wedge pores: a Monte Carlo simulation study. <i>Adsorption</i> (2022). <a href="https://doi.org/10.1007/s10450-022-00363-x">https://doi.org/10.1007/s10450-022-00363-x</a> . Copyright 2022 Springer Nature. . . . .	119
Figure E.2.	Reprinted (adapted) with permission from Xiu Liu, Allan Hua Heng Sim & Chunyan Fan (2022) The effects of potential model of CO <sub>2</sub> on its bulk phase properties and adsorption on surfaces and in pores, <i>Molecular Simulation</i> , <a href="https://doi.org/10.1080/08927022.2022.2086276">https://doi.org/10.1080/08927022.2022.2086276</a> . Copyright 2022 Taylor & Francis . . . . .	120

- Figure E.3. Reprinted (adapted) with permission. This article was published in Carbon Capture Science & Technology, Vol. 4, Allan Hua Heng Sim, Xiu Liu & Chunyan Fan, Adsorptive Separation of Carbon Dioxide at Ambient Temperatures in Activated Carbon, 100062, Copyright Elsevier (2022). . . . . 121

# List of Tables

Table 1.1.	Potential model parameters for CO <sub>2</sub> (Hammonds et al. 1990; Murthy et al. 1983; Potoff and Siepmann 2001; Wu et al. 2015). . . . .	5
Table 2.1.	Potential model parameters for CH <sub>4</sub> and N <sub>2</sub> (Ravikovitch et al. 2001; Sun et al. 1992). . . . .	21
Table 3.1.	Saturated vapour pressures of 1C-LJ CO <sub>2</sub> at various temperatures calculated with VLE/VSE simulations (simulated triple point = 172K) and with available experimental data (Spencer et al. 1958; Terlain and Larher 1983). . . . .	35
Table 4.1.	The corresponding temperatures used for 1C-LJ and 3C-LJ potential models. . . . .	53
Table 4.2.	Saturation vapour pressures of CO <sub>2</sub> at various temperatures for 1C-LJ potential model (Triple point = 172K). . . . .	53
Table 4.3.	Saturation vapour pressures of CO <sub>2</sub> at various temperatures for 3C-LJ potential model (Triple point = 216K). . . . .	53
Table 5.1.	Experimental composition of the gas mixture containing CO <sub>2</sub> and CH <sub>4</sub> (Dreisbach et al. 1999). . . . .	71
Table 5.2.	Experimental composition of the gas mixture containing CO <sub>2</sub> and N <sub>2</sub> (Dreisbach et al. 1999). . . . .	72



# Chapter 1

## Introduction

This chapter mainly discusses the background and motivation for this PhD thesis, which aimed to provide a better understanding of the mechanism of CO<sub>2</sub> adsorption in the activated carbon (AC) that is associated with its separation and removal from natural gas mixtures. Background to CO<sub>2</sub> adsorption and separation from natural gas using the AC is described in Section 1.1. A literature survey is presented in Section 1.2 including the review of the adsorption system containing CO<sub>2</sub> and AC adsorbents studied with MC simulation. Research objectives are presented in Section 1.3. Thesis organization is briefed in Section 1.4.

### 1.1 Background and Motives

The primary energy supply has relied heavily on carbonaceous fuels, including the typical fossil energies: coal, petroleum, and conventional and unconventional natural gas (IEA 2022). As a result, the pollutants emitted from power plants, mobile energy systems, and industrial factories pose significant environmental challenges to human health and safety. The pollutants include carbon dioxide (CO<sub>2</sub>), methane (CH<sub>4</sub>), SO<sub>x</sub>, NO<sub>x</sub>, mercury, and particulate matter emissions. In addition, the CO<sub>2</sub> and CH<sub>4</sub> are the primary greenhouse gases responsible for global climate change and global warming (IEA 2022; IPCC 2021). Reducing greenhouse gases emissions, particularly CO<sub>2</sub> emissions, has been heightened in both academia and industry in recent years (IPCC 2021; Siegelman et al. 2021; Vorokhta et al. 2021).

Among those fossil fuels aforementioned, natural gas is more energy efficient, clean-burning and economical energy source. However, in actual fact,

raw natural gas cannot be delivered to end-users because of contaminants and large amount of inert gases (Speight 2019). Therefore, treatments must be taken to meet the minimum quality standard of pipeline transmission and distribution companies. Furthermore, some acid impurities such as CO<sub>2</sub> or H<sub>2</sub>S must also be avoided to prevent corrosion of the pipelines. Among the different impurities, CO<sub>2</sub> has the largest contribution (Kidnay et al. 2019; Speight 2019). The maximum level permitted of CO<sub>2</sub> is between 2%–4% depending on the standard and regulations of the country. The high content of CO<sub>2</sub> significantly reduces the caloric content of natural gas. Reducing the amount of CO<sub>2</sub> becomes crucial because it not only can produce a better caloric content of natural gas, but also reduces the risk of corrosion caused to the equipment and pipelines (Kidnay et al. 2019; Speight 2019). Therefore, there is an urgent need to develop the technology for CO<sub>2</sub> capture and removal from natural gas.

Adsorption is deemed a promising technology for CO<sub>2</sub> capture as it can be retrofitted to any power and natural gas processing plant operated at various conditions with relatively high capacity, high CO<sub>2</sub> selectivity, and low energy requirement for regeneration. Furthermore, it can be applied to pre- and post-combustion pathways (Bui et al. 2018). In addition, waste materials can be utilized to prepare adsorbents, and the adsorption process could be more sustainable.

Most efforts in developing advanced adsorbents have been focused on improving CO<sub>2</sub> adsorption capacity, CO<sub>2</sub> selectivity, and impurity tolerance. Many solid adsorbents have been investigated, including carbons and carbon nanotubes (Mukherjee et al. 2019; Siegelman et al. 2021; Yang et al. 2020), zeolites (Morales-Ospino et al. 2020; Cheng et al. 2020), molecular sieve (Morali et al. 2019; Hou et al. 2021), silica (Santiago et al. 2020; Sánchez-Zambrano et al. 2020) and metal-organic frameworks (Mohamedali et al. 2019; Madden et al. 2021). During recent years, carbonaceous materials such as activated carbons (ACs), carbon molecular sieves, carbon nanotubes and graphene have been intensively investigated for CO<sub>2</sub> capture and removal. They are found effective in CO<sub>2</sub> capture and removal because of their inherent properties such as high specific surface area, excellent thermal and chemical stability, mild adsorption condition, low manufacturing cost, ease of regeneration, low energy consumption and environmentally benign nature (Mukherjee et al. 2019; Siegelman et al. 2021).

This thesis focuses on fundamental mechanisms of CO<sub>2</sub> adsorption and

separation from natural gas. The ACs are the products from the thermal decomposition of wood, coal, lignite or coconut shell with activation of a chemical or physical oxidizing agent. Different temperature and activation processes for the ACs result in different surface chemistry and different pore size distribution including micropore ( $\leq 2$  nm), mesopore (2-50 nm) and macropore ( $\geq 50$  nm) (Marsh and Reinoso 2006). However, experimental study could hardly interpret the relationship between the carbon structure and gas separation performance from a microscopic perspective. Also, the AC has rather complex physical structure and chemical properties, including wide pore size distributions, unevenly distributed solid densities, surface heterogeneity and the topological nature of the connected pore structures (Brennan et al. 2001). It is indeed difficult to understand the underlying mechanisms and the effect of these properties through experimental works.

Various computational techniques such as lattice gas theory (Masel 1996), density functional theory (Sholl and Steckel 2011) and molecular simulation (Frenkel and Smit 2002) can better understand the underlying mechanisms of adsorption and have been well recognized as useful tools and compensation of experimental studies. Molecular simulation is a popular and powerful tool for studying adsorption behaviors and mechanisms. The two equivalent principle approaches to molecular simulations are molecular dynamics (MD) simulation (Nicholson et al. 1982) and Monte Carlo (MC) simulation (Frenkel and Smit 2002). The MD simulation has the capability to research for kinetic evolution of the system and solve motion equations of particles as well as compute the fluid properties. However, the MD application is limited because of the relatively short time scale to be handled using current computation power. On the other hand, the MC simulation is designed for the equilibrium study of an adsorption system. It uses sampling and configurations corresponding to Boltzmann weight to calculate thermodynamic properties as an ensemble average (Nicholson et al. 1982). Thus, the MC simulation has become the preferred theoretical method for studying equilibrium properties of the adsorption system. This thesis focuses on the equilibrium study by examining the mechanisms of  $\text{CO}_2$  adsorption in the AC that associated with its separation and removal from natural gas mixtures, with the ultimate goal to facilitate the development of technology of  $\text{CO}_2$  adsorption and removal in natural gas purification. The MC simulation was performed for achieving the aim.

## 1.2 Literature Review

### 1.2.1 Potential models of CO<sub>2</sub>

An adsorption system comprises adsorbent (i.e., carbon solid) and adsorbate (i.e., fluid). The suitable selection of potential models for both adsorbent and adsorbate is vital to ensure the reliability of the computation. The potential model of adsorbate can be determined based on the description of bulk phase equilibria (Birkett and Do 2004; Möller and Fischer 1994; Mick et al. 2015) and data fitting with available experimental results (Fan et al. 2013).

Lennard-Jones (LJ) potential and exp-6 potential are commonly used in the MC simulation. The exp-6 potential consists of an extra and ambiguous parameter, although they can consider extreme conditions, for instance, high pressures (Okumura and Yonezawa 2000; Vortler et al. 1997). The LJ potential is frequently applied in adsorption systems because of its simplicity and excellent computational efficiency (Birkett and Do 2004). Also, it is compatible with Steele 10-4-3 and Bojan-Steele equations for calculating adsorbate-adsorbent interactions energy (Bojan and Steele 1993).

The molecular potential models are mostly empirical and constitute effective parameters from experimental data fitting or macroscopic properties (Birkett and Do 2004). The macroscopic properties include vapour-liquid equilibria (VLE), second virial coefficient, spectroscopic data, gas viscosity data and liquid radial density distribution. Interestingly, the fitting results from the second virial coefficient data outperformed those from gas viscosity data (Do and Do 2005). However, researchers and industry are more interested in the properties such as density and pressure in the adsorption system. Thus, phase equilibria data can be a better criterion for selecting effective potential models. Do and Do (2005) established an adsorption system in which equilibrium occurs between the dense adsorbed and gaseous phases. In this system, the molecular parameters that can well-describe the VLE can be identified for adsorption studies.

Potential models such as transferable potentials for phase equilibria model for CO<sub>2</sub> (Potoff and Siepmann 2001) and other complex adsorbates (Rai and Siepmann 2007) can describe the experimental phase coexistence properties well (Panagiotopoulos 1999). The parameters of the potential models are summarized in Table 1.1. A number of intermolecular potential models for CO<sub>2</sub> have been proposed in the literature such as HMT (Hammonds et al.



1990), Five charge (Murthy et al. 1983), TraPPE (Potoff and Siepmann 2001) and 1C-LJ model (Wu et al. 2015). Do and Do (2006a) compared three multi-sites potential models (i.e. TraPPE, HMT and Five charge) and the simple 1C-LJ model on their adsorption on graphitized carbon black, and found the TraPPE model is superior in describing the experimental isotherms at the specified conditions. In the same work, the effects of quadrupole interaction and molecular shape were also investigated briefly for CO<sub>2</sub> adsorption mainly in micro-slit pores.

**Table 1.1** Potential model parameters for CO<sub>2</sub> (Hammonds et al. 1990; Murthy et al. 1983; Potoff and Siepmann 2001; Wu et al. 2015).

	Atom	$\sigma$ (nm)	$\varepsilon/k_B$ (K)	q ( $e$ )	Geometry (nm)
CO <sub>2</sub>					
1C-LJ		0.3648	246.15	-	-
TraPPE	C	0.28	27	+0.7	0
	O	0.305	79	-0.35	1.16
HMT	C	0.2824	2.62	+0.664	0
	O	0.3027	74.8	-0.332	1.162
Five charge	C	0.2824	2.63	+0.1216	1.5232
	O	0.3026	75.2	-0.6418	1.0663

Remarks:  $\sigma$  is collision diameter,  $\varepsilon/k_B$  is well-depth, q is the charge of the atom.

The 1C-LJ model has the simplest CO<sub>2</sub> representation as it simulates the molecule in a spherical shape with single LJ site and no charge, therefore, the quadrupole moment and elongated shape of CO<sub>2</sub> molecule are not considered. The great advantage of applying 1C-LJ model is its computational efficiency. The TraPPE model (i.e. 3C-LJ+3Q) is triatomic CO<sub>2</sub> model comprising three dispersive interaction sites, located on each atoms, and three discrete charges are assigned at the same locations to consider the high quadrupole moment of CO<sub>2</sub>, and it has an elongated shape as compared to the 1C-LJ model.

The major differences between these two models for their adsorption in confined spaces have been observed are: the 1C CO<sub>2</sub> molecules in monolayer tends to form hexagonal packing, while the 3C CO<sub>2</sub> molecules show richer features, including the tilted configuration (Do and Do 2006a), pinwheel structures (Golebiowska et al. 2009; Kuchta and Eppers 1987; Xu et al. 2021)

and herringbone structures (Hammonds et al. 1990; Terlain and Larher 1983; Xu et al. 2019). The type of conformation is decided by the principle that configuration energy of the system should be minimized (Do et al. 2010; Steele 1996; Xu et al. 2019).

### 1.2.2 Bulk phase equilibria for CO<sub>2</sub>

The selection of CO<sub>2</sub> potential model is crucial to accurately describe the bulk phase equilibria, especially for vapour pressure (Do and Do 2006b). The MC simulation was used to perform the bulk phase equilibria study to evaluate and develop potential model(s) (Birkett and Do 2004; Liu et al. 2020; Mick et al. 2015; Rai and Siepmann 2007). However, the conventional MC method is rather inefficient because of its poor capability in handling the uneven density distribution between the two coexistence phases.

Gibbs ensemble MC (GEMC) method was then proposed to overcome the limitation by swapping molecule(s) between two individual phase boxes (Panagiotopoulos 1987, 1996). This GeMC method can excellently evaluate the potential model of pure adsorbates or mixtures with complex intermolecular potentials (Gao and Wang 1997; Vega et al. 1992). However, due to insufficient sampling of phase regions, the GeMC method fails to handle complex intermolecular interactions that involve solid or structured phases (Panagiotopoulos 1992, 1999). The continuous development in MC methods has significantly improved the efficiency and accuracy of sampling and calculation. The improved MC methods are, for instance, Grand Canonical histogram reweighting Monte Carlo method and Gibbs-Duhem integration method (Kofke 1993; Potoff et al. 1999).

Further to recent, Bin-canonical Monte Carlo (Bin-CMC) method was developed by introducing multi-bins to handle the non-uniformity of adsorption system (Fan et al. 2012). This Bin-CMC method has high sampling efficiency and accurately describes the vapour-solid and vapour-liquid equilibria (Fan et al. 2013; Liu et al. 2020). In addition, the Bin-CMC method well-describes the density profiles between the rarefied and dense phases. It can also calculate more thermodynamic properties compared to the GEMC method (Liu et al. 2020; Nguyen et al. 2013).

### 1.2.3 Adsorption of CO<sub>2</sub> in activated carbon

Adsorption in carbon adsorbents (including AC) and their mechanisms have attracted great research interest, especially for hysteresis phenomenon through experimental works and theoretical analysis (Burgess et al. 1989; de Boer 1973; Dantas et al. 2019; Foster 1951; Heffelfinger et al. 1988; Liu et al. 2019, 2020; Prasetyo et al. 2016; Ravikovitch et al. 1995; Thommes et al. 2015; Velasco et al. 2016; Zeng et al. 2014, 2017). The hysteresis can be explained through International Union of Pure and Applied Chemistry (IUPAC) classification (see Figure 1.1) and de Boer classification (see Figure 1.2). The former is the latest version of the hysteresis classification (Thommes et al. 2015). The hysteresis characterizes porous carbon structures and is dependent on operating conditions and parameters such as pressure, temperature, pore size and structure, etc.. The hysteresis can be observed in micropores and on the homogeneous surface due to the ordering transition of adsorbate and other conditions (Diao et al. 2015, 2016; Prasetyo et al. 2016). However, these observations are often neglected and are interpreted as molecular filling or layering mechanisms. It is also worth noting that capillary condensation only occurs in mesopores at low temperatures below the critical hysteresis temperature (Morishige and Nakamura 2004; Tompsett et al. 2005).

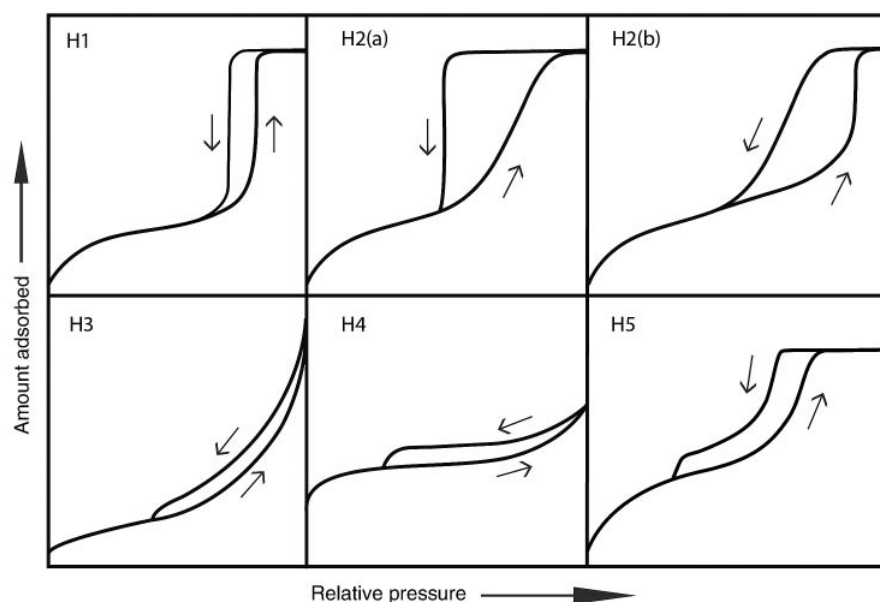


**Figure 1.1.** IUPAC hysteresis loops classification (Thommes et al. 2015).

The molecular simulation considers the ACs in various representative pore

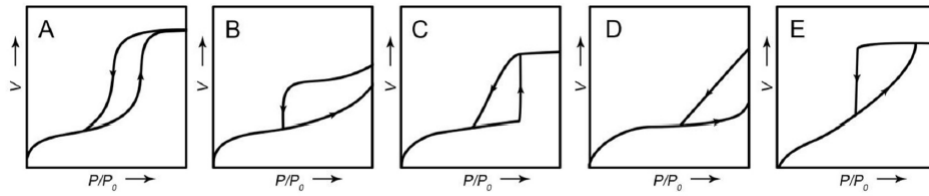


**Figure 1.2.** de Boer classification for hysteresis loops (de Boer 1973).

models that produce experimentally observed hysteresis and reveal underlying mechanisms. Many theoretical studies presumed ACs as a collection of independent, non-interconnecting slit pores with smooth, homogeneous graphitic walls to generate a kernel of isotherms (de Oliveira et al. 2021; Nguyen and Do 1999; Ravikovitch et al. 2000; Kohmuean et al. 2021). The generated isotherm is fitted with the experimental isotherm to obtain the pore size distribution (de Oliveira et al. 2021; Kohmuean et al. 2021). The structure of carbons can be built based on the considerations such as shapes of pores, connections between pores and pore size distribution (Rouquerol et al. 1994), geometrical corrugation (Guo et al. 2012; Jagiello and Olivier 2013) and pores with closed-end (Liu et al. 2020; Pan et al. 2016). In addition, more realistic and amorphous pore models have been developed (de Tomas et al. 2019). However, these pore models are complex and too complicated to be utilized in understanding the underlying mechanism of adsorption. Also, the computation and analysis of these pore models are relatively expensive. Thus, applying simplified yet representative pore model is non-trivial to facilitate the fundamental study and the above considerations.

The structure of AC is represented schematically as shown in Figure 1.3(a) and the uniform slit pore is frequently used as a basis for modeling the AC as displayed in Figure 1.3(c). Apparently, the structure of AC is more complex than is implied by the uniform slit model. As shown in Figure 1.3(b), the AC is composed of cross-linked, graphite-like crystallites based on seminal X-ray studies. Considering the thermal treatment at between 1700 and 3000 °C, the crystallites of the AC are realigned due to the weakening cross-linking in the AC. Consequently, the inter-crystallite spaces start to move toward the slit pores on parallel sides. Due to the phenomena such as the pre-orientation of crystallites and the spatial constraint of the relative positions, the pores are then transformed into a non-uniform cross-sectional width that are varied along the axial direction. In fact, the crystallites are stacked randomly and

the confined spaces between the carbon stacks tend to be wedge shaped as illustrated in Figure 1.3(d). A number of studies (e.g., Liu et al. 2019; Loi et al. 2020a,b) proposed to use wedge shaped pore as a more realistic model for characterization of the AC.

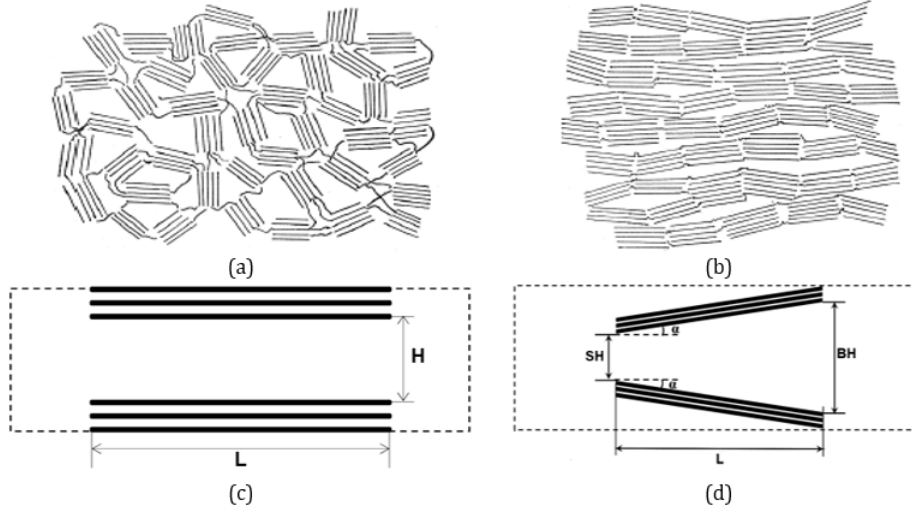


**Figure 1.3.** Schematic representations for an activated carbon (Rosalind 1951) (a) non-graphitizing carbon; (b) graphitizing carbon; (c) slit pore model; (d) wedge pore model.

The typical isotherm for a wedge pore possesses a Type C (in the de Boer classification) hysteresis loop, where its detailed shape depends on specific geometric configurations, including the range of pore widths, pore length and tilt angle. This Type C hysteresis is not commonly observed experimentally because the wedge configuration tends to be masked by other effects, such as closed ends and ink-bottle structures. A stepwise character of desorption branch can be realized on the isotherm of argon in a wedge pore at 70K or 77K (Loi et al. 2020a,b). The hysteresis loop is stepped at the desorption boundary due to a transition between commensurate and incommensurate packing (Loi et al. 2020b). However, this feature was not observed at higher temperatures, e.g., 87K (i.e., experimental boiling point of argon).

Understanding  $\text{CO}_2$  adsorption behaviours in AC is not only important for designing carbon adsorbents for carbon capture, but also of fundamental importance as  $\text{CO}_2$  adsorption is intermediate between noble gases and molecules such as water and ammonia, with strong dipole moment. Besides being the anthropogenic greenhouse gas,  $\text{CO}_2$  is commonly used in characterizing the small pores of carbonaceous materials at 273K as it has faster

diffusion rates than other commonly used probe molecule at cryogenic temperatures (Dantas et al. 2021; Lozano-Castelló et al. 2004). However, most of the studies have been focused on the CO<sub>2</sub> adsorption on AC near critical point or under supercritical conditions experimentally (Bell et al. 2021; Han et al. 2019; Hao et al. 2020) and by modelling (El Oufir et al. 2021; Kouetcha et al. 2018; Wang et al. 2018). Limited attention was paid to CO<sub>2</sub> adsorption at low temperatures below the bulk triple point (Xu et al. 2019) and above the bulk triple point (Dantas et al. 2019).

Pores in real carbon materials do not always have homogeneous surfaces, but possess geometrical corrugations, which are either as a result of impurities or defects acquired during synthesis or arise naturally as a consequence of discrete atomic structure (Guo et al. 2012; Jagiello and Olivier 2013). From IUPAC classification, it is worth noting that Type H2 hysteresis occurs in carbon solids with interconnected pore networks (Thommes et al. 2015). The interconnected pore networks consist of large cavities and small necks connected to the bulk gas. The existence and number of hysteresis loops are dependent on the interconnectivity (i.e., the sizes of both necks and cavities) (Bruschi et al. 2015). The existence of hysteresis is realized as pore-blocking and/or cavitation mechanisms (Ravikovitch and Neimark 2002b). Initially, the menisci of fluid recede from the neck mouth to the pore interior while the fluid in the cavity gradually evaporates. The cavitation mechanism of fluid occurs at the narrow neck. The fluid inside the cavity is then elongated to its mechanical stability limit. Finally, the fluid in the cavity evaporates and the fluid in the neck fluid is partially filled. These pore-blocking and/or cavitation mechanisms are sensitive to temperature, adsorbate species and properties, and relative size between neck and cavity (Morishige et al. 2006; Ravikovitch and Neimark 2002a,b; Rasmussen et al. 2010).

#### 1.2.4 Adsorption of CO<sub>2</sub>-containing mixture in activated carbon

Many studies have been conducted on CO<sub>2</sub> separation, purification from natural gas, carbon capture and storage (Siegelman et al. 2021). The studies comprise interest in the adsorption of CO<sub>2</sub>, methane (CH<sub>4</sub>), nitrogen (N<sub>2</sub>) and their mixtures using AC. The information about preferential adsorption of the adsorbates in gas mixtures is crucial for optimizing carbon capture, separation and purification performance. However, the underlying mech-

anisms for the adsorption of mixtures are difficult to understand through experimental study solely due to complexity of the system.

Several theoretical models (Cochran et al. 1985; Myers and Prausnitz 1965; Ruthven 1984; Suwanayuen and Danner 1980) have been proposed for describing adsorption of mixtures with Ideal Adsorbed Solution Theory (IAST) as the most popular one due to its predictive power and simplicity (Myers and Prausnitz 1965; Simon et al. 2016). However, IAST performs poorly when the interadsorbate interactions become significant (Tan et al. 2021) and when the adsorbent is highly heterogeneous (Swisher et al. 2013; Walton and Sholl 2015). For the non-ideal condition, the parameters introduced by real adsorbed solution theory (RAST) (Swisher et al. 2013) are used to compensate the predictive capability. However, this method can only be applied to specific mixture groups. A little can be known about the underlying mechanisms of adsorption for mixtures, for example, the competitive and synergistic adsorption of mixtures. Molecular simulation such as Monte Carlo (MC) simulation (Frenkel and Smit 2002; Norman and Filinov 1969) is an effective tool to investigate the adsorption behaviors of mixtures from a microscopic perspective and therefore can facilitate the development of adsorbents with customized properties for more effective carbon capture performance.

Experimental mixture adsorption data of  $N_2$ ,  $CH_4$  and  $CO_2$  on the ACs were available such as Norit RB2 (Goetz et al. 2006) and Norit-R1 Extra (Dreisbach et al. 1999). The adsorption experiments using the Norit RB2 were executed volumetrically at temperatures ranging from 273 to 298K. Those using the Norit-RB1 Extra were obtained gravimetrically at 298K. The chemical potentials for mixtures as a function of temperature, pressure and molecular fractions of multicomponent were studied with the isothermal and isobaric (NPT) scheme (Tan et al. 2016), which has been approved to be an efficient method for calculating the chemical potentials for mixtures in both the gaseous and liquid phases. The adsorption of mixtures in the AC, which is modelled as simplified homogeneous pores, is investigated by applying the GCMC method (Do and Do 2003). This approach can mimic the volumetric adsorption method.

Numerous studies explore the adsorption of  $CO_2$  from gas mixtures on the AC using a uniform slit pore model, e.g.  $CO_2/N_2$  and  $CO_2/CH_4$  mixtures (Cracknell et al. 1996),  $CO_2/CH_4$  mixtures (Kurniawan et al. 2006; Billefont et al. 2011, 2013; Heuchel et al. 1999; Palmer et al. 2011; Trinh et al. 2016)

and ternary CO<sub>2</sub>/CH<sub>4</sub>/CO mixtures (Sweatman and Quirke 2005). A single and binary adsorption equilibria of CH<sub>4</sub> and CO<sub>2</sub> has been explored in carbon slit pores with different pore sizes (Kurniawan et al. 2006). Palmer et al. (2011) indicated that the key factors such as the pore morphology and pore size contributed in effective separation based on the adsorption behaviour of CO<sub>2</sub>, CH<sub>4</sub> and mixtures in different types of nanoporous carbons.

The excess adsorption amount in the micropores is increased along the increasing of pore size. However, the mesopores show a reverse trend in the excess adsorption amount (Sizova et al. 2018; Zhang et al. 2018; Zhou et al. 2018). The reason is due to that the superimposed effect of the pore wall reduces the adsorption amount as the mesopore size is increased (Chen et al. 2016; Xiong et al. 2017; Han et al. 2018). As the pore volume is increased, more space is allowed for adsorbate to access and thus, the adsorption amount is reduced (Mosher et al. 2013; Xiong et al. 2017). In fact, a micropore has a larger surface area than a mesopore. A larger surface area of micropore provides more adsorption sites and more adsorbates can be captured because of the stronger wall-wall overlapping effect in micropore. This results in a higher adsorption amount (Mosher et al. 2013; Xiong et al. 2017).

Isosteric heat of adsorption provides important thermodynamic parameter for calculating energy release and exhibiting the strength of interaction (Huang et al. 2018; Yang et al. 2018). Temperature plays an important role in CO<sub>2</sub>/CH<sub>4</sub> adsorption. With the increasing temperature, the isosteric heat of CO<sub>2</sub>/CH<sub>4</sub> is decreased because more kinetic energy allows the gas molecules to escape from the surface of adsorbent (Han et al. 2018; Sha et al. 2018). This thus leads to a weaker interaction between gas molecules and the adsorbent (Yu et al. 2017).

Isosteric heat can be enhanced with the increase in pressure (Han et al. 2018). Huang et al. (2018) observed the interactions and collisions between gas molecules were intense at higher pressure. This leads to an increase in the isosteric heat. The solid-fluid interaction is indeed primary contributing factor at low pressure and reduces the adsorption amount due to the gas molecules adsorbed at higher energy sites of the adsorbent. The fluid-fluid interaction increases the gas loading at high pressure (Han et al. 2018). On the other hand, some studies (Huang et al. 2018; Xiang et al. 2014) indicate that pressure has negligible effect to the isosteric heat of CO<sub>2</sub>/CH<sub>4</sub> adsorption.

With the increasing pore size, the isosteric heat is gradually decreased and



then becomes plateau as the overlapping effect is reduced and the adjacent surface has less impact on CO<sub>2</sub>/CH<sub>4</sub> adsorption (Han et al. 2018; Xiong et al. 2017; Zhang et al. 2018). Moreover, unstable adsorbed gas can also weaken the released heat when the pore size is increasing (Han et al. 2018).

Gas mixtures can be separated by selective adsorption of one species in the AC. The effectiveness of the separation can be quantified in terms of the selectivity (Dong et al. 2019; Huang et al. 2018; Sizova et al. 2018). The adsorption selectivity can be influenced by many factors. With the increasing pressure, Zhou et al. (2019) found that the selectivity of CO<sub>2</sub>/CH<sub>4</sub> is decreased until a plateau. CO<sub>2</sub> has high affinity toward the AC and occupies high energy sites at low pressure. CO<sub>2</sub> is then filled the low energy sites upon the high energy sites are filled (Zhang et al. 2015). When the CO<sub>2</sub> turns saturated, CH<sub>4</sub> is continued to capture the remaining sites with low energy. CH<sub>4</sub> is more likely to access micropores at high pressure. This thus leads to a decreasing selectivity of CO<sub>2</sub>/CH<sub>4</sub> until the adsorption reaches equilibrium.

A smaller pore size allows more overlapping spaces that have stronger interactions between adsorbate-adsorbate and adsorbate-adsorbate (Huang et al. 2007; Kurniawan et al. 2005; Kowalczyk et al. 2012). This results in a higher selectivity. A smaller diameter pore shows higher selectivity as compared to a larger pore. The aerodynamic diameter of CO<sub>2</sub> is shorter than that of CH<sub>4</sub> and CO<sub>2</sub> has higher interaction potential and a greater adsorption loading as compared to CH<sub>4</sub> (Huang et al. 2007). These ease CO<sub>2</sub> to access smaller pores as well as enhances the selectivity. A wedge pore model can mimic the presence of dead end in ACs, which does impact the adsorption at low pressure region, and this cannot be captured with the uniform slit pore model. Therefore, the wedge pore model can be treated as an alternative model for representing the non-uniform pore size distribution in the AC.

### 1.3 Thesis Objectives

The main objectives are specified as follows:

1. To study the adsorption behaviours of pure CO<sub>2</sub> in the AC simulated with idealized and/or more realistic pore model, to elaborate the effects of pore configuration (pore size, shape, etc.) on the adsorption

behaviours at subcritical conditions.

2. To evaluate the effects of CO<sub>2</sub> potential models on their performances within different scenarios, including the vapor liquid/solid equilibrium (VLE/VSE) of bulk phase, and adsorption in the AC.
3. To understand the effects of presence of other gases on the adsorption behaviours of CO<sub>2</sub> adsorption, for instance, N<sub>2</sub>, CH<sub>4</sub>, etc..
4. To propose the optimized parameters of adsorbent and operating conditions based on the successful outcomes from the first three objectives in order to maximize the CO<sub>2</sub> adsorption capacity and separation efficiency from natural gas.

## 1.4 Thesis Organization

The organization of this thesis is outlined as follows. Chapter 2 details the theories and Monte Carlo simulation applied in this thesis. It addresses Monte Carlo ensembles, potential models used, adsorptive simulation system, and equations for calculating the thermodynamic properties, IAST and selectivity. Chapters 3 and 4 focus on pure CO<sub>2</sub> adsorption in wedge-shaped pores, which is a more realistic model for activated carbon, and was used as the alternative to the commonly used slit pore model in Chapter 5, where the mixture adsorption in wedge pores was investigated. The single-component adsorption behaviours serve as the foundation of understanding mixture adsorption. Therefore, the characters and mechanisms of CO<sub>2</sub> adsorption in wedge pores learned from the Chapters 3 and 4 facilitate the understanding of mixture adsorption in Chapter 5, and based on the experimental data, the carbon solids were characterized with a wedge pore model.

With the above information, Chapter 5 then provides a fundamental understanding of the adsorption of CO<sub>2</sub> from natural gas mixtures containing CH<sub>4</sub> and N<sub>2</sub> at the molecular level for activated carbon. In this study, the TraPPE CO<sub>2</sub> was selected considering its accuracy in describing experimental data for both bulk phase and adsorption studies as presented in Chapter 4. This thesis is concluded in Chapter 6 with remarks and recommendations for future works.

# Chapter 2

## Theory and Simulation

This chapter summarizes the main theories and Monte Carlo (MC) simulation methods applied in this thesis. The methods of Bin-Canonical MC, NPT and Grand Canonical MC are described. Also, the characterizations of pore models and simulation systems used are presented.

### 2.1 Monte Carlo Simulation

The classical theories such as Langmuir approach only can provide a simple description for the adsorption behaviours of molecules on a homogeneous carbon surface. Also, the theories involve empirical fitting parameters and assumptions that are not compatible for real practice and experiment. Due to these limitations of classical theories, MC simulation then becomes a better alternative method to investigate the equilibrium of adsorption systems by generating a Markov chain in a sequence of configurations following with generating ensemble averages from calculations of thermodynamic properties of adsorption system. The MC simulations use a number of ensembles (Frenkel and Smit 2002), i.e. canonical (constant  $NVT$ ), grand canonical (constant  $\mu VT$ ), isobaric-isothermal (constant  $NPT$ ) and isotension - isothermal (constant  $NST$ ) ensembles. We applied Bin-Canonical MC (Fan et al. 2012), NPT (Tan et al. 2016) and grand canonical MC (Frenkel and Smit 2002) in this thesis.

### 2.1.1 Grand canonical Monte Carlo

The Grand Canonical Monte Carlo (GCMC) was initially proposed by Norman and Filinov (1969) and was then commonly applied in adsorption research. In MC simulation, the GCMC describes an isolated system with constant chemical potential, temperature and volume. The system is then built in an infinite bulk reservoir with variation in number of adsorbate molecules and constant temperature and chemical potential. This system condition is precisely aligned to adsorption experiment. This ensemble is also capable of measuring adsorption isotherms of single and multiple components and revealing adsorbate-adsorbate and adsorbate-adsorbents interactions. The conventional MC simulation in the GCMC ensemble are described as follows.

Step 1: Initialize a system (i.e. a rectangular simulation box) with number of particles ( $N$ ), specified chemical potential ( $\mu$ ), temperature ( $T$ ) and volume ( $V$ ).

Step 2: Compute the energy of the initial system configuration ( $U$ ), which is the potential energy before displacement, insertion or deletion.

Step 3: Select a random particle. The random movement of the selected particle from an initial point ( $x,y,z$ ) to a new point ( $x',y',z'$ ) is known as displacement.

Step 4: Compute the energy of the new system configuration ( $U'$ ), which is the potential energy after displacement, insertion or deletion.

Step 5: Evaluate the new system configuration ( $U'$ ) based on the insertion probability

$$P^{acc} = \min \left[ 1, \frac{V}{\Lambda^3(N+1)} \exp\{\beta(\mu - U' + U)\} \right] \quad (2.1)$$

and/or based on the deletion probability

$$P^{acc} = \min \left[ 1, \frac{\Lambda^3 N}{V} \exp\{-\beta(\mu + U' - U)\} \right] \quad (2.2)$$

where  $\Lambda$  is thermal de Broglie wavelength,  $\beta$  is reciprocal temperature,  $1/k_B T$  with Boltzmann's constant  $k_B = 1.38066 \times 10^{-23} \text{ J/K}$ .

Step 6: If the new configuration is accepted, the initial configuration will be updated with the latest position of the particles and energy of new configuration system. Otherwise, the initial configuration will be re-computed.

Step 7: In the event of  $D$  number of steps, the properties of the system will be calculated in total as follows:

$$X_{prop} = \sum_{i=1}^D X_i \quad (2.3)$$

where  $X_i$  is the property at  $i^{th}$  configuration.

Step 8: Step 2 to Step 7 will be repeated until reaching an adequate number of configurations where the system reaches equilibrium.

Step 9: When the system reaches equilibrium, an average of the ensemble for a thermodynamic property is calculated as follows:

$$\langle X_{avg} \rangle = \frac{\sum_{i=1}^D X_i}{D} \quad (2.4)$$

In this thesis, we employed GCMC simulation (Do and Do 2003; Frenkel et al. 1997) at a number of cycles  $N_c$  in both equilibration and sampling stages to obtain the adsorption isotherm and structural properties. Each cycle consists of 1000 displacement moves, insertion and deletion with equal probability. As a result, this generated a total of  $N_c \times 10^3$  configurations. In the equilibration stage, the maximum displacement length is initially configured as half of the largest box dimension and adjusted at the end of each cycle to reach an acceptance ratio of 20% (Mountain and Thirumalai 1994). The dimension of the simulation box in the  $x$ -direction is set as 10 times the collision diameter of  $\text{CO}_2$ . The dimension in the  $z$ -direction follows the pore width of the larger end. The cut-off radius is 5 times the collision diameter of the carbon atom of  $\text{CO}_2$ .

### 2.1.2 Bin-canonical Monte Carlo

Fan et al. (2012) proposed a Bin-Canonical Monte Carlo (Bin-CMC) scheme, which is capable of dealing with the non-uniformity of the adsorption system. This scheme introduces individual bins that comprise patches of similar

interaction energies to the conventional canonical MC. As a result, the maximum displacement length is relatively long in the rarefied region and small in the dense region. This can improve the efficiency of sampling in both the rarefied and dense regions.

The Bin-CMC starts the adsorption system with fixed temperature ( $T$ ), total number of molecules ( $N$ ) and total volume of the system ( $V$ ). Each bin is taken as a pseudo grand canonical ensemble with constant volume, temperature and chemical potential ( $\mu$ ). The subsequent process transfers a molecule from bin  $C$  to bin  $D$  and then displaces molecules within the two bins following with reverse transfers of a molecule from bin  $D$  to bin  $C$ . These reverse transfers aim to achieve microscopic reversibility.

A molecule follows two steps transferring from bin  $C$  to bin  $D$ . These steps are equivalent to the grand ensemble processes: deletion and insertion. First, a random molecule is deleted from bin  $C$  to the surroundings at a fixed chemical potential. Then, a molecule is inserted from the surroundings to a random position in bin  $D$ . The acceptance probability is stated as follows.

$$P_{Trs}^{acc} = \min \left[ 1, \frac{N_c/V_c}{(N_D + 1)/V_D} \exp\{-\beta Q - W\} \right] \quad (2.5)$$

where  $Q = U(N_D + 1) - UN_D$ ,  $W = U(N_C - 1) - U(N_c - 1)$ , and  $Q$  and  $W$  are the energy changes for deletion and insertion, respectively.

In this thesis, the Bin-CMC method is used to perform the phase equilibria study for temperatures ranging from below the triple point to the critical point of  $\text{CO}_2$ . For the vapor-solid equilibria (VSE) below the triple point, the system is initialized by placing a solid slab of  $\text{CO}_2$  molecules arranged in the *fcc* structure at the middle of an elongated simulation box with vacuum spaces on both sides of the slab. The simulation box is divided into 28 bins for the purpose of determining the density distribution and the bin size is smaller in the interfacial and condensed phase regions and larger in the gas phase region. To ensure the accuracy of output data, at least  $N_m \times 10^5$  cycles were employed, with 1000 displacement moves in each cycle and, in both the equilibration and sampling stages. Details of the Bin-CMC scheme and the calculation methods of various thermodynamic properties can be found elsewhere (Fan et al. 2012). For temperatures above the triple point, the same simulation procedure described above was performed to determine the vapor-liquid equilibria (VLE). The only difference is that the solid slab is replaced with a lattice having an initial density equal to the bulk liquid density at the boiling point.

### 2.1.3 Isobaric-isothermal (NPT)

The NPT ensembles were initially proposed by Wood (1968) and subsequently applied by McDonald (1972) in systems with continuous intermolecular forces. The NPT simulation method is used to determine chemical potentials for mixtures as a function of temperature, pressure and mole fractions of all components including CO<sub>2</sub>, CH<sub>4</sub> and N<sub>2</sub> (Tan et al. 2016, 2020). The NPT ensemble can calculate chemical potentials accurately even in circumstances where most conventional methods fail. The chemical potentials can be calculated using the equations detailed in Sect. 2.2.2. The pressure calculated via the virial route should equal the specified pressure (or close to it within statistical error). To ensure the accuracy of output data, at least 10<sup>4</sup> cycles were employed, 10<sup>4</sup> displacement moves and 10 volume change moves in each cycle and, in both the equilibration and sampling stages. After displacement moves, the partial average pressure was used to decide on the volume change. The initial volume and number of particles were set at specified volume in nm<sup>3</sup> (cubic box) and 300, respectively. All three dimensions are altered when the volume is changed.

## 2.2 Thermodynamic Property Calculations

### 2.2.1 Potential energy

#### Fluid-fluid potential

The Lennard-Jones (LJ) model is commonly used to elucidate the interaction between two dispersive sites. The reason is due to its simplicity and readily available parameters for a range of fluids. This model is also compatible with the potential equations used to calculate the solid-fluid interactions such as Bojan-Steele equations (Bojan and Steele 1988, 1993). The 12-6 LJ potential equation

$$\varphi_{ff}(r) = 4\varepsilon_{ff} \left[ \left( \frac{\sigma_{ff}}{r} \right)^{12} - \left( \frac{\sigma_{ff}}{r} \right)^6 \right] \quad (2.6)$$

is used to calculate the interaction between two fluid molecules, where  $r$  is the separating distance between two molecules,  $\varepsilon_{ff}$  is the well-depth of interaction energy and  $\sigma_{ff}$  is the collision diameter at which  $\varepsilon_{ff} = 0$ .

Given that a molecule with multiple dispersive sites and fixed partial charges, the interaction energy between two molecules is calculated based on

the total of the LJ and Coulomb interactions

$$\varphi_{i,j} = \sum_{a=1}^A \sum_{b=1}^B \frac{q_i^a q_j^b}{4\pi\epsilon_0 r_{ij}^{ab}} + \sum_{c=1}^C \sum_{d=1}^D 4\epsilon_{ij}^{cd} \left[ \left( \frac{\sigma_{ij}^{cd}}{r_{ij}^{cd}} \right)^{12} - \left( \frac{\sigma_{ij}^{cd}}{r_{ij}^{cd}} \right)^6 \right] \quad (2.7)$$

where  $\varphi_{i,j}$  is the interaction energy between the molecules  $i$  and  $j$ ,  $A$  and  $B$  are the number of partial charges on the molecules  $i$  and  $j$ , respectively,  $C$  and  $D$  are the number of LJ sites on the molecules  $i$  and  $j$ , respectively,  $\epsilon_0$  is the permittivity of a vacuum,  $r_{ij}^{ab}$  is the separating distance between charge  $a$  on a molecule  $i$  and charge  $b$  on molecule  $j$  possessing charges  $q_i^a$  and  $q_j^b$ , respectively,  $r_{ij}^{cd}$  is the separating distance between the LJ site  $c$  on molecule  $i$  and the LJ site  $d$  on molecule  $j$ ,  $\sigma_{ij}^{cd}$  and  $\epsilon_{ij}^{cd}$  are calculated using the Lorentz-Berthelot mixing rules:

$$\sigma_{ij}^{cd} = \frac{\sigma_i^c + \sigma_j^d}{2}; \quad \epsilon_{ij}^{cd} = \sqrt{\epsilon_i^c \epsilon_j^d} \quad (2.8)$$

where  $\sigma_{ij}^{cd}$  and  $\epsilon_{ij}^{cd}$  are the combined LJ collision diameter and the well-depth for the two LJ sites, respectively.

### Potential model: CO<sub>2</sub>

Various intermolecular potential models for CO<sub>2</sub> have been proposed such as HMT (Hammonds et al. 1990), Five charge (Murthy et al. 1983), TraPPE (Potoff and Siepmann 2001) and 1C-Lennard-Jones (LJ) model (e.g. Yoshioka et al. 2004). The TraPPE model considers high quadrupole moment of CO<sub>2</sub> by having three discrete charges, while the 1C-LJ model is the most computation efficient. Do and Do (2006a) compared these four intermolecular potential models on the adsorption of CO<sub>2</sub> on graphitized carbon black and slit pores, and found that the TraPPE model is capable to elucidate the adsorption isotherms for CO<sub>2</sub> among the four. The potential model parameters for CO<sub>2</sub> are listed in Table 1.1.

### Potential model: CH<sub>5</sub>

The Amber all-atom model for CH<sub>4</sub> suggested by Sun et al. (1992) considers the tetrahedral shape of CH<sub>4</sub> as well as the octopole moment involved. However, in the TraPPE model, the reduced well depth of carbon atom is 0.01 K, which is not realistic to represent for CH<sub>4</sub>. The potential model parameter for CH<sub>4</sub> is listed in Table 2.1.

### Potential model: N<sub>2</sub>



The united-atomic spherical LJ model of N<sub>2</sub> has been proposed in Ravikovitch et al. (2001) and the authors considered the quadrupole interaction in the effective parameters. The potential model parameter for N<sub>2</sub> is listed in Table 2.1.

**Table 2.1** Potential model parameters for CH<sub>4</sub> and N<sub>2</sub> (Ravikovitch et al. 2001; Sun et al. 1992).

	$\sigma$ (nm)	$\varepsilon/k_B(\text{K})$
CH <sub>4</sub> model		
1C-LJ	0.373	148
N <sub>2</sub> model		
1C-LJ	0.3615	101.5

### Solid-fluid potential

The surface of carbon adsorbents can be modelled based on a structured solid model or an unstructured solid model. The structured solid model contains discrete carbon atoms in hexagonal units, which have carbon-carbon bonds with a length of 0.142 nm. In the unstructured solid model, the solid contains carbon atoms at constant density in each graphene layer. The two solid models are indeed able to provide an equivalence simulation outcome as the barrier between the hexagonal sites is less than  $k_B T$ .

### Structured model

The solid-fluid interaction energy can be calculated based on the total pairwise interactions between each molecule site  $i$  and each carbon atom on the surface. The LJ 12-6 potential equation (2.6) can be rewritten as

$$\varphi_{i,s}(r) = 4\varepsilon_{i,s} \left[ \left( \frac{\sigma_{i,s}}{r} \right)^{12} - \left( \frac{\sigma_{i,s}}{r} \right)^6 \right] \quad (2.9)$$

The total solid-fluid interaction can then be written as

$$\varphi_{i,s} = \sum_{a=1}^M \varphi_{i,a} \quad (2.10)$$

where  $s$  stands for the graphite surface and  $M$  represents the number of carbon atoms on the graphite surface.

### Infinite unstructured model

The Steele 10-4-3 potential

$$\varphi_{i,s} = 2\pi\rho_s\varepsilon_{sf}\sigma_{sf}^2 \left\{ \frac{2}{5} \left( \frac{\sigma_{sf}}{z_i} \right)^{10} - \left( \frac{\sigma_{sf}}{z_i} \right)^4 - \frac{\sigma_{sf}^4}{3\Delta(0.61\Delta + z_i)^3} \right\} \quad (2.11)$$

can be used to calculate the solid-fluid interaction energy between particle  $i$  and a flat, homogeneous solid surface at the infinite extent (Steele 1973a,b). The details are: the surface density of carbon atom in a graphene layer  $\rho_s = 38.2 \text{ nm}^{-2}$ , the spacing between two adjacent graphene layers,  $\Delta = 0.3354 \text{ nm}$  and the shortest distance between the particle and the surface,  $z_i$ . The solid-fluid molecular parameters, which are cross collision diameter,  $\sigma_{sf}$  and well-depth,  $\varepsilon_{sf}$ , can be determined using the Lorentz-Berthelot mixing rule (2.8) by substituting  $\sigma_{ss} = 0.34 \text{ nm}$  and  $\varepsilon_{ss}/k = 28 \text{ K}$ .

### Finite unstructured model

The Bojan-Steele potential

$$\varphi_{f,s} = 2\pi\rho_s\varepsilon_{sf}\sigma_{sf}^2 \{ [\varphi_{rep}(z, y^+) - \varphi_{rep}(z, y^-)] - [\varphi_{att}(z, y^+) - \varphi_{att}(z, y^-)] \} \quad (2.12)$$

$$\begin{aligned} \varphi_{rep}(z, y) = \frac{y}{\sqrt{y^2 + z^2}} & \left[ \frac{1}{5} \left( \frac{\sigma_{sf}}{z} \right)^{10} + \frac{1}{10} \frac{\sigma_{sf}^{10}}{z^8(y^2 + z^2)} + \right. \\ & \left. \frac{3}{40} \frac{\sigma_{sf}^{10}}{z^6(y^2 + z^2)^2} + \frac{1}{16} \frac{\sigma_{sf}^{10}}{z^4(y^2 + z^2)^3} + \frac{7}{128} \frac{\sigma_{sf}^{10}}{z^2(y^2 + z^2)^4} \right] \end{aligned} \quad (2.13)$$

$$\varphi_{att}(z, y) = \frac{y}{\sqrt{y^2 + z^2}} \left[ \frac{1}{2} \left( \frac{\sigma_{sf}}{z} \right)^4 + \frac{1}{4} \frac{\sigma_{sf}^4}{z^2(y^2 + z^2)} \right] \quad (2.14)$$

can describe the interaction between a particle and a homogeneous surface in an infinite  $x$ -direction and in a finite  $y$ -direction, where  $\varphi_{rep}$  and  $\varphi_{att}$  are the repulsive and attractive interaction energy, respectively,  $z$  is the shortest distance between the particle and surface,  $\rho_s$  is the surface density,  $\sigma_{sf}$  and  $\varepsilon_{sf}$  are the solid-fluid molecular parameters. The solid-fluid molecular parameters, which are cross collision diameter,  $\sigma_{sf}$  and well-depth,  $\varepsilon_{sf}$ , can be determined using the Lorentz-Berthelot mixing rule (2.8) by substituting  $\sigma_{ss}$  and  $\varepsilon_{ss}/k$ .

### 2.2.2 Chemical potential

In NPT system, the chemical potential is simulated by the Widom method (Widom 1982), which is based on statistical mechanics. This method can measure excess chemical potential,  $\mu_{ex}$  using a perturbation in the number of particles. A test particle is initiated at a random position in frequent intervals. The energy between the test particle and other particles in the system is computed as  $N_{test}$  particles. The ensemble average used is as follows:

$$\left\langle \exp \left( -\frac{U_{test}}{k_B T} \right) \right\rangle = \frac{1}{N_{cycle} N_{test}} \sum_{n=1}^{N_{cycle}} \sum_{j=1}^{N_{test}} \exp \left( -\frac{U_{nj}^{test}}{k_B T} \right) \quad (2.15)$$

where  $N_{cycle}$  is the number of cycles,  $N_{test}$  is the number of test particles in the Widom method,  $U_{test}$  is the average energy of a test particle with all particles in one cycle,  $U_{nj}^{test}$  is the energy between the test particle  $j$  with the all particles in cycle  $n$ ,  $k_B$  is Boltzmann's constant, and  $T$  is temperature. The excess chemical potential is then calculated as follows:

$$\mu_{ex} = -k_B T \ln \left\langle \exp \left( -\frac{U_{test}}{k_B T} \right) \right\rangle \quad (2.16)$$

The total chemical potential,  $\mu$  is calculated based on the sum of both ideal gas chemical potential,  $\mu_{id}$  and excess chemical potential,  $\mu_{ex}$  as follows:

$$\mu = \mu_{id} + \mu_{ex} \quad (2.17)$$

$$\mu_{id} = \mu_0(T) + k_B T \ln \left( \frac{N}{V} \right) \quad (2.18)$$

where  $\mu_0(T)$  is a standard chemical potential.

### 2.2.3 Pressure

The vapour pressure is computed through a virial route (Allen and Tildesley 1989, p.385) in the Bin-CMC method as follows:

$$p_G = \rho_G k_B T - \frac{1}{3V_G} \left\langle \sum_{i \in V_G} \sum_{j \in V_G, j=i+1}^{N_G} \omega_{ij} \right\rangle - \frac{1}{6V_G} \left\langle \sum_{i \in V_G} \sum_{j \notin V_G} \omega_{ij} \right\rangle \quad (2.19)$$

where  $\omega_{ij}$  is the intermolecular pair virial function:

$$\omega_{ij} = \sum_{a=1}^A \sum_{b=1}^B \frac{\vec{r}_{ij}^a \cdot \vec{r}_{ij}^{ab}}{r_{ij}^{ab}} \frac{\partial u_{ij}^{ab}}{\partial r_{ij}^{ab}} \quad (2.20)$$

which involves the sum of interaction between molecules in the  $V_G$  region corresponding to the second term in (2.19) and involves in the sum of interactions between  $N_G$  molecules and other molecules in the surroundings corresponding to the third term in (2.19).

In the NPT ensemble, the pressure is computed through a virial route (Allen and Tildesley 1989, p.385) as follows:

$$p = \frac{Nk_B T}{V} - \frac{W}{3V} + p_{LRC} \quad (2.21)$$

where  $p_{LRC}$  is the long-range correction and  $W$  is the virial of  $N$  molecules system. The  $W$  is calculated as a total of the pairwise virials  $v_{ij}$  between molecules  $i$  and  $j$ :

$$W = \sum_{i=1}^{N-1} \sum_{j>1}^N v_{ij} \quad (2.22)$$

where the molecular pairwise virial includes the site virials as

$$v_{ij} = \sum_{n=1}^{S_i} \sum_{m=1}^{S_j} \frac{\vec{r}_{i,j} \cdot \vec{r}_{i,j}^{nm}}{r_{i,j}^{nm}} \frac{\partial \varphi_{ij}^{nm}}{\partial r_{i,j}^{nm}} \quad (2.23)$$

where  $\varphi_{ij}^{nm}$  is the potential energy between the site  $n$  on the molecule  $i$  and the site  $m$  on the molecule  $j$ , and  $r_{ij}^{nm}$  is the distance between  $n$  site and  $m$  site. The parameters,  $\vec{r}_{ij}$  is the vector of  $r_{ij}$ ,  $\vec{r}_{i,j}^{nm}$  is the vector between site  $n$  on molecule  $i$  and site  $m$  on molecule  $j$ , and  $S_i$  and  $S_j$  are the number of sites on molecules  $i$  and  $j$ , respectively.

### 2.2.4 Evaporation (sublimation) heat

As reported in Fan et al. (2012), the change of molar enthalpy between the two coexistence phases,  $\Delta h$  is calculated as follows:

$$\Delta h = h_G - h_L = (u_G + pv_G) - (u_L + pv_L) = (u_G + u_L) + p \left( \frac{1}{\rho_G} - \frac{1}{\rho_L} \right) \quad (2.24)$$

where  $h_G$  and  $h_L$  are molar enthalpies of the gas and liquid phase,  $u_G$  and  $u_L$  are molar energies of the gas and liquid phase,  $v_G$  and  $v_L$  are molar volumes of the gas and liquid phase,  $\rho_G$  is the density in gas region,  $\rho_L$  is the average densities of the liquid phase, and  $p$  is the pressure. The molar energies of gas and liquid phases are calculated by summing their pair interaction energies as below:

$$U_G = \sum_{i \in V_G}^{N_G-1} \sum_{j \in V_G, j>i}^{N_G} u_{ij} + \frac{1}{2} \sum_{i \in V_G}^{N_G} \sum_{j \notin V_G} u_{ij} \quad (2.25)$$

$$U_L = \sum_{i \in V_L}^{N_L-1} \sum_{j \in V_L, j > i}^{N_L} u_{ij} + \frac{1}{2} \sum_{i \in V_L}^{N_L} \sum_{j \notin V_L} u_{ij} \quad (2.26)$$

$$u_G = \frac{U_G}{N_G} \quad (2.27)$$

$$u_L = \frac{U_L}{N_L} \quad (2.28)$$

where  $U_G$  and  $U_L$  are the summations over the pair energies in the gas and liquid phase regions,  $V_G$  is volume of gas region,  $V_L$  is volume of bin  $L$ ,  $N_G$  is the number of molecules in gas region, and  $N_L$  is the number of particles in bin  $L$ .

### 2.2.5 Surface tension

Surface tension,  $\gamma$  can be calculated using the Kirkwood and Buff equation (Kirkwood and Buff 1949; Linse 1987) as follows:

$$\gamma = \frac{1}{2S} \left\langle \sum_{i=1}^{N-1} \sum_{j>1}^N \frac{r_{ij}^2 - 3y_{ij}^2}{2r_{ij}^2} \sum_{a=1}^A \sum_{b=1}^B \frac{\vec{r}_{ij} \cdot \vec{r}_{ij}^{ab}}{r_{ij}^{ab}} \frac{\partial u_{ij}^{ab}}{\partial r_{ij}^{ab}} \right\rangle \quad (2.29)$$

where  $N$  is the number of particles,  $r_{ij}$  is the separation of the mass centres of molecules  $i$  and  $j$ ,  $y_{ij}$  is the distance between the mass centres of molecules  $i$  and  $j$  in the  $y$  direction,  $\vec{r}_{ij}$  is the vector of  $r_{ij}$ ,  $\vec{r}_{ij}^{ab}$  is the vector between site  $a$  on molecule  $i$  and site  $b$  on molecule  $j$ ,  $u_{ij}^{ab}$  is the molar energies between site  $a$  on molecule  $i$  and site  $b$  on molecule  $j$ ,  $S$  is the interfacial area.

### 2.2.6 Adsorption isotherm

The adsorption isotherm

$$N_{ex} = N - N_b = N - \rho_b V_{app} \quad (2.30)$$

can be expressed in terms of excess amount between absolute amount in adsorption cell and the total amount occupying at bulk phase, where  $N$  and  $N_{ex}$  are the absolute and excess amount of adsorbate in the adsorption cell, respectively, and  $N_b$  is the number of particle occupying the apparent void volume,  $V_{app}$  within the bulk density,  $\rho_p$ .

In experimental settings, the apparent void volume is obtained by using helium as a medium. The experimental measurement is made on the known dosing amount of helium into the system at a specified temperature,  $T_{He}$  at

which the minimum concentration of helium located (Malbrunot et al. 1997). The helium void volume

$$V_{He} = \int_{V_s} \exp[-\varphi_{He}(\mathbf{r})/k_b T_{He}] d\mathbf{r} \quad (2.31)$$

is expressed in the form of resulting zero excess amount,  $N_{ex}^{He} \approx 0$ , where  $\varphi_{He}(\mathbf{r})$  is the helium-solid potential energy at any position of  $\mathbf{r}$  in the system and  $V_s$  is the volume of the entire system.

Upon a part of helium adsorb at  $T_{He}$ , the helium void volume is then greater than the initial void volume of the system as a function of temperature. However, there are some limitations to this measurement described in Malbrunot et al. (1992) and are then rectified by a high temperature expansion as stated in Malbrunot et al. (1997).

Do and Do (2007) proposed an alternative measurement of apparent volume corresponding to the principle of accessible volume via simulation. The accessible volume is defined as the volume accessible to the centre of mass of a molecule at zero loading (Do et al. 2010). The calculation steps via the MC simulation are described as follows:

Step 1: The centre of mass of a molecule is inserted at a random position in a simulation box and the molecule is then oriented in given  $G$  different orientations, particularly for a multi-site molecule.

Step 2: Once the potential energies of the  $G$  orientations are positive, the insertion is treated as a failure. Otherwise, the insertion is treated as a success.

Step 3: The above steps are repeated.

Step 4: Upon completion, the accessible volume is computed as

$$V_{acc} = V_{box} f = V_{box} \left( \frac{N_{suc}}{N_{tri}} \right) \quad (2.32)$$

where  $V_{box}$  is the volume of simulation box,  $f$  is the fraction of successful insertion, i.e. the solid-fluid interaction is non-positive,  $N_{suc}$  is the number of successful insertion and  $N_{tri}$  is the number of trial insertion. The surface excess of adsorption

$$\Gamma_{exc} = \frac{\langle N_{ps} \rangle - V_{acc} \rho_g}{S_s} \quad (2.33)$$

is evaluated as the excess amount as compared to a reference amount, where  $\langle N_{ps} \rangle$  is the ensemble average of the number of molecules in the system,  $\rho_g$  is the density of gas phase calculated using the equation of state and  $S_s$  is the surface area of the solid. The absolute pore density corresponding to accessible volume is calculated as follows:

$$\rho_{pore} = \frac{\langle N_{pp} \rangle}{V_{acc}} \quad (2.34)$$

where  $\langle N_{pp} \rangle$  is the ensemble average of the number of molecules in the pore. The absolute pore density (2.34) can provide a good description on how dense the adsorbed phase is.

### 2.2.7 Isosteric heat

The isosteric heat is referred to the heat of adsorption and also the infinitesimal change of the enthalpy of adsorbate over that of the excess adsorbed amount. In the GCMC simulation, the isosteric heat is calculated by considering the fluctuations of thermodynamic properties (Nicholson et al. 1982) as follows:

$$q_{st} = k_B T - \frac{f(U, N)}{f(N, N) - \bar{N}_G} \quad (2.35)$$

where  $\bar{N}_G$  is the number of molecules of an ideal gas occupying the adsorption space. Most of the adsorption work neglected the  $\bar{N}_G$  term because the molar volume of the adsorbed phase is smaller than that of the gas phase. As a result, the isosteric heat (2.35) can be rewritten as

$$q_{st} = k_B T - \frac{f(U, N)}{f(N, N)} \quad (2.36)$$

where  $U$  is the configuration energy of system and  $N$  is the number of molecules. The function  $f$  is defined as  $f(C, D) = \langle C, D \rangle - \langle C \rangle \langle D \rangle$ . This definition is only applicable for subcritical fluids and are invalid for supercritical fluids and subcritical fluids near to critical point conditions.

Do et al. (2009) then proposed and applied a differential isosteric heat in the canonical ensemble:

$$q_{st,diff} = k_B T - \frac{\partial \{ \langle U \rangle - \langle U_G \rangle \}}{\partial \{ N - N_G \}} \quad (2.37)$$

which is defined as the energy change of the adsorbed phase per unit change in the excess number, where  $U$  represents for the energy of the system,  $U_G$

stands for the energy of the bulk gas phase defined as

$$\langle U_G \rangle = \frac{V}{V_M} \langle U_M \rangle \quad (2.38)$$

with  $U_M$  and  $V_m$  denote the energy and volume of a region representing the bulk gas phase, respectively. The  $N_G$  represents for the hypothetical number of molecules that occupy the accessible volume at the same density as the bulk gas.

### 2.2.8 Henry constant

Henry's law expresses the amount adsorbed on the surface of a solid at low loading as a linear function of the bulk gas concentration. Given that the surface excess concentration

$$C = \frac{KP}{R_g T} \quad (2.39)$$

where  $P$  is the absolute pressure,  $R_g$  is the gas constant,  $T$  is the temperature of the system and  $K$  is the Henry constant. The Henry constant  $K$  is a measure of the interaction between a single molecule and the solid. It can be a useful tool to evaluate the interaction strength between a fluid molecular and adsorbent (Zeng et al. 2015).

## 2.3 Selectivity in binary mixtures

Gas mixtures can be separated by selective adsorption of one species in the adsorbent. The effectiveness of the separation can be quantified in terms of the selectivity (Buss 1995). For example, the equilibrium selectivity of  $\text{CO}_2/\text{CH}_4$  is defined as follows:

$$S_{\text{CO}_2/\text{CH}_4} = \frac{x_{\text{CO}_2}/x_{\text{CH}_4}}{y_{\text{CO}_2}/y_{\text{CH}_4}} \quad (2.40)$$

where  $x_{\text{CO}_2}/x_{\text{CH}_4}$  denotes the ratio of mole fractions of two species in the pore and  $y_{\text{CO}_2}/y_{\text{CH}_4}$  represents the ratio of mole fractions of two species in the bulk. If  $S_{\text{CO}_2/\text{CH}_4} > 1$ ,  $\text{CO}_2$  is preferentially adsorbed compared to  $\text{CH}_4$ . If  $S_{\text{CO}_2/\text{CH}_4} < 1$ ,  $\text{CH}_4$  is preferentially adsorbed.



## 2.4 IAST

The IAST theory defines the mixtures adsorption by mimicking the Raoult's law in vapor-liquid equilibrium (Myers and Prausnitz 1965). It assumes that the interactions between adsorbed molecules are equivalent, which is an ideal solution. The IAST is a thermodynamic framework for predicting multi-component adsorption isotherms from only the pure-component adsorption isotherms at the same temperature. IAST assumes that the adsorbed species form an ideal mixture, which is a reasonable approximation in many chemical systems (Myers and Prausnitz 1965). IAST is a powerful tool for providing practical mixed-gas adsorption measurements. Furthermore, considering all multi-component adsorption isotherm measurements may be impractical for cases where one is interested in several different mixture conditions only.

With the aid of reliable computational tools, Simon et al. (2016) developed a pyIAST program that can fit standard analytical isotherm models (Langmuir, Quadratic, Brunauer-Emmett-Teller (BET), approximated Temkin isotherm, and Henry's law) to the experimental data to characterize the pure-component isotherms. The pyIAST can interpolate the isotherm data for IAST calculations and handle an arbitrary number of components in the mixture. The pyIAST is also helpful for performing reverse IAST calculations, where one calculates the required gas phase composition to yield a desired adsorbed phase composition. In this thesis, IAST was applied by firstly considering the experimental single component isotherms (e.g., CO<sub>2</sub>, N<sub>2</sub>, CH<sub>4</sub>). They pyIAST is then used to fit the experimental multicomponent isotherm data and to predict the mixtures adsorption for comparison purposes (Simon et al. 2016).

## 2.5 Simulation Systems

### Phase equilibria system

As shown in Figure 2.1, the dense phase is placed at the middle of a rectangular simulation box and two bulk gaseous phases are connected at the two ends, forming two interfaces. Periodic boundary conditions are applied in all directions. The initial configuration of the dense phase is either solid slab or lattice structured liquid, depends on the temperature of the system is below or above the triple point.

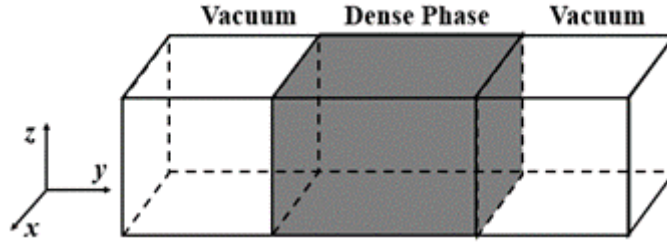


**Figure 2.1.** Schematic diagram of a phase equilibria system.

### 2.5.1 Adsorption systems

In the simulation of adsorption systems, a solid is located on the plane, which is perpendicular to the  $z$ -direction and no periodicity at this direction. Adsorption on a graphite surface can be simulated in two settings. Firstly, a uniform slit pore can be considered with a large pore width. Thus, the opposite walls can be taken as two independent surfaces as there is no overlapping between the potential energies. This setting is employed for an adsorption system with a high bulk gas density as well as to avoid the effects of the hard wall. Secondly, a graphite surface is placed at one boundary and a hard wall is placed at the opposite end. This setting is normally applied for an adsorption system under sub-critical conditions.

#### Graphitized carbon black

The graphitized carbon black is simulated as an infinite plane surface positioned at the bottom of the simulation box, as shown in Figure 2.2. Periodic boundary conditions are applied in both  $x$ - and  $y$ -directions. The length of each side  $L$  is set as 4 nm and the box height is 10 nm, which is large enough for the local density in the  $z$ -direction to closely approach the bulk gas density. The interaction between  $\text{CO}_2$  molecule and surface is calculated by the Steele 10-4-3 equation. The molecular parameters for a carbon atom in a graphene layer are  $\sigma_{ss} = 0.34\text{nm}$  and  $\varepsilon_{ss}/k = 28K$  and the carbon density of a graphene layer is  $\rho_s = 38.2\text{ nm}^2$ . The same parameters are also applied for the following two pore models, i.e. the slit and wedge pores.

#### Uniform slit pore

As shown in Figure 1.3(c), the pore width,  $H$  is defined as the distance between the plane passing through the centres of carbon atoms in the inner

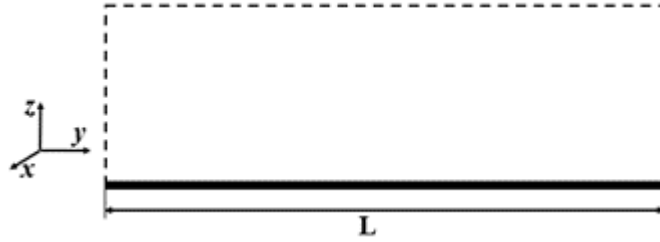


**Figure 2.2.** Schematic diagram of a graphitic surface.

layer of a wall and the plane of the opposite wall. The pore length,  $L$  can be infinite or finite, respectively. For infinite pore length, periodic boundary conditions are applied to both  $x$ - and  $y$ -directions. For finite pore length, periodic boundary condition is merely applied in the  $x$ -direction. There are two open pore ends connected to bulk gas reservoirs in the  $y$ -direction. The molecules in the pore can move and interact with bulk phase to maintain a mechanical equilibrium between the pore and the gaseous surroundings.

### Wedge pore

Figure 1.3(b) shows rather complex pore structure of the AC (Rosalind (1951)). Apparently, the carbon planes are not aligned and the pore spaces are displayed in wedges at different angles. The topological arrangement of the pores is dependent on the precursors and the method of preparation. Thus, a wedge pore can be a more realistic pore model for representing activated carbon. As shown in Figure 1.3(d), the wedge pore model can be characterized by several structural parameters including pore size at the narrow end,  $SH$ , the wedge angle,  $\alpha$ , and the length along the axial direction,  $L$ . The length of the wedge pore can be estimated based on the Raman spectroscopy (Inagaki and Kang 2014). The adsorption isotherm is then dependent on the pore size at the narrow end and the wedge angle. Also, the characterization of pore volume distribution can be expressed in the form of the pore size and wedge angle. When the wedge angle is equal to zero, the wedge pore model is reduced to a uniform slit pore model.

As shown in Figure 1.3(d), the pore walls contain three homogeneous graphene layers in the  $z$ -direction, which are finite in the axial  $y$ -direction and infinite in the  $x$ -direction. The dashed lines represent the boundaries of the simulation box in the  $y$ - and  $z$ - directions. The gas surrounding connected to each end of the pore has a length of 3 nm along the  $y$ -axis, and the

dimensions in the  $x$ -direction and  $z$ -direction are the same as the pore walls in that direction.

# Chapter 3

## Adsorption of CO<sub>2</sub> in Wedge Pores

### 3.1 Introduction

CO<sub>2</sub> is one of the greenhouse gases from natural gas purification and separation. Also, it is commonly used in characterizing the small pores of carbonaceous materials at 273K as it has smaller molecular size and faster diffusion rates than other commonly used probing gases, for example nitrogen. However, as most of the studies have been focused on the CO<sub>2</sub> adsorption at supercritical conditions, limited attention was paid to CO<sub>2</sub> adsorption at low temperatures below its bulk triple point (216.6K in experiment). Moreover, there has been no systematic study on the CO<sub>2</sub> adsorptive behaviour using the more realistic pore model, i.e. wedge pore at this low temperatures range. Although the temperature range used in this chapter is not directly related to the values in the practical application of CO<sub>2</sub> separation in natural gas industry, it compensates the knowledge gap in CO<sub>2</sub> adsorption in ACs, with new features been observed, which are absent at high temperatures. Regarding the pressure range for each temperature studied in this chapter, the corresponding saturated vapour pressures are applied. Under various conditions (i.e. pore geometry, temperature, corrugation and affinity), we have also examined in this chapter the occurrence and characters of hysteresis loop for CO<sub>2</sub> adsorption in wedge pore by Monte Carlo simulation. The mechanism of CO<sub>2</sub> adsorption in heterogeneous pores, especially at low temperatures, was understood further through this systematic study, together with the microscopic analysis presented.

## 3.2 Theory and Simulation

### 3.2.1 Wedge pore model

As shown in Figure 1.3(d), the wedge pore of  $SH = 2\text{nm}$ ,  $L = 10\text{nm}$  and  $\alpha = 5^\circ$  with smooth walls was taken as the reference wedge pore for comparison purpose. The main reason for choosing this dimension for wedge pore is to facilitate the special feature of the step-wised isotherm, which mainly exist in mesopores. The wedge angle is chosen as  $5^\circ$  so that the pore size range covered in the wedge remains in the meso-pore range. A corrugated wedge pore is constructed by grafting humps that composed of graphene-like layers in the same manner as the pore walls on the innermost graphene layers (see Figure 3.1). The configuration of the humps is included in the Sect. 3.3.5.

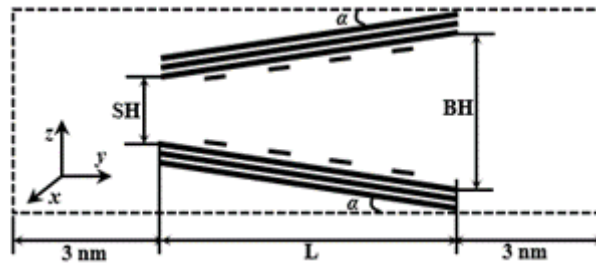


Figure 3.1. Schematic diagram of a corrugated wedge pore.

### 3.2.2 Potential model

The intermolecular potential energy of CO<sub>2</sub> is described by the 12-6 Lennard-Jones (LJ) equation and the solid-fluid interaction energy is calculated with the Bojan-Steele equation as presented in Sect. 2.2.1. The cross molecular parameters are calculated from the Lorentz-Berthelot combining rules. The molecular parameters of the 1C-LJ CO<sub>2</sub> are listed in Table 1.1.

### 3.2.3 Monte Carlo simulation details

The GCMC simulation was applied to determine adsorption and desorption isotherms, with at least  $5 \times 10^5$  cycles in both the equilibration and sampling stages. The values of saturated vapour pressures at different temperatures, as tabulated in Table 3.1, are determined from vapour-solid equilibrium (VSE) or vapour-liquid equilibrium (VLE) simulations with Bin-CMC scheme. The

experimental data of vapour pressure above triple point (i.e. 216.6K in experiment) in Table 3.1 were taken from the Lemmon et al. (2018). The experimental data of vapour pressure below triple point in Table 3.1 were taken from Terlain and Larher (1983) and Spencer et al. (1958). We employed the Bin-Canonical Monte Carlo (Bin-CMC) scheme to determine the VSE and VLE data for CO<sub>2</sub> at various temperatures.

The system for VSE simulation is initialized by placing a solid slab of  $7 \times 12 \times 7$  unit cells (i.e., 2352 CO<sub>2</sub> molecules) arranged in the *fcc* structure in the middle of an elongated simulation box with vacuum spaces on both sides of the slab. The main difference for VLE simulation is that the solid slab is replaced with a lattice having an initial density equals to the bulk liquid density at the boiling point of CO<sub>2</sub> (i.e.,  $3.55 \times 10^4$  mol/m<sup>3</sup>). The simulation box is divided into 25 bins and the bin size is smaller in the interfacial and condensed phase regions and larger in the gas phase region. We used  $6 \times 10^5$  cycles, with 1000 displacement moves in each cycle, in both equilibration and sampling stages to ensure the accuracy of the outputted data. Details of the Bin-CMC scheme can be found in Sect. 2.1.2.

**Table 3.1** Saturated vapour pressures of 1C-LJ CO<sub>2</sub> at various temperatures calculated with VLE/VSE simulations (simulated triple point = 172K) and with available experimental data (Spencer et al. 1958; Terlain and Larher 1983).

T (K)	150.0	155.0	160.0	173.0	194.7	216.6
$P_{0,sim}$ (kPa)	17.6	25.6	37.6	85.7	275.0	681.5
$P_{0,exp}$ (kPa)	0.8	2.5	2.8	10.1	93.0	443.0

## 3.3 Results and Discussion

### 3.3.1 CO<sub>2</sub> adsorption in the reference wedge pore at 150K

The isotherm of CO<sub>2</sub> adsorption at 150K in the reference wedge pore is presented in Figure 3.2(a). A Type C (de Boer Classification) or Type H2(b) (IUPAC classification) hysteresis is observed with three distinct steps (i.e., sharp evaporation) occurring on the desorption branch. To shed further light on the underlying mechanisms, the snapshots tracking the evolution of

adsorption and desorption processes are shown in Figure 3.3, with A-J points as labelled in Figure 3.2(a). All snapshots in this work are dimensionless units in the scale of collision diameter of 1C-LJ CO<sub>2</sub>,  $\sigma_{ff}$  (see Table 1.1).

From the points A to C in Figure 3.3(a), the mass starts building on the pore walls via layering until the critical conditions are reached which triggered the condensation and the pore is filled at the point D with two menisci formed. The pore is then further filled through the proceeding of the menisci to the pore mouths. This adsorption process is also evidenced by the isosteric heat of adsorption presented in Figure 3.2(b); the main characters are summarized as below.

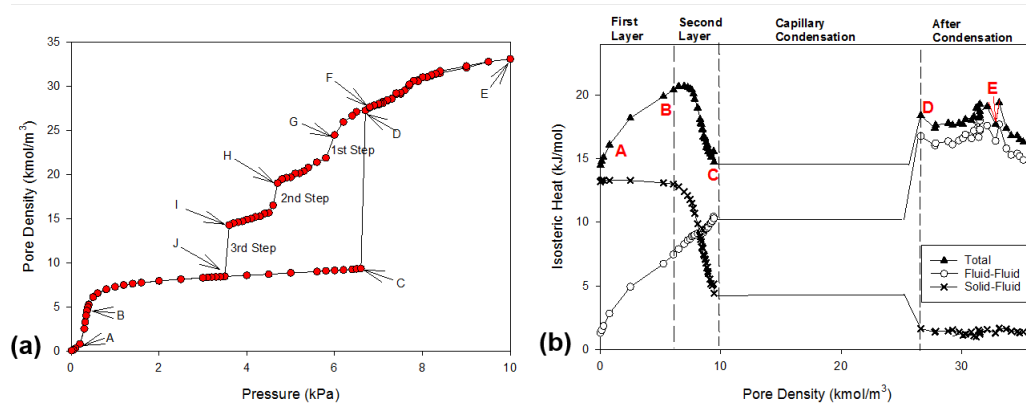


**Figure 3.2.** (a) Isotherm and (b) isosteric heat of 1C-CO<sub>2</sub> adsorption at 150K in the reference wedge pore of SH=2nm, L=10nm and  $\alpha=5^\circ$ , with the lines as guide to the eye.

- (a) The linear monotonic increment of heats released during the formation of the first adsorption layer, with the feature of constant solid-fluid contribution.
- (b) After reaching the maximum, the heat drops which indicates molecules start to adsorb on the second layer, which is further from the pore walls compared to the first adsorption layer, therefore solid-fluid interaction decreased.
- (c) Constant heat is observed when condensation occurs, corresponding to the sharp step in the isotherm.

At the point E, the snapshot in Figure 3.3(a) shows that five domains (labelled as I to V) are formed inside the pore. Each domain contains an



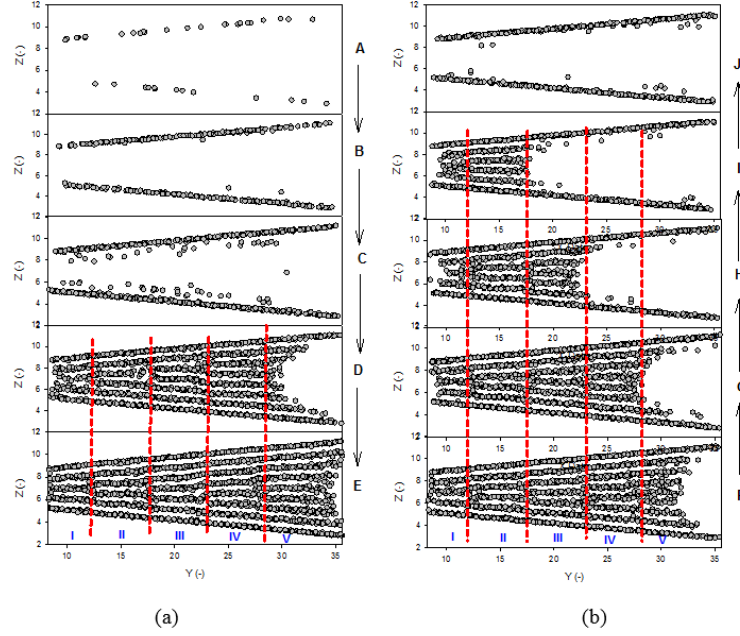


**Figure 3.3.** Snapshots of evolution of CO<sub>2</sub> adsorption at 150K in the reference wedge pore of SH=2nm, L=10nm and  $\alpha=5^\circ$ : (a) adsorption and (b) desorption. The points from A to J are as labelled in Figure 3.2.

integer number of layers (commensurate packing) with an increment of one layer between the two adjacent domains, bifurcated via the sections termed as junction (incommensurate packing) (Klomkliang et al. 2014).

As the pressure is decreased from point E to F, the menisci of both pore ends recede gradually into the pore, dominated by the one from the wider end. When the meniscus of the wider end approaches the junction between the domains IV and V (at Point G), where the adsorbate is less cohesive, a sharp evaporation is triggered due to the instant evaporation of molecules in domain IV, illustrated as the 1st step in the isotherm. Followed the sharp step is the gradual evaporation of the junction between domain III and IV. This evaporation process is repeated as the menisci are continued to recede, dominated by the meniscus at the wider end which proceeded through the domain III following by the domain II. This can be referred to the second and third steps in the isotherm (see Figure 3.2). It should be noted that the commensurate packing in the domain I is retrograded with the reducing pressure. Consequently, the remaining mass evaporates simultaneously with domain II at point J.

From Figure 3.3, the pore sizes corresponding to the junctions can be

obtained, which are  $6.14\sigma_{ff}$ ,  $7.12\sigma_{ff}$ ,  $8.07\sigma_{ff}$  and  $9.03\sigma_{ff}$ , respectively. The interval of the pore size of junctions is approximately  $0.96\sigma_{ff}$  and consistent with the results in Liu et al. (2019). The homogeneous slit pores with these pore sizes demonstrate incommensurate packing while those having pore sizes in between demonstrate commensurate packing (Liu et al. 2019).

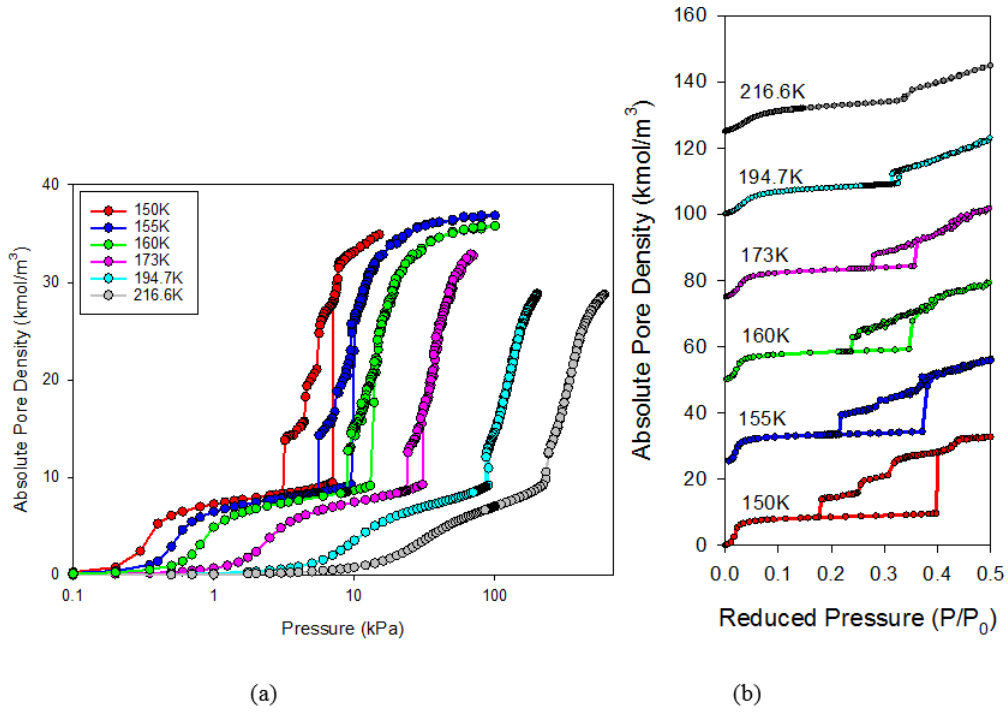
### 3.3.2 Effects of temperature

The adsorption isotherms of CO<sub>2</sub> in the homogeneous wedge pore within a temperature range of 150 - 216.6K are illustrated in Figure 3.4. The following features are observed,

- a) As the temperature increases, the hysteresis loop gradually transits from Type C (de Boer Classification) or Type H2(b) (in IUPAC) into Type A (or Type H1 in IUPAC) and then shrinks until it is completely disappeared at 216.6K.
- b) The distinct sharp steps formed in the desorption branch at 150K are gradually smoothed out at higher temperatures (160K in this case), indicating a critical temperature of this “stepwise” behaviour is between 155 and 160K for the reference homogeneous wedge pore.
- c) The stepwise desorption is originated from the alternation of commensurate and incommensurate packing along the pore axis direction. The higher thermal motion of particles at higher temperatures is adverse for packing, as further illustrated by the snapshots at various temperatures in Figure 3.5.
- d) The positions of the junctions (i.e., where incommensurate packing occurs) in a specific system are not affected by the temperature. However, with the increase of temperature, the adsorbate at the large open end become less structured and eventually propagate into the whole pore.

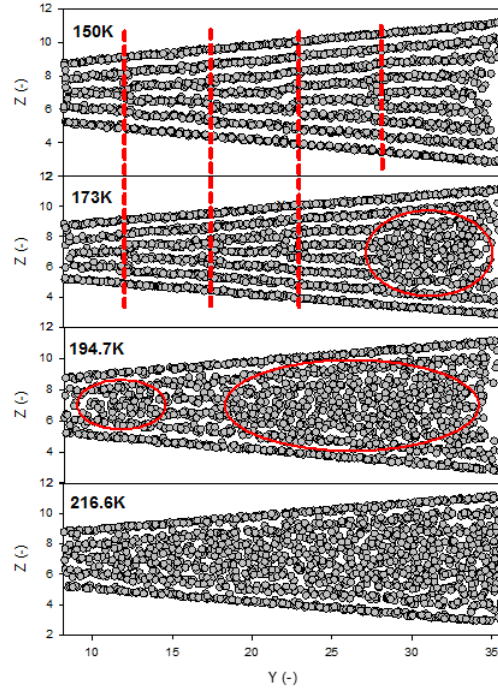
### 3.3.3 Effects of pore length

Figure 3.6 shows the isotherms at 150K for wedge pores of lengths 10 and 15nm with  $SH = 2\text{nm}$  and  $\alpha = 5^\circ$ . Figure 3.7 illustrates the comparison of the respective snapshots just after condensation and at pressure of 15kPa. The following observations can be made.



**Figure 3.4.** Isotherms of CO<sub>2</sub> adsorption at various temperatures in the reference wedge pore of SH=2nm, L=10nm and  $\alpha=5^\circ$  with (a) absolute pressure in log scale and (b) reduced pressure. Isotherms in (b) for 155K, 160K, 173K, 194.7K and 216.6K have been shifted up by  $n \times 25 \text{ kmol/m}^3$ , respectively.

- a) The condensation pressures are found almost identical for both pore lengths and the fraction of the adsorptive capacity associated with condensation is decreased with pore length. However, the sections occupied by the condensed fluid are identical for both pore lengths (as shown in Figure 3.7(a)).
- b) After initial condensation, two extra steps are observed for the longer pore on its adsorption branch. These steps are correlated to the formation of the two domains VI and VII as illustrated in Figure 3.7(b). These distinct steps are synchronized with the extra steps on desorption branch, which is in accordance with the result reported in Klomkiang et al. (2014), where this phenomenon also occurs in a wedge pore with a closed narrow end for argon at 77K. The reason is due to that similar scenario as a closed end as the particles accumulating to a certain quantity at the narrow end in the open wedge pore.



**Figure 3.5.** Snapshots at saturated pressures and various temperatures in the reference wedge pore of SH=2nm, L=10nm and  $\alpha=5^\circ$ .

### 3.3.4 Effects of angle

As shown in Figure 3.8(a), the isosteric heat of the wedge pore with tilt angle of  $2.5^\circ$  is similar as that of the reference pore, i.e.  $\alpha=5^\circ$ , except the peak shifts to higher loading. This is because larger tilt angle creates larger pore volume, with the same amount of adsorbate on the completion of the first adsorption layers, results in smaller pore density. For the case of corrugated wedge pore, the most interesting feature is for each step observed in the isotherm, the constant heat is found as seen in Figure 3.8(b).

The effects of angle on the isotherms of wedge pores with a constant SH of 2nm and the pore lengths of 10 and 15nm, are illustrated in Figure 3.9. When the angle is decreased from  $5^\circ$  to  $1^\circ$ , the adsorption and desorption branches shift to lower pressures due to the greater solid-fluid interaction exerted by the narrower average pore width. This enhanced solid-fluid interaction is also accounted for a higher saturation adsorption capacity. Moreover, the number of steps on desorption branch decreases along with a reduction in pore angle, indicating less domains are formed as shown in Figure 3.10.

Furthermore, the pore sizes corresponding to the junctions in these wedge pores are found to be consistent despite the variation of tilt angles. It is

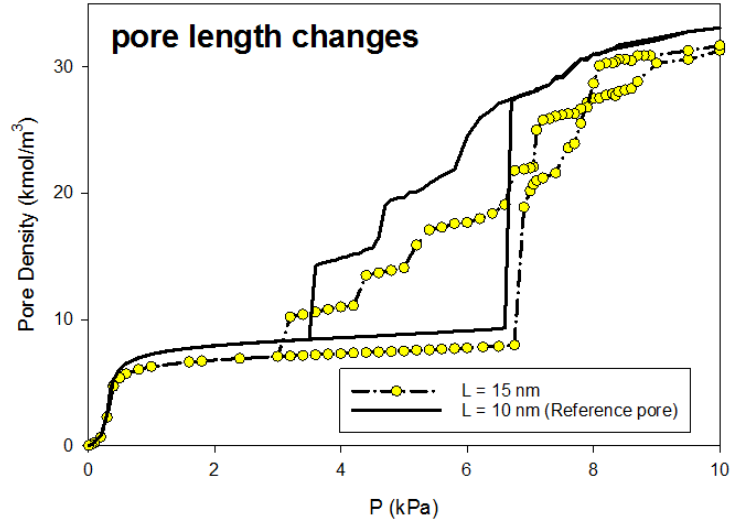


**Figure 3.6.** Isotherm for  $\text{CO}_2$  at 150K in the wedge pores of lengths 10 and 15nm,  $\text{SH}=2\text{nm}$  and  $\alpha=5^\circ$ .

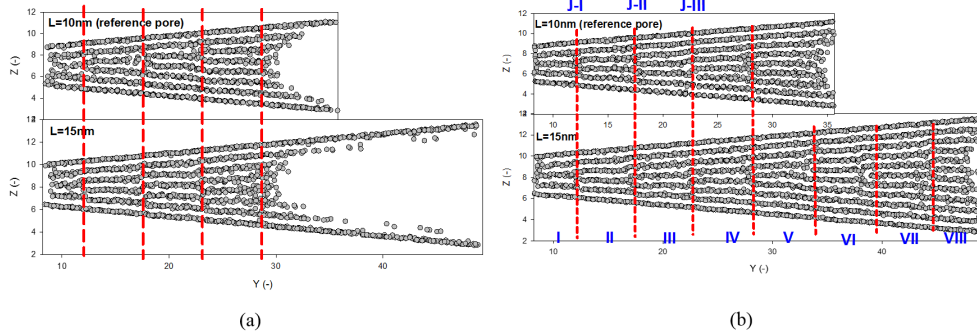


**Figure 3.7.** Snapshots of (a) just after condensation; (b) at 15 kPa for  $\text{CO}_2$  at 150K in wedge pore of lengths 10 and 15nm,  $\text{SH}=2\text{nm}$  and  $\alpha=5^\circ$ .

evident that the pore sizes of the junctions are specific and independent of the wedge angles. This feature could be potentially utilized to improve the characterization of porous materials. These observations are made in pores with smooth pore walls. The following section is to understand the effects of corrugated solid surface and the effects of non-uniformity of pore, both geometrically and energetically, along the pore axis on the adsorption behaviour and hysteresis.

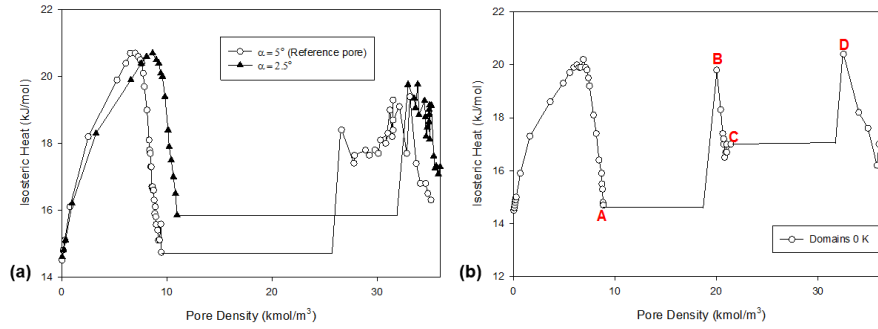


**Figure 3.8.** Isothermic heat curves for CO<sub>2</sub> adsorption at 150K (a) in the reference wedge pore ( $\alpha=5^\circ$ ) of SH=2nm and L=10nm, (b) in the corrugated pore with two double-layers humps grafted at the domains III and IV (see isotherm in Figure 3.13)

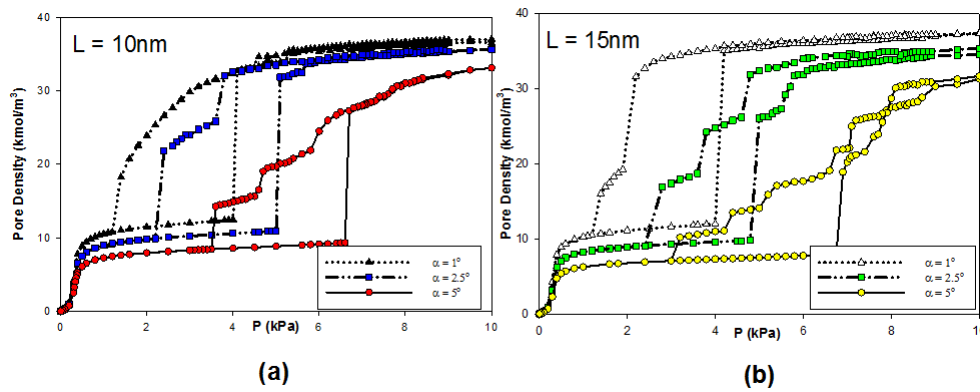


**Figure 3.9.** Isotherm for CO<sub>2</sub> at 150K in wedge pore of angles  $\alpha = 1^\circ$ ,  $2.5^\circ$  and  $5^\circ$ , SH=2nm, (a) L=10nm; (b) L=15nm.

### 3.3.5 Effects of corrugation

Pores in real porous materials do not have homogeneous surfaces, but possess geometrical corrugations, which are either as a result of impurities or defects acquired during synthesis or arise naturally as a consequence of discrete atomic structure. The effects of corrugation are examined by grafting small humps of 0.5nm width along the pore axis onto the reference wedge pore at 150K. The spacing between the humps and the homogeneous pore walls is kept as  $\Delta$  in graphite and the same affinity of pore was employed or otherwise stated. The configurations and properties of the humps are then elucidated for each case as follows.

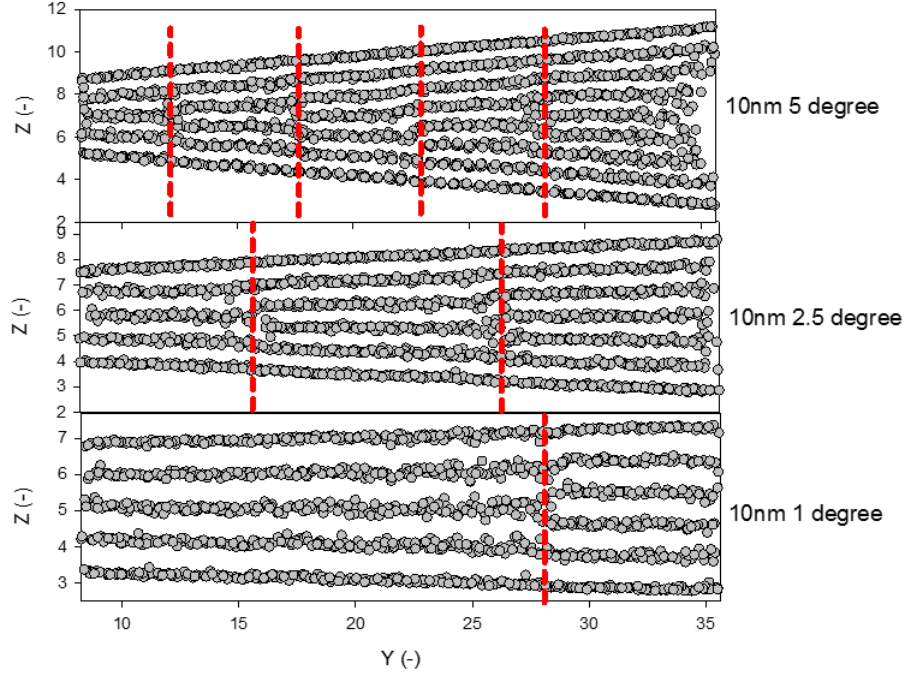


**Figure 3.10.** Snapshots at 10kPa and 150K in wedge pore of  $\alpha = 5^\circ$ ,  $2.5^\circ$  and  $1^\circ$ ,  $SH=2\text{nm}$ ,  $L=10\text{nm}$ .

### Effects of the positions of humps

Two pairs of double-layers humps (i.e. amplitude of  $2\Delta$ ) are grafted symmetrically on each side of the wall, with the center of the humps are aligned either with the junctions ( $y = 17.6 \sigma_{ff}$  and  $23 \sigma_{ff}$ , i.e. J-II and J-III in Figure 3.7(b)) or located within the domains ( $y = 19 \sigma_{ff}$  and  $25 \sigma_{ff}$ , i.e. III and IV in Figure 3.7b). The isotherms are presented in Figure 3.11 with the isotherms in the reference homogeneous wedge pore for comparison purpose.

In the reference homogeneous wedge pore, the evaporation of the domains IV and III are corresponding to the first and second steps (see Figure 3.3), respectively, while the junctions J-II and J-III is accounted for the plateaus before reaching the second and third steps, respectively. By adding the humps at these positions, we can make the following observations:

- a) The condensation occurs at a lower pressure when there are humps grafted to the pore walls, due to the enhanced solid-fluid interaction compared to the reference wedge pore.
- b) In the corrugated pores, a new hysteresis is observed after the condensation, the one obtained with humps grafted at J-II and J-III is more

pronounced.

- c) When the humps are located within the domains III and IV, a same number of steps is observed in the major hysteresis as the reference wedge pore. However, the first step shifts to a higher pressure and the contrary was seen for the second and third steps. From the snapshots in Figure A.1 (Appendix A), the first step is caused by the partial evaporation of the domain IV. The fraction between the two humps is retained and evaporated gradually as the plateau in the isotherm. The same mechanism is applicable for the second and third steps.
- d) By changing the positions of the humps to the junctions J-II and J-III, the step numbers of the major hysteresis were reduced from three to two. The first step shifts to a lower pressure due to the enhanced junctions with the presence of humps. Subsequently, the second and third steps are merged into one and evaporated at the pressure of the third step as of the reference case. This is due to the packing of the domain III was reinforced by the presence of humps.

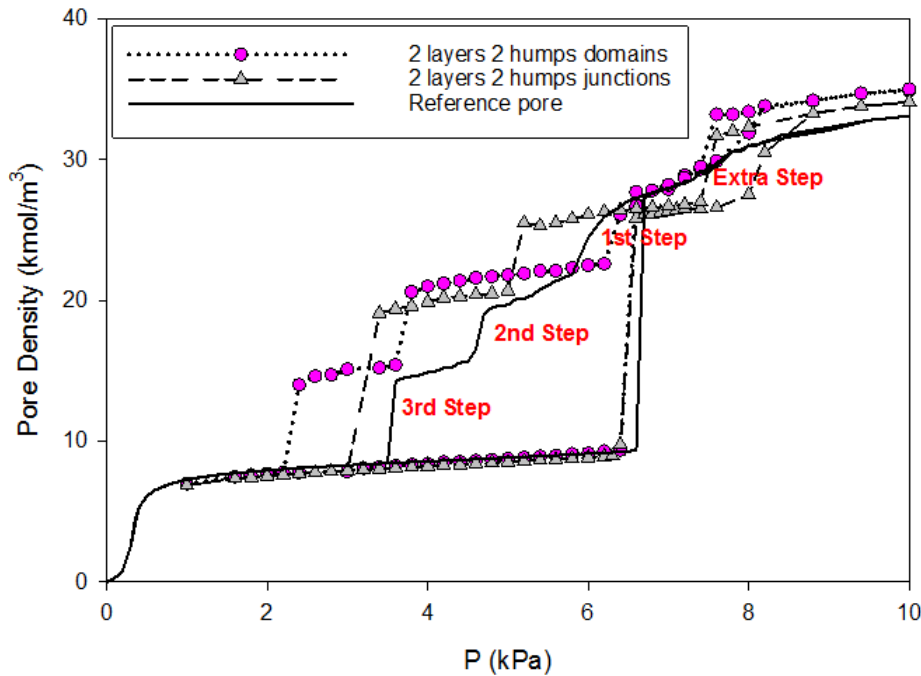


**Figure 3.11.** Isotherms of adsorption in pores with two pairs of double-layers humps grafted on the pore walls at domains and junctions.



To illustrate the effects of number of humps, an extra pair of humps is grafted to the pore walls based on the configurations presented in Figure 3.7(b), the centres of the humps are allocated at  $y = 12 \sigma_{ff}$  and  $13 \sigma_{ff}$ , respectively, for the scenarios of located at junctions and within domains. The adsorption isotherms are shown in Figure 3.12 and exhibit a stepwise behaviour in both adsorption and desorption branches, and formed multiple (fused) loops. Similar mechanisms can be seen from the experimental isotherms of noble gases in the nanoporous material (Ravikovitch and Neimark 2002b).

With the increasing number of humps at domains and junctions, we can see from Figure B.1 (Appendix B) that the wedge pore turns into a pore structure similar to an ink-bottle pore comprised of necks and cavities. The condensation occurs sequentially in the cavities, advancing from the small to the large end, and exhibited as the sharp steps in the adsorption branch. The necks between two adjacent domains filled gradually by pore filling and correspond to the plateaus in the isotherm. This adsorption process is identical as the case of weak humps that presented in Figure 3.13. The evaporation mechanism is cavitation-like pore blocking (Nguyen et al. 2013), with two menisci recede into the pore interior, again the sharp steps in the desorption branch reflect the evaporation of the domains.

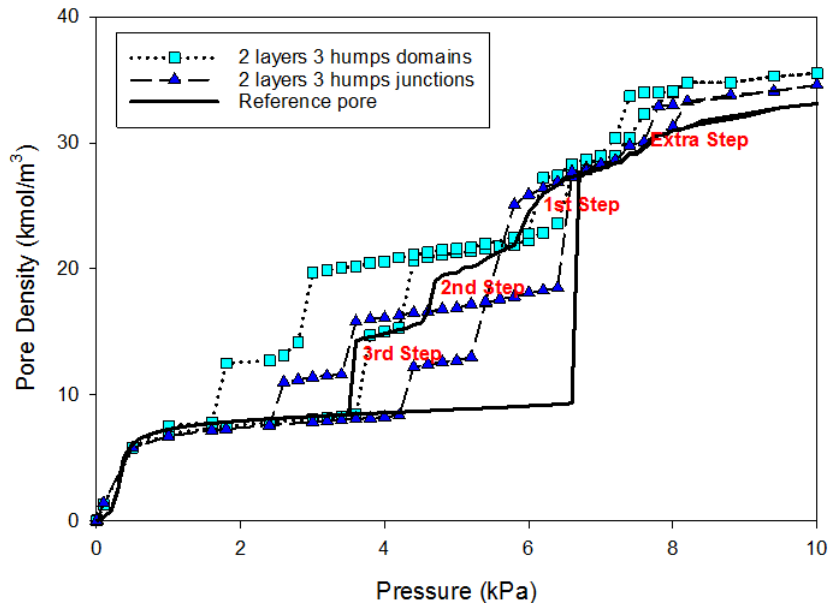


**Figure 3.12.** Isotherms of adsorption in pores with three pairs of double-layers humps grafted on the pore walls at different locations.

### Effects of the affinity of the humps

Given the same affinity of the humps and the pore walls, the average pore size of the corrugated pore was smaller than the corresponding homogeneous wedge pore, hence stronger forces exerted to the adsorbate, as illustrated in the previous sections. Very often in practical applications, the impurities embedded in the solid have weaker affinity than carbon. For an extreme case, there is no interaction between the humps and the solid, and this is realized by setting the well depth,  $\varepsilon_{ss}/k = 0K$  for the humps in this work. Figure 3.13 presents the comparison of the adsorption isotherms between the strong humps ( $\varepsilon_{ss}/k = 28K$ ) and weak humps ( $\varepsilon_{ss}/k = 0K$ ), where two pairs of humps are grafted within the reference wedge pore in the domains III and IV. The snapshots of the points A-J as labelled in Figure 3.13 are shown in Figure 3.14 to facilitate the understanding of the underlying mechanism.

Some key features are described as follows:

1. The condensation pressure shifts to a higher pressure as the total affinity of the pore walls is decreased due to the lower solid-fluid interactions.
2. With the presence of weak humps, multiple steps are formed in the adsorption branch. Interestingly, as illustrated in Figure 3.14, the sharp condensation is corresponding to the formation of domains, while the development of the junctions is demonstrated as plateaus in the isotherm.
3. In the desorption branch, the domain R5 was not affected by the grafted weak humps. Therefore, the evaporation process from the saturated pore follows the comparable path as that of the reference homogeneous wedge pore. The sharp step of point H to I corresponds to the simultaneous evaporation of two domains R3 and R4, different from the sequential evaporation as in the reference wedge pore, due to the weakened packing within the two domains.

The humps with strong affinity enhance the packing of the adsorbate, hence, this enhanced packing retains the steps and yet affects the pressures at which the steps occur. On the other hand, the humps that have low affinity interfere the structure of the adsorbate, especially towards the domains. Therefore, this interference in structure of the adsorbate accounts for diminished number of the steps.

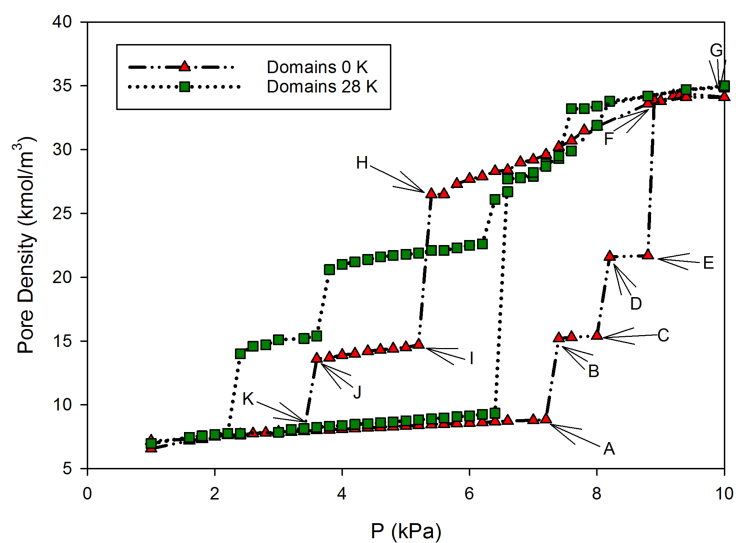


**Figure 3.13.** Isotherms for  $\text{CO}_2$  at 150K in wedge pore having two humps with two layers at domains (well depth = 28K and 0K).

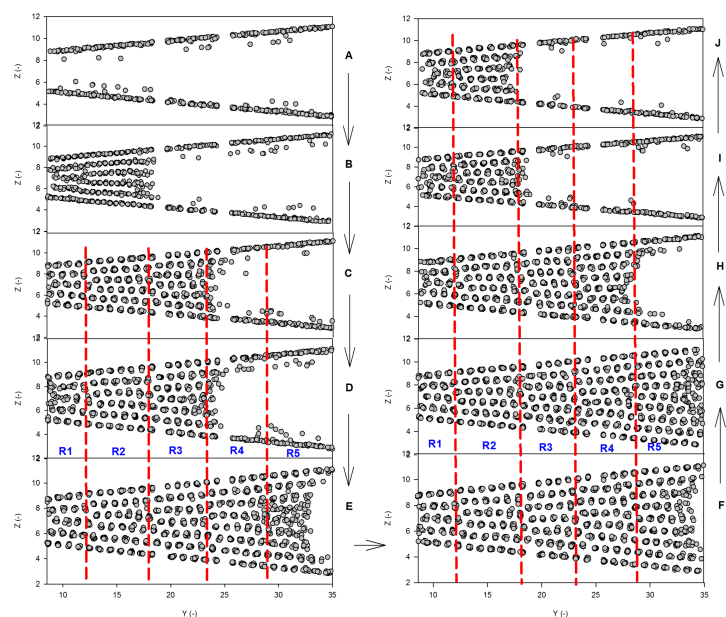


**Figure 3.14.** Snapshots of  $\text{CO}_2$  adsorption at 150K in the wedge pore containing two layers two humps (well depth = 0K) corresponding to the points A to J in Figure 3.13. The dashed lines are labelled at the same positions as in Figure 3.2, i.e. the positions of the junctions.

### 3.4 Summary

We investigated CO<sub>2</sub> adsorption and its stepwise behaviour under subcritical conditions in mesoporous wedge pores using the GCMC simulation. We found that the stepwise desorption behaviour in wedge pores can be a unique characteristic of any adsorbate using a single-site molecular model. For a given wedge pore, there exists a critical temperature for the occurrence of stepwise desorption. Low temperature facilitates the formation of ordered structures in the wedge pore and steps of desorption branch. As temperature increases, disordered structures are likely to occur at the wide end and then proceed at the narrow end, until propagated to the entire pore. For a given adsorbate, the pore sizes for junctions are fixed, specific and independent of temperature or pore tilt angle. The number of steps occurred during desorption is dependent on the number of alternating packing of junctions and domains inside the pore. Grafting humps on the interior surface of wedge pore at different positions, i.e. at junctions or domains, not only can retain the stepwise desorption as more ordered structure is formed, but also facilitate the formation of steps in the adsorption branch. With more humps grafted on the pore walls, the wedge pore resembles the characteristics of ink-bottle pore and evaporate via cavitation-like pore blocking mechanisms.

# Chapter 4

## Effects of CO<sub>2</sub> Potential Model

### 4.1 Introduction

A number of intermolecular potential models for CO<sub>2</sub> have been proposed in the literature as presented in Sect. 1.2.1. This chapter aims to evaluate two models of CO<sub>2</sub>, which are 1C-LJ and TraPPE, on their performances within different scenarios, including the vapor-liquid/solid equilibrium (VLE/VSE) of bulk phase, adsorption on graphite surface, and in slit pores and wedge shaped pores. The 1C-LJ model simulates the CO<sub>2</sub> in a spherical shape with single LJ site and no charge, therefore, no quadrupole moment included. The TraPPE model (i.e. 3C-LJ+3Q) is triatomic model comprising three dispersive interaction sites, located on each atoms, and three discrete charges are assigned at the same locations to consider high quadrupole moment of CO<sub>2</sub>, and it has a elongation shape compared to the 1C-LJ. The main tool applied in this chapter is MC simulation as presented in Sect. 2.1.

Adsorption of CO<sub>2</sub> with carbonaceous materials has been one of the commonly applied approaches of carbon capture and storage. To improve this technology, it necessitates understanding of the underlying mechanisms, for which molecular simulation has been recognized as a useful tool and compensation of experimental study. However, to ensure the reliability of the simulation results, the selection of the reliable potential model is vital. A systematic Monte Carlo simulation was conducted to evaluate the performance of two commonly used potential models of CO<sub>2</sub>, i.e. the simple 1C-LJ and the TraPPE 3C-LJ+3Q models, in different scenarios including bulk phase, adsorption on graphite surface and in carbonaceous pores. And a special investigation on the occurrence of step-wised hysteresis in wedge shaped pore

that has been observed with 1C-LJ CO<sub>2</sub> and other simple gases. It reveals the consideration of shape and quadrupole of CO<sub>2</sub> plays an important role in the description on the phase equilibria and adsorption behavior, especially at temperatures below the triple point.

## 4.2 Theory and Simulation

### 4.2.1 Potential models

The corresponding molecular parameters for the two selected potential models of CO<sub>2</sub>, i.e. the 1C-LJ and TraPPE (3C-LJ) are listed in Table 1.1. The interaction energy between two CO<sub>2</sub> molecules  $i$  and  $j$  is given by the sum of the LJ and Coulomb interaction as presented in Sect. 2.2.1.

The solid-fluid interaction energy is calculated by the Bojan-Steele equation. The parameters of the solid (i.e.  $\sigma_{ss}$  and  $\varepsilon_{ss}/k_B$  for a carbon atom in a graphene layer), carbon density of a graphene layer and spacing between adjacent graphene layers are given in Sect. 3.2.1.

### 4.2.2 Simulation systems

Four simulation systems used in this chapter are bulk phase equilibria (VLE and VSE), graphitized carbon black, uniform slit pore and wedge pore. The corresponding schematic diagrams are presented in Sect. 2.5.

For the graphite surface, the length of each side  $L$  is set as 3 nm and the box height is 10 nm. For the slit and wedge pores, the pore wall parameters are listed as  $L = 8.5$  nm,  $SH = 2$  nm and  $\alpha = 5^\circ$ .

### 4.2.3 Monte Carlo simulation

#### Bin-canonical Monte Carlo

To ensure the accuracy of output data, at least  $8 \times 10^5$  cycles were employed, with 1000 displacement moves in each cycle, in both the equilibration and sampling stages. More details can be found in Sect. 2.1.2.

#### Grand canonical Monte Carlo

As described in Sect. 2.1.1, at least  $5 \times 10^5$  cycles were employed in both equilibration and sampling stages to obtain the adsorption isotherm and

structural properties. Each cycle consists of 1000 displacement moves, insertion and deletion with equal probability. As a result, this generated a total of  $5 \times 10^8$  configurations.

## 4.3 Results and Discussion

### 4.3.1 VSE/VLE of CO<sub>2</sub>

The VSE/VLE coexistence curves of CO<sub>2</sub> obtained with two models are shown in Figure 4.1 and compared against the experimental data (cross symbols). The experimental data above triple point (i.e. 216.6K in experiment) in Figure 4.1 were taken from the Lemmon et al. (2018). The experimental data of vapour pressure below triple point in Figure 4.1(c) and (d) were taken from Terlain and Larher (1983) and Spencer et al. (1958). The experimental solid phase density and sublimation heat below triple point in Figure 4.1(a), (b) and (e) were taken from Chen et al. (2001). The simulated results of both models (red circle for 3C-LJ model and blue circle for 1C-LJ model) covered from below the triple point up to near the critical point (i.e. 304.2 K in experiment). Compared with the 1C-LJ model, the simulation results of the 3C-LJ model agree better with those reported experimentally. The following observations can be made:

1. At temperature below triple point, compared with the 3C-LJ, the 1C-LJ model is inadequate in describing the experimental data, including the densities of gas and solid phases, the saturated vapor pressure and sublimation heat. However, the deviation is negligible for temperatures greater than 230 K.
2. Both models capture the discontinuity in the branch of the dense phase density (see Figure 4.1(a)) as well in the enthalpy of phase change (see Figure 4.1(e)), which corresponds to the triple point. However, the prediction made by 3C-LJ model (216 K) is much closer to the experimental value (216.6 K), compared to that of the 1C-LJ model (172 K).
3. For surface tension (Figure 4.1(f)), 1C-LJ model predicts the correct trend of surface tension, and performs better than the 3C-LJ model.

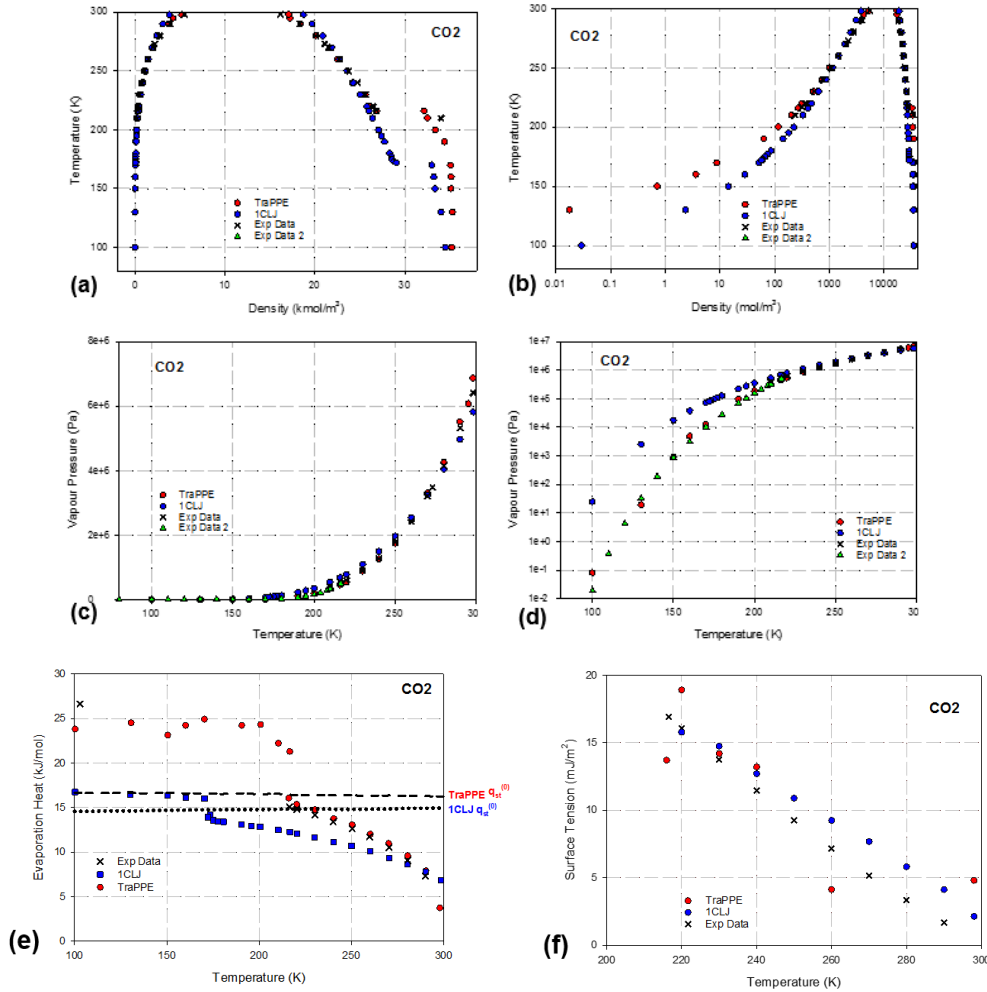


**Figure 4.1.** Thermodynamic properties of 1C-LJ and TraPPE 3C-LJ potential models at various temperatures obtained with Bin-CMC as compared to the experimental data, (a) liquid (solid)–vapour coexistence curve in linear scale, (b) liquid (solid)–vapour coexistence curve in semi-log scale, (c) vapour pressure in linear scale, (d) vapour pressure in semi-log scale, (e) evaporation (sublimation) heat and (f) surface tension. Statistical uncertainties are smaller than the size of the symbols used in the above figures.

The values of triple points predicted by the 1C-LJ and TraPPE 3C-LJ models are different. To ensure the two models have similar thermodynamic properties for adsorption study, the so-called equivalent temperatures applied for the 1C-LJ and 3C-LJ potential models are correlated as follows:

$$T_{1C}^{Tr} - T_{1C} = T_{3C}^{Tr} - T_{3C}, \quad (4.1)$$

where  $T_{1C}^{Tr} = 172$  K and  $T_{3C}^{Tr} = 216$  K. The temperatures applied for the 1C-LJ



and 3C-LJ potential models (4.1) can be rewritten as

$$T_{3C} = T_{1C} + 44K. \quad (4.2)$$

The corresponding temperatures used are then calculated for the 1C-LJ and 3C-LJ potential models and are shown in Table 4.1, where T1 denotes a temperature below the triple point and T2 denotes a temperature above the triple point. The saturation vapour pressure of CO<sub>2</sub> at several temperatures are calculated using Bin-CMC simulations and are presented in Table 4.2 and Table 4.3 for 1C-LJ and 3C-LJ potential models, respectively.

**Table 4.1** The corresponding temperatures used for 1C-LJ and 3C-LJ potential models.

CO <sub>2</sub> Potential model	1C-LJ	3C-LJ
T1 (below triple point)	150K	194K
T2 (above triple point)	229K	273K

**Table 4.2** Saturation vapour pressures of CO<sub>2</sub> at various temperatures for 1C-LJ potential model (Triple point = 172K).

T (K)	150	155	160	173	194.7	216.6	229	273	298
P <sub>0</sub> (kPa)	17.62	25.61	37.55	85.69	275	681.5	1060	3468	5820

**Table 4.3** Saturation vapour pressures of CO<sub>2</sub> at various temperatures for 3C-LJ potential model (Triple point = 216K).

T (K)	150	160	170	180	194	273	298
P <sub>0</sub> (kPa)	0.896	4.848	12.304	42.229	99.7	3479	6422

### 4.3.2 Adsorption on graphitic surface

The accessible volume [see eqs. (2.32), (2.33)] is determined for each potential model and applied in the calculation. It is shown in Figure 4.2, the potential profile of CO<sub>2</sub> molecule as a function of distance between its mass center to the solid surface, the 3C-LJ model exhibits deeper well-depth, and closer zero-potential distance to the surface, implying larger  $V_{acc}$  obtained with the 3C-LJ model. This is in good agreement with the result of Do and Do (2006a).

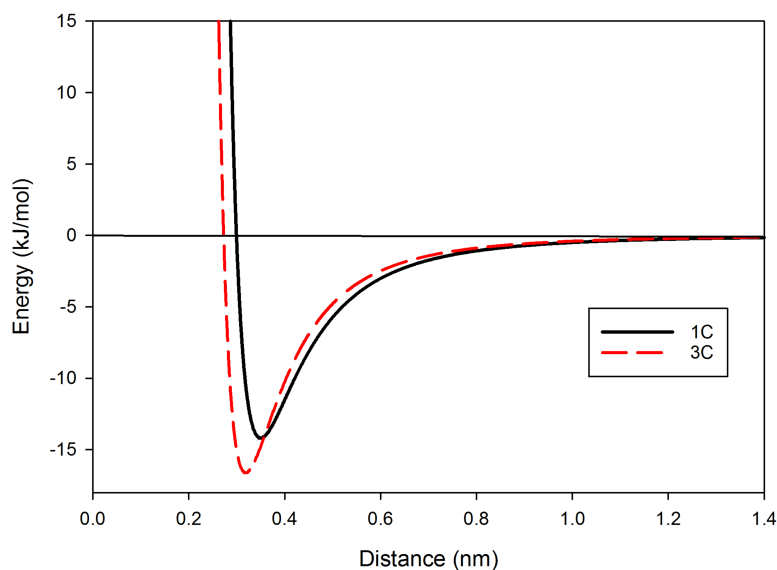


**Figure 4.2.** Profile of solid-fluid potential energy versus the distance between the mass center of CO<sub>2</sub> molecule to the solid surface, 3C-LJ model is parallel to the surface to maximize the potential.

### Adsorption isotherms

Figure 4.3 shows the surface excess adsorption isotherms on graphite at several temperatures for the 1C-LJ and 3C-LJ models, and the comparison with the experimental data at 194K (Spencer et al. 1958) and 273K (Guillot and Stoeckli 2001).

### Below triple point

At the temperature of 194K, which is below the bulk triple point, the 3C-LJ model describes the experimental data better than the 1C-LJ model, produces the same monolayer capacity as in experiment, while the 1C-LJ model over-predicts it. Both models capture the occurrence of the incomplete wetting, i.e. with finite number of layers formed at the saturated vapor pressure, which are consistent with the results reported in Xu et al. (2019). However, with the 1C-LJ model, at 150K there are four distinct sharp steps recognized, indicating four layers are formed through the first order transition. The steps are no longer observed when temperatures are greater than 150K for the 1C-LJ model.

The snapshots of the monolayer for 1C-LJ model at 150K and 3C-LJ model at 194K are presented in Figure 4.3(c) and (d), different configurations

are observed for the two models, which are the hexagonal packing by the 1C-LJ model and the 3C-LJ particles are mainly lying flat on the surface.

### Above triple point

In Figure 4.3(b), a Type II adsorption isotherm is observed for both models at temperature above the triple point, with continuous wetting observed, i.e. the loading approaches infinity asymptotically with pressure increased to the bulk vapor pressure. The isotherm obtained by the 1C-LJ model at 273K is almost identical with that at the equivalent temperature 229K and trace the experimental data in general well. In the sub-monolayer region, a good agreement is observed with both the 1C-LJ and 3C-LJ models, the latter diverts from the rest after the completion of the monolayer though, implying better performance of the 1C-LJ model at the high loading region. To shed further light on these observations, Henry constant of the models on graphite surface is analyzed.

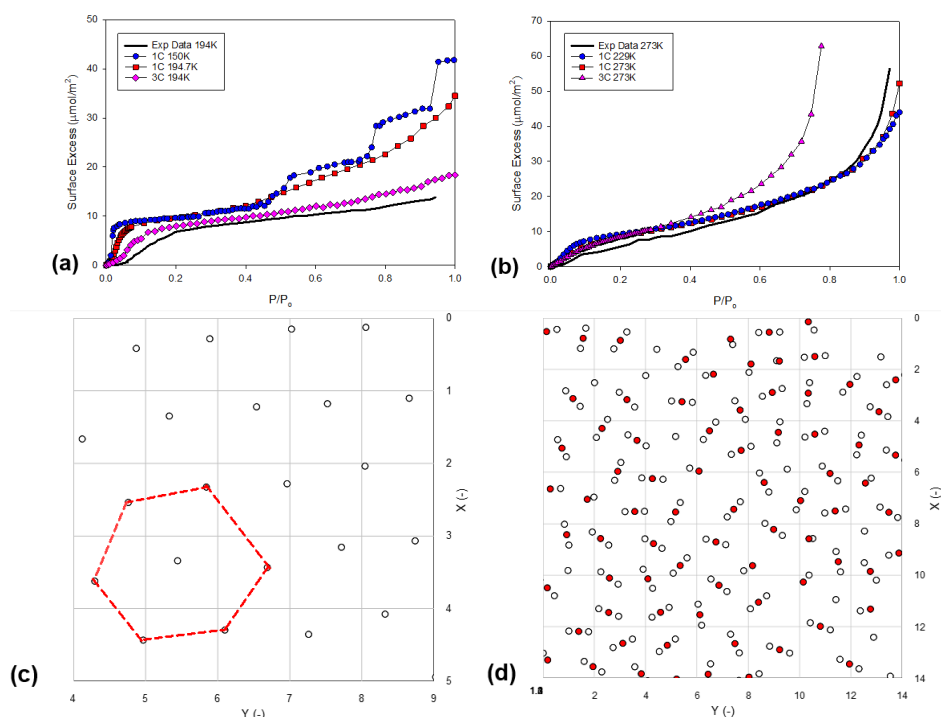


**Figure 4.3.** Comparison of adsorption isotherms on graphitic surface at temperatures of (a) 194K and (b) 273K for both models and monolayer snapshots of  $\text{CO}_2$  for (c) 1C-LJ model at 150K and (d) 3C-LJ model at 194K, both at  $P_0$ .

### Henry constant

The Henry constant  $K$  in eq. (2.39) is dependent on the exponential of the reciprocal temperature and is therefore lower at higher  $T$ . To reveal the effect of adsorbent interactions and the influence of the adsorbate–adsorbate interaction, the surface excess concentration eq. (2.39) can be rewritten as follows:

$$C = \frac{K'}{R_g T} \left( \frac{P}{P_0} \right), \quad (4.3)$$

where  $K' = KP_0$  is a modified Henry law parameter,  $K$  represents the Henry constant and implies for the adsorbate–adsorbent interaction, and the saturation vapour pressure  $P_0$  denotes the parameter for the interaction between adsorbate molecules. As a result, the implication of  $K'$  is the relative importance of these two interaction potentials.

As shown in Figure 4.4, as temperature  $T$  increases, the measured parameter of the adsorbate–adsorbent interaction  $K$  decreases while the measured parameter of the adsorbate–adsorbate interactions  $P_0$  increases and the temperature dependence of  $K'$  therefore provides a mean of estimating the relative importance of these two interactions. If  $K'$  decreases with temperature  $T$ , then the adsorbate–adsorbent interaction tends to be dominant. On the other hand, the adsorbate–adsorbate interaction potentials would be great as  $K'$  increases with temperature  $T$  (Nguyen et al. 2013). For 3C-LJ model, the modified Henry constant ( $K'$ ) increases with temperature  $T$ , indicating that the adsorbate–adsorbent interaction is weaker than the intermolecular interaction between CO<sub>2</sub> molecules. However, 1C-LJ model has a decreased in the modified Henry constant ( $K'$ ), implying that the adsorbate–adsorbent interaction is stronger than the intermolecular interaction between CO<sub>2</sub> molecules. These results also indicate that the 1C-LJ model tends to be hydrophilic on graphitic surface while the 3C-LJ model tends to be hydrophobic on graphitic surface. This explains (1) at the same/equivalent temperature, the monolayer is built up with a greater rate with the 1C-LJ than the 3C-LJ model (see Figure 4.3(a) and (b)); (2) the saturated loading of 3C-LJ model is lower than the 1C-LJ model at low temperature; (3) as the temperature is increased, i.e. higher thermal mobility, adsorbate–adsorbate interaction become more dominating, a thick adsorbed film is formed by the 3C-LJ model at a coexistence pressure  $P_0^*$  that is smaller than the bulk saturated vapor pressure  $P_0$ .

Furthermore, the comparison between the heat of evaporation and the

isosteric heat of adsorption at zero loading  $q_{st}^{(0)}$  is an indication of the occurrence of the wetting or non-wetting behavior for the adsorbate/adsorbent pair. The heat of evaporation is a measure of the cohesion in the bulk, while the  $q_{st}^{(0)}$  is a measure of adhesion strength to the surface. As shown in Figure 4.1(e), for both models, without considering the adsorbate-adsorbate interactions, the triple points demarcate the wetting and non-wetting temperature ranges, that is, the  $q_{st}^{(0)}$  is smaller than sublimation heat when below the triple point, non-wetting is expected. However, this demarcation can be affected when the amount of adsorbate is increased (Xu et al. 2019). This is illustrated in Figure 4.3(a), incomplete wetting is observed at temperatures below the triple points for both models.

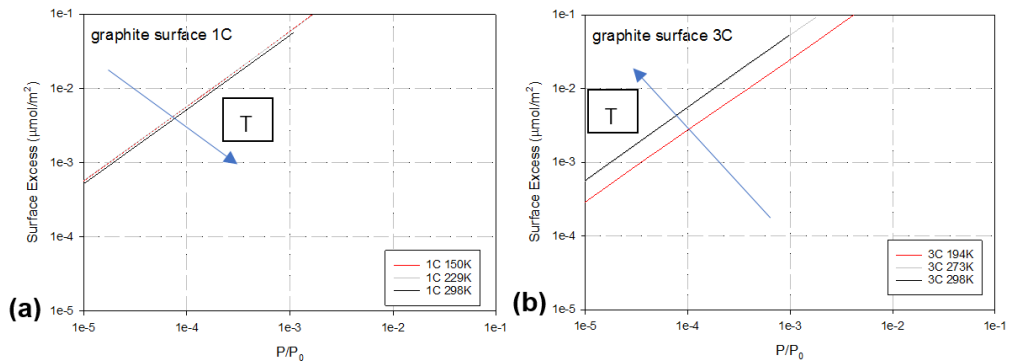


**Figure 4.4.** Comparison of adsorption isotherms (on a logarithmic scale) on graphitic surface at various temperatures for (a) 1C-LJ and (b) 3C-LJ models.

### 4.3.3 Adsorption in slit pores

#### 298K

Figure 4.5 presents the adsorption isotherms at 298K of the 1C-LJ and 3C-LJ models in two slit pores, with widths of 2nm and 3.5nm, both of which fall in the mesopore range, and corresponds to the SH and BH of the wedge pore defined in this chapter. Identical reversible type I (IUPAC) adsorption isotherms are observed in the 2nm slit pore, while divergence appeared when the pore size is enlarged to 3.5nm. The two CO<sub>2</sub> models predict almost the same adsorption capacities for the two pore sizes selected, with the 3C-LJ model produces slightly higher saturation densities. This agrees with Do and Do (2006a) that for slit pore with sizes larger than 1.5nm, the packing

effects caused by the shape of the molecules is negligible. As the pore size is increased to 3.5nm, there is a reflection point observed for both models, with the 3C-LJ model reaches the reflection point at lower reduced pressure, due to the stronger intermolecular interaction by considering the quadrupole interaction.

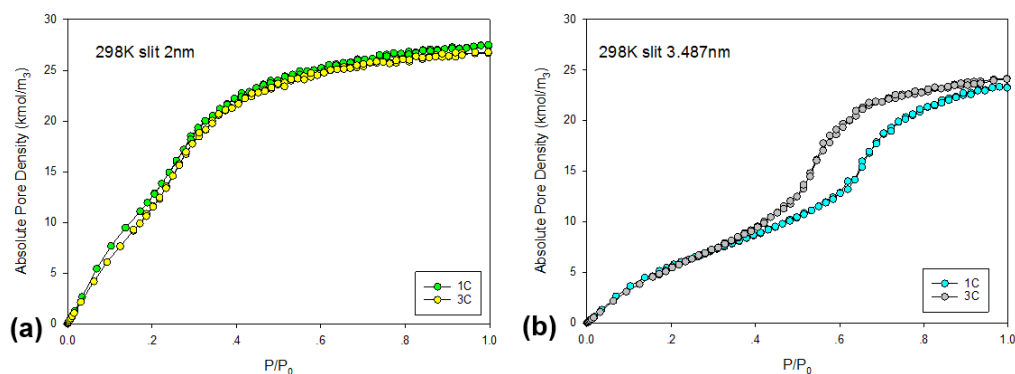


**Figure 4.5.** Comparison of adsorption isotherms at 298K for 1C-LJ and 3C-LJ models in slit pores with the pore size of (a) 2 nm and (b) 3.5 nm.

#### At equivalent temperature at T1- below triple point

Figure 4.6 shows the isotherms at T1 in two slit pores, the 1C-LJ and 3C-LJ models diverge from one another in both slit pores. The following observations can be made:

1. Although incomplete wetting occurred for adsorption on graphite surface (see Figure 4.3(a)), due to the enhanced force field with the presence of the opposite wall, in 2nm slit pore, Type HI hysteresis according to the IUPAC classification are observed for both 1C-LJ and 3C-LJ models. However, the 1C-LJ model predicts a larger hysteresis and higher saturation loading, which is even higher than the bulk density despite that the two models predict similar bulk density at T1 (see Figure 4.1(a)). Moreover, the condensation and evaporation occurred at higher reduced pressures with the 3C-LJ than the 1C-LJ model.
2. In the 3.5nm slit pore, Type H1 hysteresis is again observed with 1C-LJ model and condensation and evaporation occur at higher pressures compared to in the 2nm slit. However, the 3C-LJ CO<sub>2</sub> failed to condense with incomplete wetting occur on pore walls.

- In the low pressure region, the two pore walls act as two independent graphite surfaces, therefore, identical features observed earlier with adsorption on graphic surfaces are again captured here. That is the monolayer of the 1C-LJ model is formed at lower reduced pressure and picked up with a rather sharp manner than the 3C-LJ model, due to the 1C-LJ model has stronger interaction with the solid substrate than the 3C-LJ model.

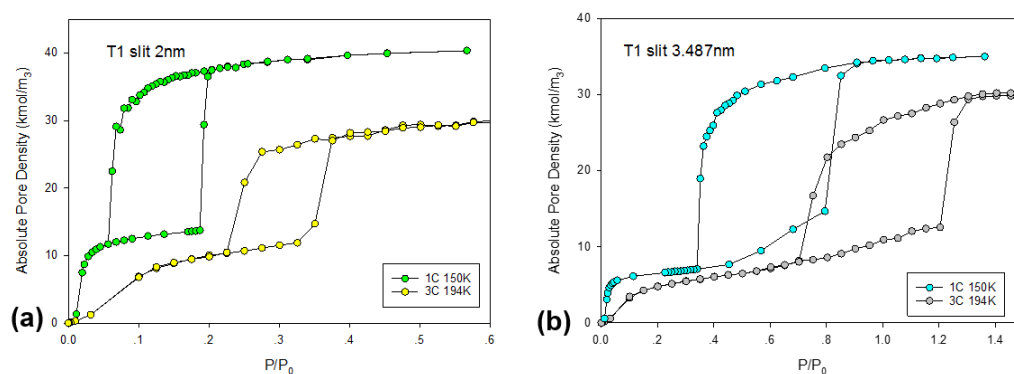


**Figure 4.6.** Comparison of isotherms at temperature T1 for 1C-LJ and 3C-LJ models in slit pores with the pore size of (a) 2 nm and (b) 3.5 nm.

#### At T2 - Above triple and below critical point

Figure 4.7 illustrates the adsorption isotherms of both models at T2 in the slit pores of width 2nm and 3.5nm. Compare with results at T1, some features remain the same, including (1) 1C-LJ model predicts higher saturated density than 3C-LJ model; (2) the monolayers are built at lower relative pressure with 1C-LJ model, although the discrepancy between the two models is reduced with increased temperature. Other major impacts caused by the temperature rise are:

- The hysteresis vanished in the 2nm pore for both models, instead a reflection point and vertical reversible transition was observed for 1C-LJ model, and a more gradual building up process with 3C-LJ model.
- In the 3.5nm pore, the hysteresis of 1C-LJ model becomes much smaller, the 3C-LJ model fills the pore, instead of only partially wet the surfaces due to increased thermal mobility by increasing the temperature from T1 to T2.

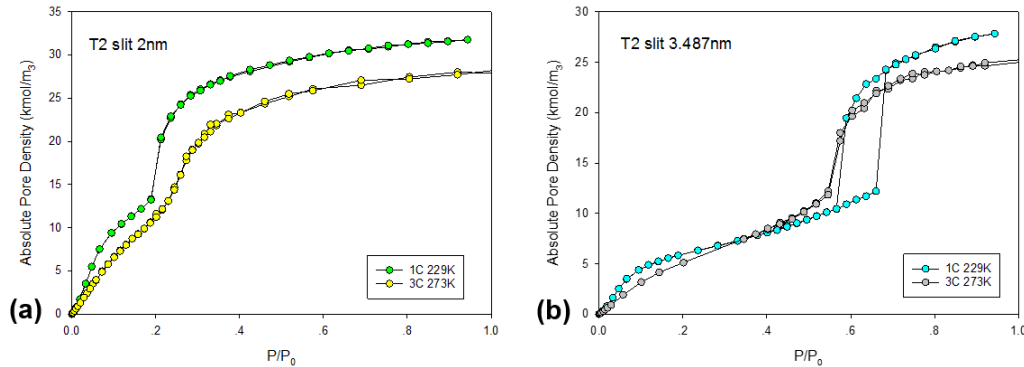


**Figure 4.7.** Comparison of adsorption isotherms at temperature T2 for 1C-LJ and 3C-LJ models in slit pores with the pore size of (a) 2 nm and (b) 3.5 nm.

### 4.3.4 Adsorption in wedge pores

The adsorption isotherm in the wedge pore at different temperatures are presented in Figure 4.8. The wedge pore has an axial length of 8.5 nm, widths of 2 nm (small end) and 3.5 nm (large end), and tilt angle  $\alpha = 5^\circ$ . Some of the differences between the two models that observed in the slit pores are also captured with the wedge pore, i.e. (1) higher saturated pore density predicted by the 1C-LJ model at T1 and T2, (2) the monolayer formation is facilitated with 1C-LJ model at the same equivalent temperature, due to its stronger interaction with solid, and (3) the discrepancy between two models diminishes with temperature. Furthermore, the type H2b hysteresis (IUPAC classification) and step-wise desorption that has been observed as the major features for adsorption in wedge pores, was reproduced with the 1C-LJ model at T1 but not the 3C-LJ model. The latter instead predicts a smaller H1 type of hysteresis (see Figure 4.8(b)). The reason is due to the packing effects of CO<sub>2</sub> molecules, as it has been known that the alternating commensurate and incommensurate are accounted for the step-wise desorption behavior, which was observed with 1C-LJ model at T1 (see Figure 4.9(a)) consistent with other noble gases [9]-[11], but not the 3C-LJ model. This indicates the impacts of the quadrupole and molecular shape on the packing. The alternative packing of the 1C-LJ model no longer exists with temperature increased. As seen in Figure 4.9(b), the configuration clearly appears to be disordered.



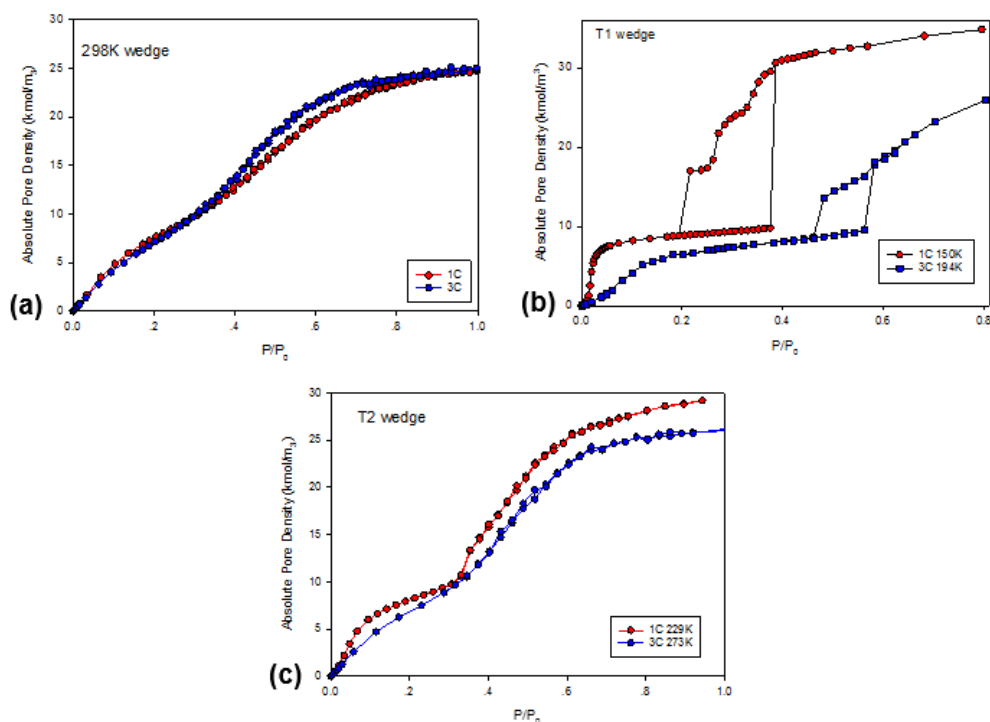


**Figure 4.8.** Comparison of adsorption isotherms for 1C-LJ and 3C-LJ models in the wedge pore at various temperatures: (a) 298 K, (b) T1, (c) T2. The pores are 8.5 nm in axial length.

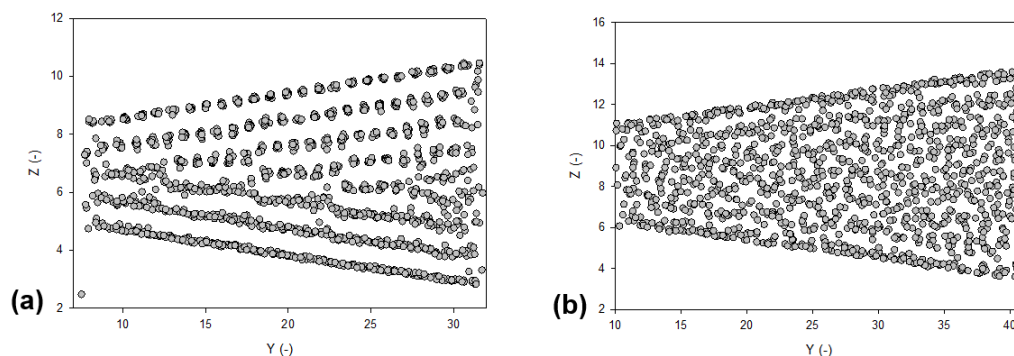


**Figure 4.9.** Snapshots of CO<sub>2</sub> molecules in the reference wedge pore at saturation vapor pressures for (a) 1C-LJ model (at temperatures below triple point) and (b) 1C-LJ (at temperatures above triple point).

### Effects of temperature

The possible disputation about the way of defining the equivalent temperature was aware of, although intention was to evaluate the two models at

the same thermodynamic status. To eliminate possible discrepancies caused by this definition, this section systematically illustrates the evolution of the performances of the two models in the wedge pore as a function of temperature. Figure 4.10 shows the adsorption isotherms for temperatures ranged between 150K (below the triple point) and 273K (above the triple point). The following observations can be made.

1. Figure 4.10(a) depicts Type H2(b) hysteresis (of IUPAC), which is then transformed into Type H1 for temperatures increased from 150 to 173K. The closure point of the hysteresis loop shifts to a higher relative pressure and smaller size until it is completely vanished at 216.6K, instead a sharp transition is observed. In the desorption boundary of the hysteresis, the number of steps remains unchanged between 150 and 160K. Once the temperature reaches 173K, which is above the triple point, the last two steps are gradually smoothed out. This implies that a critical temperature of this step-wise behavior is between 172 and 174K for the reference wedge pore.
2. Figure 4.10(b) clearly shows with the 3C-LJ model, when temperature is no higher than 170K, the fluid only can partially wet the surface. At 194K, Type H1 in IUPAC is observed, and 216 K is the hysteresis critical temperature for the studied wedge pore, i.e. above which the isotherm becomes reversible. However, the pore critical temperature should be above 216 K, where exhibits no sharp jump in adsorption isotherm, which implies no occurrence of condensation.
3. In the monolayer region, the 1C-LJ model describes oppositely as the 3C-LJ model for the trend of the uptake rate/pressure as a function of temperature. The uptake of 1C-LJ CO<sub>2</sub> and completion of the monolayer shifts to higher reduced pressure with temperature, and this is consistent with experimental data (Bottani et al. 1994; Dantas et al. 2019; Terlain and Larher 1983). Same trend can be observed on isotherm results using a uniform slit mesopore and graphitic surface with 1C-LJ model, while 3C-LJ model consistently describes in the opposite way.

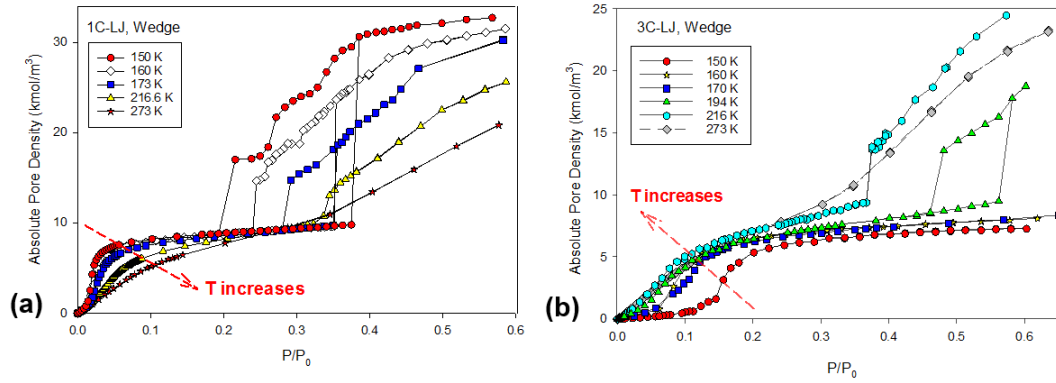


**Figure 4.10.** Isotherms of  $\text{CO}_2$  adsorption corresponding to the reduced pressure for the reference wedge pore at various temperatures using (a) 1C-LJ model (triple point = 172K) and (b) 3C-LJ model (triple point = 216K).

## 4.4 Summary

This chapter has presented a systematic simulation of  $\text{CO}_2$  bulk phase co-existence properties and its adsorption on graphitic surfaces, and in slit and wedge pores by evaluating the performance of two  $\text{CO}_2$  potential models (i.e. 1C-LJ and 3C-LJ). An equivalent temperature was introduced for comparing 1C-LJ and 3C-LJ models at the same thermodynamic condition. Simulations with 3C-LJ model accounting for the presence of a quadrupole moment have better agreement for the vapor-liquid and vapor-solid equilibria, and adsorption, especially at the temperature below triple point and at high pressure region. On the other hand, the 1C-LJ model has better agreement with the experimental data at low pressure region. The difference between simulation results and experimental data for both models is negligible at temperature above the triple point.

Because of the electrostatic interactions, 3C-LJ model has the characteristics of non-wetting and wetting and is dependent on the difference between the isosteric heat at zero loading for adsorption and the heat of evaporation of the bulk fluid, as well as the strength of the intermolecular interactions of the fluids. The quadrupolar  $\text{CO}_2$  molecules lie parallel to the graphite surface to maximize their interactions. As the temperature increases, 1C-LJ model tends to be hydrophilic on graphitic surface while the 3C-LJ model tends to be hydrophobic on graphitic surface.

Simulations for 1C-LJ model at the temperature below the triple point show occurrence of step-wised hysteresis in slit pore and wedge-shaped pore.

This occurrence is well-aligned with other simple gases. It is also evident that the consideration of shape and quadrupole of CO<sub>2</sub> are significant in the correct description of adsorption isotherm and packing density in slit and wedge pores, especially at temperatures below the triple point.

In the monolayer region, the 3C-LJ model describes in the opposite trend as compared to the 1C-LJ model. Same observations have been found on isotherms of the slit pore and graphitic surface. As the temperature increases, the uptake of 1C-LJ model and completion of the monolayer shifts to higher reduced pressure. These observations are consistent with experimental data (Bottani et al. 1994; Dantas et al. 2019; Terlain and Larher 1983).

# Chapter 5

## Adsorptive Separation of CO<sub>2</sub>

### 5.1 Introduction

Gas adsorption by AC is one of the common approaches applied in industries for separation and purification purposes, e.g., air purification and hydrocarbon processing as well as carbon capture and storage. Understanding the preferential adsorption of the adsorbates in gas mixture becomes crucial for improving the separation technologies. With the development of computational technology, molecular simulation is recognized as a useful tool that can be important compensation to experimental measurement. A uniform slit pore is commonly used as a pore model for representing the AC. However, the pore structure of AC is rather complex and is composed of randomly stacked crystallites. The confined spaces between the carbon stacks tend to be wedge-shaped.

In this regard, a systematic Monte Carlo simulation was conducted to study the adsorption of binary mixtures containing CO<sub>2</sub> with CH<sub>4</sub> or N<sub>2</sub> at the ambient temperatures (i.e., 273 K – 298 K) in slit and wedge-shaped pores with graphitic surfaces. The pore size distributions reported for the commercial AC Norit RB2 and R1 Extra were used as the references for constructing the pore models, i.e., deciding the pore widths for a set of uniform slit pores, the combination of which then formed the pore model of AC. The chemical potentials for mixtures as a function of temperature, pressure and molecular fractions of multicomponent were obtained with NPT schemes. The adsorption isotherms of CO<sub>2</sub>, CH<sub>4</sub>, N<sub>2</sub> and their mixtures in single slit pores are obtained by GCMC, then used to predict the adsorption isotherm of pure and binary gases in the AC, respectively. The wedge pore with equiv-

alent accessible pore volume (as the combined slit pores) was used to predict the adsorption isotherm of pure and mixture gases and then compared with the experimental data and IAST predicted data.

## 5.2 Theory and Simulation

### 5.2.1 Potential models

The corresponding molecular parameters for the selected potential model of TraPPE CO<sub>2</sub>, 1C-LJ CH<sub>4</sub> and 1C-LJ N<sub>2</sub> are listed in Table 1.1. The interaction energy between molecules  $i$  and  $j$  is given by the sum of the Lennard-Jones (LJ) and Coulomb interactions as presented in eq. (2.7). The solid-fluid interaction energy is calculated by the Bojan-Steele equation.

### 5.2.2 Simulation systems

Two simulation systems used in this chapter are a uniform slit pore and a closed-end wedge pore.

### 5.2.3 Monte Carlo simulation

#### NPT Simulation

To ensure the accuracy of output data, the chemical potentials of individual species (e.g., CO<sub>2</sub>) are verified as shown in Figure 5.1 by comparing with equation of state (EOS) as reported in Johnson et al. (1993); Lotfi et al. (1992). It is evident that the chemical potentials of individual species are correctly calculated in the NPT simulation (Tan et al. 2016).

In NPT, at least  $2 \times 10^4$  cycles were employed, 20 000 displacement moves and 10 volume change moves in each cycle, in both the equilibration and sampling stages. After displacement moves, the partial average pressure was used to decide the volume change. The initial volume and number of particles were set at 27 nm<sup>3</sup> (cubic box) and 300, respectively. All three dimensions are altered when the volume is changed. The pressure was recalculated with the virial method and derived from the relationship between the pressure and chemical potential, predetermined from simulations of the bulk phase of a constant mole fraction in the canonical ensemble. Details of the NPT scheme can be found in Sec. 2.1.3.

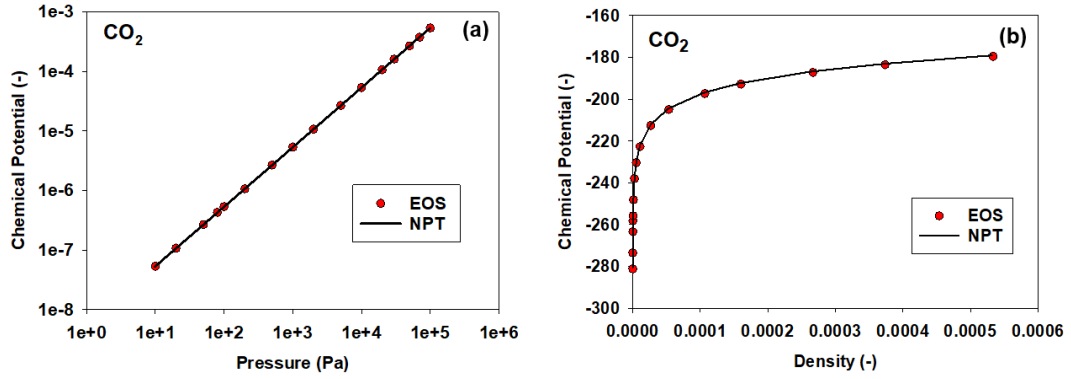


**Figure 5.1.** The chemical potential of CO<sub>2</sub> at 273K as functions of (a) pressure in log-scale; (b) density in linear scale. Circles are plotted from the EOS of Johnson et al. and the solid line is taken from NPT.

### Grand canonical Monte Carlo

As described in Sect. 2.1.1, at least  $1 \times 10^5$  cycles were employed in both equilibration and sampling stages to obtain the adsorption isotherm, the isosteric heat as a function of loading and microscopic properties, with the chemical potential obtained from the NPT as the input. Each cycle consists of 1000 displacement moves, insertion and deletion with equal probability. As a result, this generated a total of  $1 \times 10^8$  configurations.

### IAST

The pyIAST (Simon et al. 2016) was applied by firstly considering the experimental pure gas isotherms (Dreisbach et al. 1999; Goetz et al. 2006). In the pyIAST program, the Langmuir calculation model was used to fit the experimental pure gas isotherms and the results were then used to predict gas mixture isotherms for comparison purposes ((Dreisbach et al. 1999; Goetz et al. 2006).

## 5.3 Results and Discussion

### 5.3.1 Activated carbon Norit R1 Extra

Binary mixtures adsorption of CH<sub>4</sub>, N<sub>2</sub> and CO<sub>2</sub> are performed on Norit R1 Extra (R1E), which has microporous volume of 0.3511 cm<sup>3</sup>/g and BET surface of 1407.3m<sup>2</sup>/g [1]. The measurements were obtained gravimetrically

at 298K over a pressure ranging from 93kPa to 6.077 MPa. Pore size distribution of the Norit R1 Extra can be found in Dreisbach et al. (1999). The pore width reported,  $H^*$  is between 0.45-0.65, 0.7-0.78, 1.05-1.95nm. In this chapter, the pore width is calculated as follows,  $H = H^* + \text{collision diameter of carbon atom (i.e. 0.34nm)}$ . We select a combination of uniform slit pores with pore length  $L = 8.5\text{nm}$  and different pore sizes to represent the geometry structure of AC as illustrated in Figure 5.2: pore widths (1)  $H = 0.8\text{nm}$  (i.e.,  $H^* = 0.47\text{nm}$ ), (2)  $H = 1.1\text{nm}$  (i.e.,  $H^* = 0.73\text{nm}$ ) and (3)  $H = 1.5\text{nm}$  (i.e.,  $H^* = 1.18\text{nm}$ ). Those pore widths (1)-(3) are selected from the peaks of pore size distribution plot for the R1E (Nguyen and Bhatia 2004). The adsorption isotherms are reconstructed following the ratios of 0.1, 0.3 and 0.6 corresponding to pore widths (1)-(3). A closed end wedge pore model is chosen with an equivalent accessible pore volume (as the reconstructed slit pore model). The configurations of the closed end wedge pore applied in this chapter are  $L = 9.7\text{nm}$ ,  $SH = 0.35\text{nm}$ ,  $BH = 2.05\text{nm}$ , and  $\alpha = 5^\circ$ .

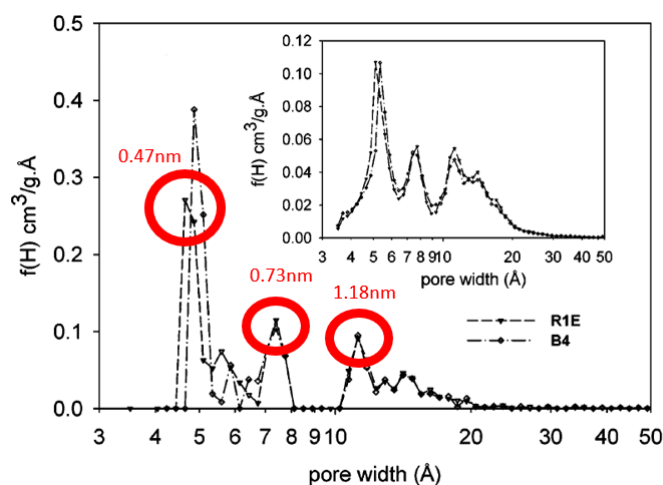


**Figure 5.2.** Pore size distribution of Norit R1 Extra and Sorbonorit B4 carbons, obtained by interpretation of argon adsorption at 87K using the current approach. The inset shows the PSD using the conventional infinite wall thickness model [Reprinted (adapted) with permission from T. X. Nguyen, S. K. Bhatia, Characterization of pore wall heterogeneity in nanoporous carbons using adsorption: the slit pore model revisited, *J. Phys. Chem B* 108 (37) (2004) 14032–14042. doi:10.1021/jp049048f. Copyright 2022 American Chemical Society].



### Pure gases adsorption

The adsorption isotherms for pure gases  $N_2$ ,  $CH_4$  and  $CO_2$  on the AC Norit R1E at  $T = 298K$  and pressures up to 6 MPa are presented in Figure 5.3 (Dreisbach et al. 1999). Type I isotherms were presented for both pure gases. At ambient temperature, the carbon solid exhibits preferential adsorption for  $CO_2$  in relation to  $CH_4$  following with  $N_2$  over the pressure range, which has a higher adsorbed density. The wedge pore well predicted the experimental data for  $N_2$ ,  $CO_2$  and  $CH_4$  at 298K as shown in Figure 5.3(b). The combination of slit pores fits experimental data well for  $CO_2$  at 298K as shown in Figure 5.3. The simulated isotherms and experimental data shows continuous pore filling mechanisms and the adsorption behavior of the  $N_2$ ,  $CH_4$  and  $CO_2$  occurs at pressures lower than the saturated pressure (Do 1998).

As shown in Figure 5.3, the adsorbed amounts of  $N_2$ ,  $CH_4$  and  $CO_2$  in wedge pore are less than that in slit pore. The wedge pore has a narrow end to a bigger end. The smaller pore end of AC leads to the stronger interaction between fluid and carbon wall. Thus, the pore size of porous carbon is one of contributing factors in pure gases and mixtures adsorption of  $N_2/CO_2/CH_4$ . Furthermore, it is evident that the adsorption isotherms of  $CO_2$  at 298K and the pressure up to 0.5MPa exhibit the initial part of the Type I isotherm, implying the micropore filling mechanism (Do 1998). On the other hand, the behaviour of  $CH_4$  and  $N_2$  isotherms is similar to that of  $CO_2$  isotherms. The adsorbed amount of  $CH_4$  and  $N_2$  are less than  $CO_2$  due to weaker interaction with the AC.  $CH_4$  and  $N_2$  molecules do not contain any quadrupole moment and electrostatic charge as compared to  $CO_2$  molecules (Do and Do 2006a). In this regard,  $CH_4$  and  $N_2$  molecules have weaker intermolecular force on carbon surface in comparison to the intermolecular force between carbon surface and  $CO_2$  molecule, contributing to different adsorption behaviours (Choi et al. 2003) as shown in Figure 5.3. As shown in Figures 5.4 and 5.5, the potential profiles of  $CH_4/N_2/CO_2$  with Bojan-Steel surface and between two fluid molecules also explain that  $CO_2$  has stronger solid-fluid and fluid-fluid interactions than  $CH_4$  and  $N_2$ .

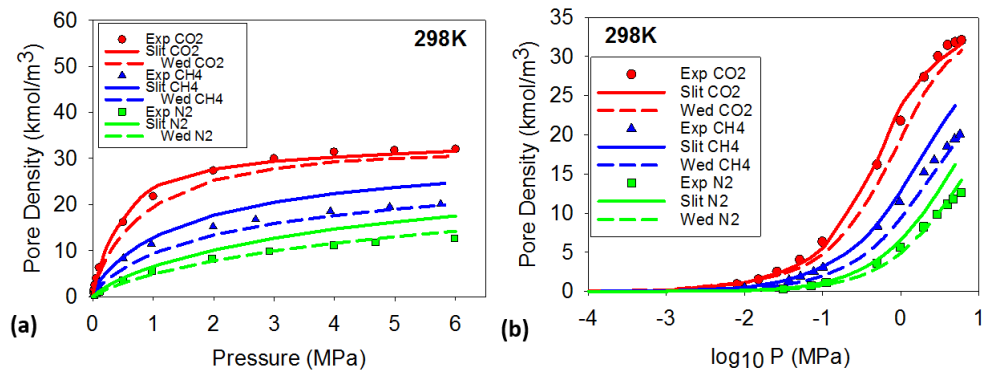


**Figure 5.3.** Experimental data of pure N<sub>2</sub>, CH<sub>4</sub> and CO<sub>2</sub> on AC Norit R1E at  $T = 298\text{K}$  (Dreisbach et al. 1999). Prediction of data with the adsorption isotherms in a slit and wedge pore: (a) absolute pressure and (b) absolute pressure in log scale.

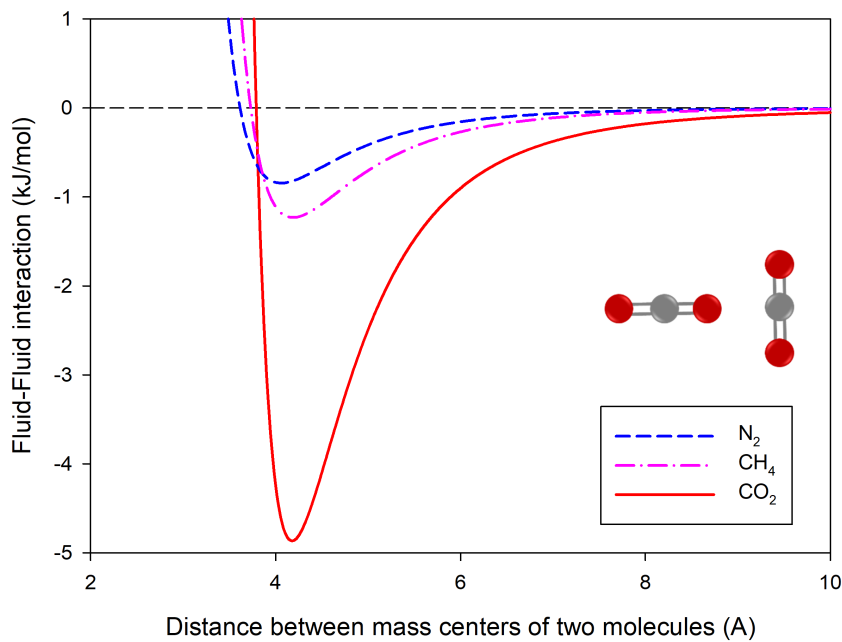


**Figure 5.4.** The profile of pairwise interaction between two fluid molecules. For CO<sub>2</sub>, the axis of the two molecules lies in the same plane, and perpendicular to each other, the distance between two carbon atoms varied.

### CO<sub>2</sub>/CH<sub>4</sub> adsorption

For the binary adsorption, the pressures are ranged from 93 kPa to 6.077 MPa. The experimental composition of the gas mixture is tabulated in Ta-

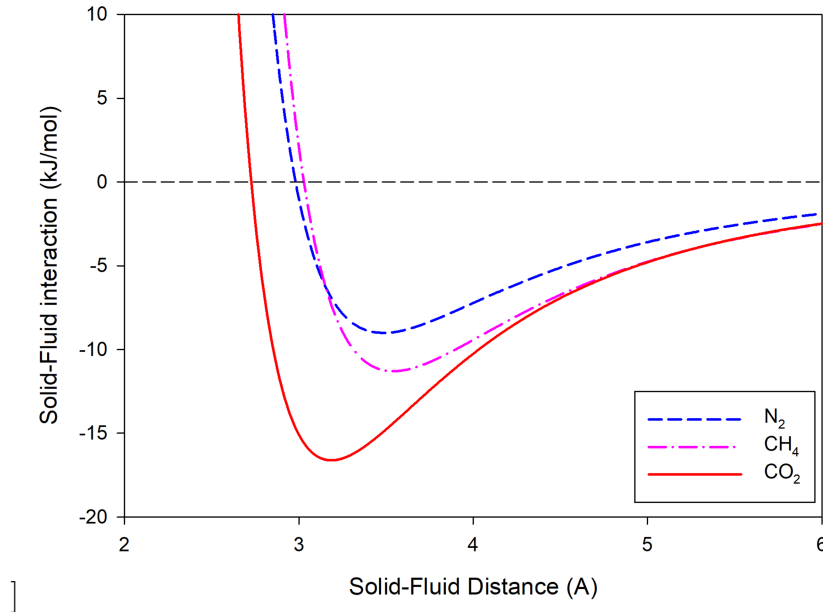


**Figure 5.5.** The profile of the selected fluid molecular interact with the graphite surface, simulated with Bojan potential. For  $\text{CO}_2$ , the axis of the molecule lies parallel to the graphite surface, and the distance between the two changes by shifting the whole molecule above the surface.

ble 5.1 and the adsorbed amount of each gas experimentally measured on the AC reported for  $T = 298\text{K}$  are referred to Dreisbach et al. (1999).

**Table 5.1** Experimental composition of the gas mixture containing  $\text{CO}_2$  and  $\text{CH}_4$  (Dreisbach et al. 1999).

	$\text{CO}_2$	$\text{CH}_4$
a)	6%	94%
b)	48%	52%
c)	79%	21%

Adsorbed amount as a function of the gaseous composition at  $T = 298\text{K}$ , and pressures are presented in Figure 5.6. The experimental data (symbols) at 298K exhibit the adsorbed quantities. The results were then compared between slit pore, wedge pore and IAST models (solid lines).

Similar discussion to AC Norit RB2 can be made. The total adsorbed amount increased against  $\text{CO}_2$  composition and simultaneously, the amount of  $\text{CH}_4$  adsorbed decreased, implying the competition for adsorption sites and preferential adsorption of  $\text{CO}_2$  over  $\text{CH}_4$ . Because of its higher boil-

ing point than CH<sub>4</sub>, CO<sub>2</sub> is more likely to behave as a condensable steam while CH<sub>4</sub> as a supercritical gas (Kirk and Othmer 2004). This less volatility of CO<sub>2</sub> increased its adsorption preference on AC than CH<sub>4</sub>. Furthermore, CO<sub>2</sub> exhibits a higher polarizability, which enhance attractive forces with the surface and a quadrupole moment (Do and Do 2006a), leading to stronger interactions with the solid surface than CH<sub>4</sub>. Thus, we can see from Figure 5.6 that for binary isotherms, CO<sub>2</sub> has higher adsorbed amounts than CH<sub>4</sub>. It is worth to note that the total amount of adsorbates increases with the concentration of CO<sub>2</sub> in the bulk mixture (Dreisbach et al. 1999).

From the analysis of Figure 5.6, the slit pore model well-predicted experimental data comparable with IAST predictions. The wedge pore model showed better fitted results with experimental data for CH<sub>4</sub> isotherm and comparable with IAST predictions. The slit pore model showed better results in predicting total (CO<sub>2</sub> + CH<sub>4</sub>) adsorbed amounts for experimental data in comparison with the wedge pore. However, the overall performance of IAST is good, especially well fitted the adsorbed amount at 298K (see Figures 5.6(c)(f)(i)). On the other hand, the wedge pore model under predicted in overall and well-fitted the experimental data for CH<sub>4</sub> (see Figure 5.6(e)(h)). This might be explained by only using a single wedge pore and the geometry structure of AC Norit R1E could be even complex. The isotherms of CH<sub>4</sub> agrees well with experimental data of CH<sub>4</sub>. At high pressure, the interactions in the adsorbed phase become dominant and decrease the applicability of the IAST model (Buss 1995).

### CO<sub>2</sub>/N<sub>2</sub> adsorption

The experimental composition of the gas mixture is tabulated in Table 5.2 and the adsorbed amount of each gas experimentally measured on the AC reported for T = 298K are referred to Dreisbach et al. (1999).

**Table 5.2** Experimental composition of the gas mixture containing CO<sub>2</sub> and N<sub>2</sub> (Dreisbach et al. 1999).

	CO <sub>2</sub>	N <sub>2</sub>
a)	21%	79%
b)	47%	53%
c)	85%	15%

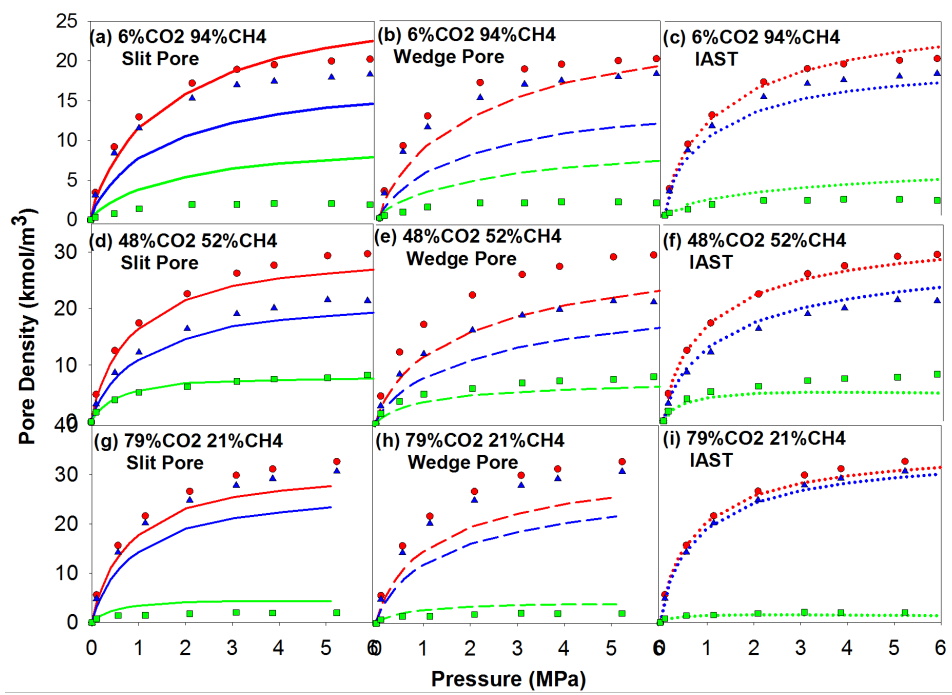


**Figure 5.6.** Adsorption isotherms of  $\text{CO}_2/\text{CH}_4$  mixture at  $T = 298\text{K}$  in a slit pore, wedge pore and predicted values from IAST for the pressures ranging from 93kPa to 6.077MPa, and the adsorbed amounts of  $\text{CO}_2$  and  $\text{CH}_4$  from their mixture [symbols: experimental data (Dreisbach et al. 1999), solid lines: theoretical model, red: total adsorbed amount of  $\text{CO}_2$  and  $\text{CH}_4$ , blue: adsorbed amount of  $\text{CO}_2$ , green: adsorbed amount of  $\text{CH}_4$ ].

Adsorbed amount as a function of the gaseous composition at  $T = 298\text{K}$ , and pressures are presented in Figure 5.7. The experimental data (symbols) at 298K exhibit the adsorbed quantities. The results were then compared between slit pore, wedge pore and IAST models (solid lines).

The total adsorbed amount increased against  $\text{CO}_2$  composition and simultaneously, the amount of  $\text{N}_2$  adsorbed decreased, implying the competition for adsorption sites and preferential adsorption of  $\text{CO}_2$  over  $\text{N}_2$ . Because of its higher boiling point than  $\text{N}_2$ ,  $\text{CO}_2$  is more likely to behave as a condensable water vapour while  $\text{N}_2$  as a supercritical gas (Kirk and Othmer 2004). This less volatility of  $\text{CO}_2$  increased its adsorption preference on AC than  $\text{N}_2$ . Furthermore,  $\text{CO}_2$  exhibits a higher polarizability, which enhance attractive forces with the surface and a quadrupole moment (Harris and Yung 1995), leading to stronger interactions with the solid surface than  $\text{N}_2$ . Thus, we can see from Figure 5.7 that for binary isotherms,  $\text{CO}_2$  has higher adsorbed

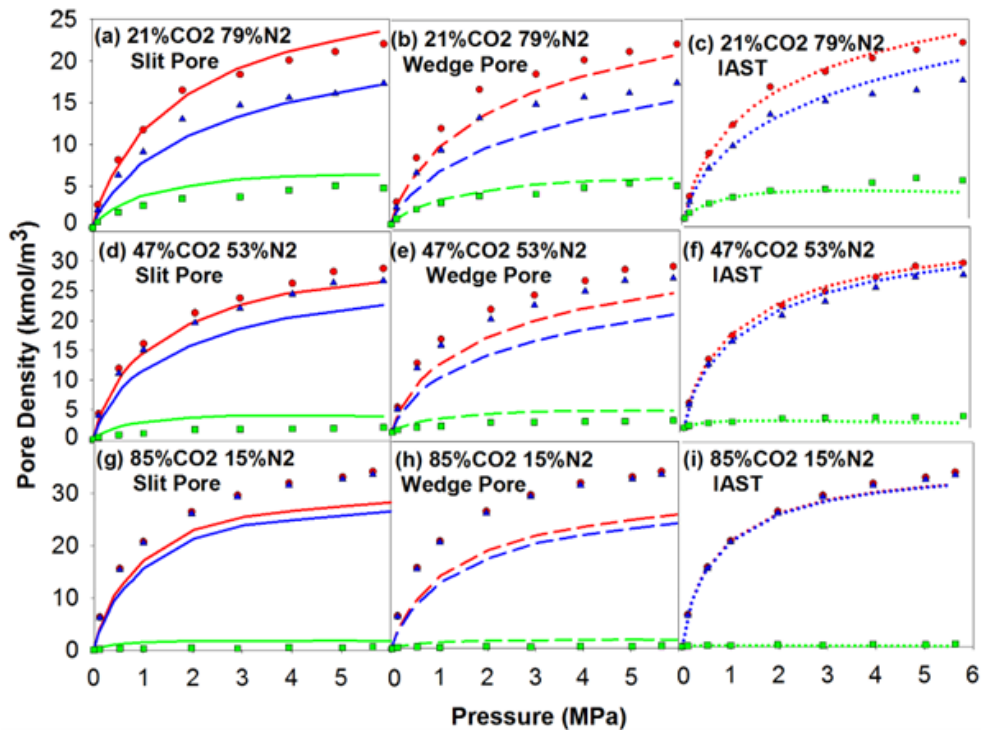


**Figure 5.7.** Adsorption isotherms of CO<sub>2</sub>/N<sub>2</sub> mixture at  $T = 298\text{K}$  in a slit pore, wedge pore and predicted values from IAST for the pressures ranging from 93kPa to 6.077MPa, and the adsorbed amounts of CO<sub>2</sub> and N<sub>2</sub> from their mixture [symbols: experimental data (Dreisbach et al. 1999), solid lines: theoretical model, red: total adsorbed amount of CO<sub>2</sub> and N<sub>2</sub>, blue: adsorbed amount of CO<sub>2</sub>, green: adsorbed amount of N<sub>2</sub>].

amounts than N<sub>2</sub>. It is worth to note that the total amount of adsorbates increases with the concentration of CO<sub>2</sub> in the bulk mixture (Dreisbach et al. 1999).

From the analysis of Figure 5.7, the slit pore model well-predicted experimental data comparable with IAST predictions. The wedge pore model showed better fitted results with experimental data especially for N<sub>2</sub>. The slit pore model showed better results in predicting total (CO<sub>2</sub> + N<sub>2</sub>) adsorbed amounts for experimental data in comparison with the wedge pore. However, the overall performance of IAST is good, especially well fitted the adsorbed amount at 298K (see Figure 5.7(c)(f)(i)). On the other hand, the wedge pore model under predicted in overall and well-fitted the experimental data for N<sub>2</sub> (see Figure 5.7(b)(e)(h)). This might be explained by only using a single wedge pore and the geometry structure of AC Norit R1E could be

even complex. The isotherms of  $N_2$  agrees well with experimental data.

### Selectivity of $CO_2$ over $CH_4$ or $N_2$

The selectivity eq. (2.40) of  $CO_2$  over  $CH_4$  or  $N_2$  at  $T = 298K$  is calculated as shown in Figure 5.8. the selectivity for  $CO_2$  over  $N_2$  is higher than over  $CH_4$ . This indicates that  $N_2$  adsorbs less strongly than  $CH_4$ .  $CO_2$  molecule has a smaller diameter around axis than  $N_2$ . Hence, the  $CO_2$  molecule has a strong attraction in pores. A smaller pore hinders the rotational of  $CO_2$  molecules. However, it does not hinder the movement of  $N_2$  molecules to the same extent as  $N_2$  molecule is shorter. This can be due to an entropic effect. A wider pore allows  $CO_2$  molecule to move freely and therefore the selectivity increases, especially in wedge pore. The selectivity increases along with the increasing of partial loading of  $CO_2$ , pressures and mole fraction of  $CO_2$  in gas mixture. A high selectivity can be clearly seen at a high partial loading of  $CO_2$  on the carbon. The  $CH_4$  gas has a low selectivity in gas mixture containing  $CO_2$ . The reason is due to its weaker intermolecular force on carbon surface in comparison to the intermolecular force between carbon surface and  $CO_2$  molecule. The selectivity has also been predicted by calculation with IAST and with molecular simulation in slit and wedge pore. Generally, the slit and wedge pore can achieve satisfactory predictions of the selectivity of gas mixtures for the conditions where interactions between the adsorbed molecules are critical. IAST fails to predict the selectivity as it does not consider the interactions between the adsorbed molecules. At high surface coverage especially for high pressure region ( $>1$  MPa), the adsorbed phase becomes dominant and this significantly reduce the applicability of IAST.

### 5.3.2 Activated carbon Norit RB2

Single and multicomponent adsorption of  $CH_4$  and  $CO_2$  are performed on the commercial AC Norit RB2. The experimental procedure and data are referred to Goetz et al. (2006). The Norit RB2 has microporous volume of  $0.43 \text{ cm}^3/\text{g}$  (Goetz et al. 2006). The pressure range were 0–1 MPa for mixtures adsorption. The measurements were obtained volumetrically at 273K and 298K over a pressure ranging from 0 to 1 MPa. Pore size distribution of the Norit RB2 can be found in Nguyen and Bhatia (2004). The pore width reported of Norit RB2,  $H^*$  is between 0.37-0.78, 1.05-1.95nm. In this work,

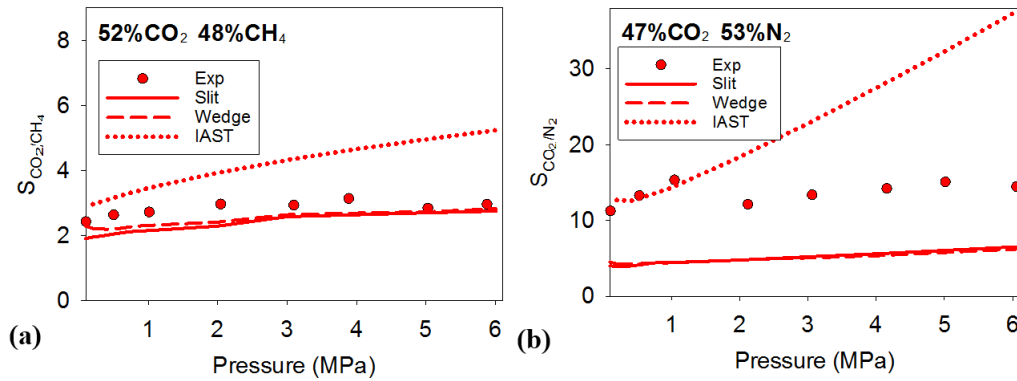


**Figure 5.8.** Selectivity of CO<sub>2</sub> over CH<sub>4</sub> or N<sub>2</sub> at  $T = 298\text{K}$  on AC Norit R1E at approximately 50% CO<sub>2</sub> with experimental data (Dreisbach et al. 1999) (symbols).

the pore width is calculated as follows,  $H = H^* + \text{collision diameter of carbon atom}$  (i.e. 0.34nm). We consider a combination of uniform slit pores with pore length  $L = 8.5\text{nm}$  and different pore sizes to represent the geometry structure of AC as illustrated in Figure 5.9: (1)  $H = 0.8\text{ nm}$  (i.e.,  $H^* = 0.47\text{ nm}$ ), (2)  $H = 1.1\text{ nm}$  (i.e.,  $H^* = 0.75\text{ nm}$ ), (3)  $H = 1.45\text{ nm}$  (i.e.,  $H^* = 1.1\text{ nm}$ ) and (4)  $H = 100\text{nm}$  (i.e., surface adsorption). Those pore widths (1)-(3) are selected from the peaks of pore size distribution plot for the RB2 (Nguyen and Bhatia 2004). The adsorption isotherms are reconstructed following the ratios of 0.15, 0.21, 0.29, 0.35 corresponding to pore widths (1)-(4). A closed end wedge pore model is chosen with an equivalent accessible pore volume (as the reconstructed slit pore model following same ratios corresponding to pore widths (1)-(3)). The configurations of the wedge pore applied in this work are  $L = 7.5\text{ nm}$ ,  $SH = 0.35\text{ nm}$ ,  $BH = 1.66\text{ nm}$ , and  $\alpha = 5^\circ$ .



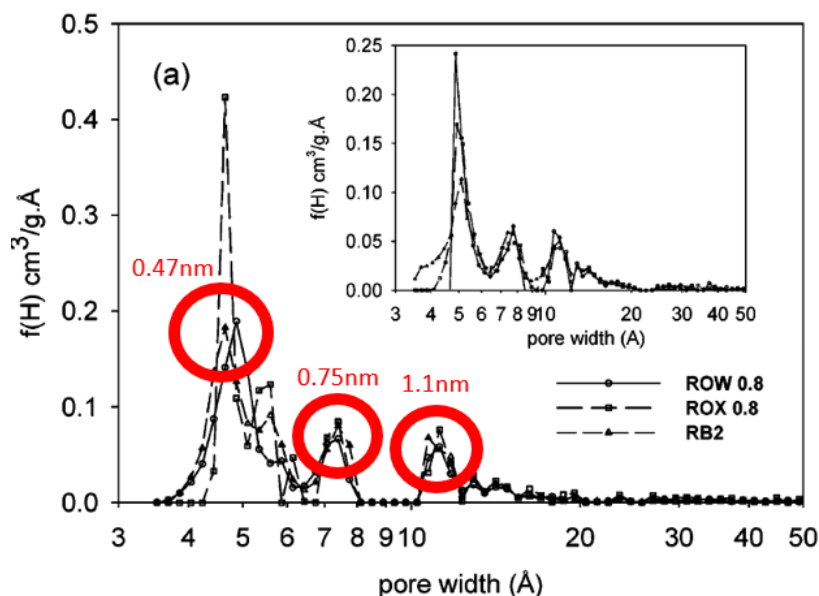


**Figure 5.9.** Pore size distribution of Norit RB2, ROW 0.8 and ROX 0.8 carbons, obtained by interpretation of argon adsorption at 87K using the current approach. The inset shows the PSD using the conventional infinite wall thickness model [Reprinted (adapted) with permission from T. X. Nguyen, S. K. Bhatia, Characterization of pore wall heterogeneity in nanoporous carbons using adsorption: the slit pore model revisited, *J. Phys. Chem B* 108 (37) (2004) 14032–14042. doi:10.1021/jp049048f. Copyright 2022 American Chemical Society].

### Pure gases adsorption

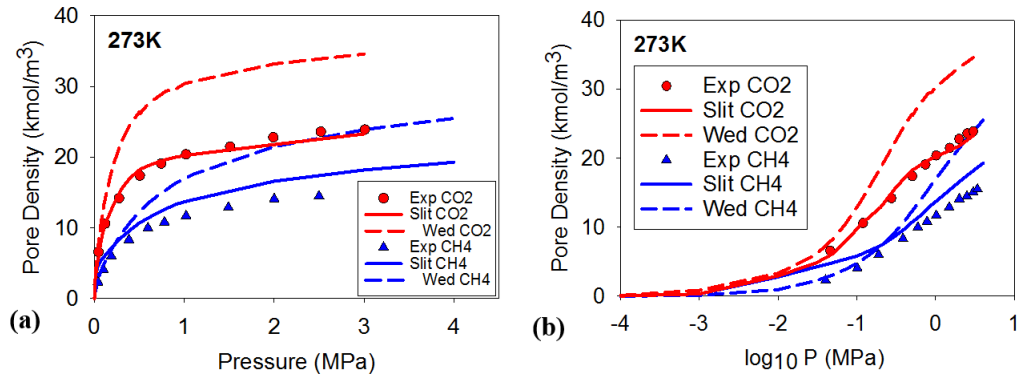
The adsorption isotherms for pure gases  $\text{CH}_4$  and  $\text{CO}_2$  on the AC Norit RB2 at the temperatures of 273 and 298K and pressure up to 3.5 MPa are presented in Figures 5.10 and 5.11, respectively (Goetz et al. 2006). According to the International Union of Pure Applied Chemistry (IUPAC) classification, Type I isotherms were presented for both pure gases, particularly in microporous materials. At ambient temperature, the AC exhibits preferential adsorption for  $\text{CO}_2$ , which has a higher adsorbed density compared to  $\text{CH}_4$  over the pressure range. The wedge pore well predicted the low-pressure region of the experimental data for both  $\text{CO}_2$  and  $\text{CH}_4$  at 273 and 298K as shown in Figures 5.10(b) and 5.11(b). The combination of slit pores fits experimental data well for  $\text{CO}_2$  at both 273 and 298K as shown in Figures 5.10(b) and 5.11(b). The simulated isotherms and experimental data

exhibit continuous pore filling mechanisms (Do 1998), which are a typical isotherm observed in microporous adsorbents. However, the phase transition at temperatures of 273 and 298K is well developed without any dramatic change. The adsorption behavior of the CH<sub>4</sub> and CO<sub>2</sub> occurs at pressures lower than the saturated pressure.

As shown in Figures 5.10(a) and 5.11(a), the adsorbed amounts of CH<sub>4</sub> and CO<sub>2</sub> in wedge pore are greater than that in slit pore. The wedge pore has a narrow end to a bigger end. The smaller pore end of AC leads to the stronger interaction between fluid and carbon wall. Thus, the pore size of porous carbon is one of contributing factors in pure gases and mixtures adsorption of CO<sub>2</sub>/CH<sub>4</sub>. Furthermore, it is evident that the adsorption isotherms of CO<sub>2</sub> at 273 and 298K and the pressure up to 0.5MPa exhibit the initial part of the Type I isotherm, implying the micropore filling mechanism (Do 1998). Apparently, the adsorbed amount at 273K is higher than that at 298K, indicating the characteristic of physical adsorption with the release of heat. The adsorbates thus require greater energy to evaporate (Do 1998; Kirk and Othmer 2004). On the other hand, the behaviour of CH<sub>4</sub> isotherms is similar to that of CO<sub>2</sub> isotherms. The adsorbed amount of CH<sub>4</sub> is less than CO<sub>2</sub> due to weaker interaction with the AC. CH<sub>4</sub> molecules do not contain any quadrupole moment and electrostatic charge as compared to CO<sub>2</sub> molecules (Do and Do 2006a). As shown in Figures 5.4 and 5.5, the potential profiles of CH<sub>4</sub>/CO<sub>2</sub> with Bojan-Steel surface and between two fluid molecules also explain that CO<sub>2</sub> has stronger solid-fluid and fluid-fluid interactions than CH<sub>4</sub>.

### CO<sub>2</sub>/CH<sub>4</sub> adsorption

For the binary adsorption, the pressures are ranged from 0.1 to 1 MPa. The experimental composition of the gas mixture and the adsorbed amount of each gas experimentally measured on the AC reported for T = 273 and 298K are referred to Goetz et al. (2006). Adsorbed amount as a function of the gaseous composition at T = 273 and 298K, and pressures of 0.1, 0.5 and 1 MPa are presented in Figures 5.12 and 5.13, respectively. The experimental data (in symbols) at 273 and 298K exhibit the adsorbed quantities between the two points with respect to pure gas adsorption of CH<sub>4</sub> (yCO<sub>2</sub> =0) and CO<sub>2</sub> (yCO<sub>2</sub>=1). The results were then compared with slit pore, wedge pore and IAST models (in solid lines).



**Figure 5.10.** Experimental isotherms of the pure gases  $\text{CO}_2$  and  $\text{CH}_4$  on AC Norit RB2 at  $T = 273\text{K}$  (Goetz et al. 2006). Adsorption isotherms in a slit and wedge pore: (a) absolute pressure and (b) absolute pressure in log scale.

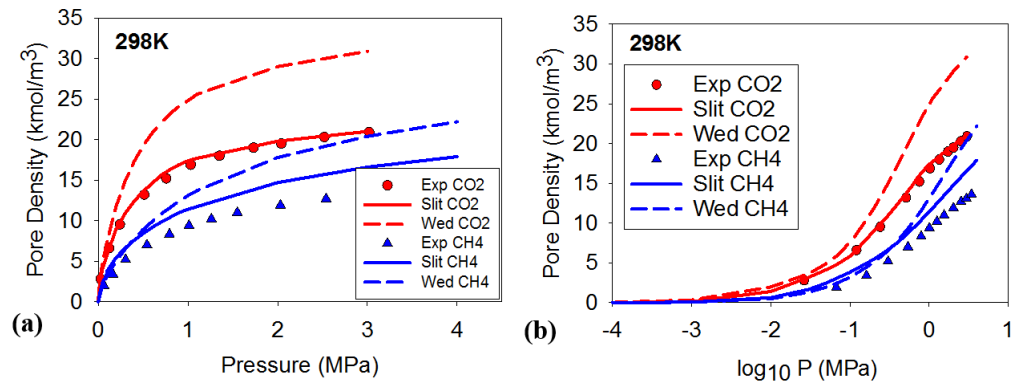


**Figure 5.11.** Experimental isotherms of the pure gases  $\text{CO}_2$  and  $\text{CH}_4$  on AC Norit RB2 at  $T = 298\text{K}$  (Goetz et al. 2006). Adsorption isotherms in a slit and wedge pore: (a) absolute pressure and (b) absolute pressure in log scale.

The total adsorbed amount increased against  $\text{CO}_2$  composition and simultaneously, the amount of  $\text{CH}_4$  adsorbed decreased, implying the competition for adsorption sites and preferential adsorption of  $\text{CO}_2$  over  $\text{CH}_4$ . Because of its higher boiling point than  $\text{CH}_4$ ,  $\text{CO}_2$  is more likely to behave as a condensable steam while  $\text{CH}_4$  as a supercritical gas (Choi et al. 2003). This less volatility of  $\text{CO}_2$  increased its adsorption preference on AC than  $\text{CH}_4$ . Furthermore,  $\text{CO}_2$  exhibits a higher polarizability, which enhances attractive forces with the surface and a quadrupole moment, leading to stronger interactions with the solid surface than  $\text{CH}_4$  (Do and Do 2006a).

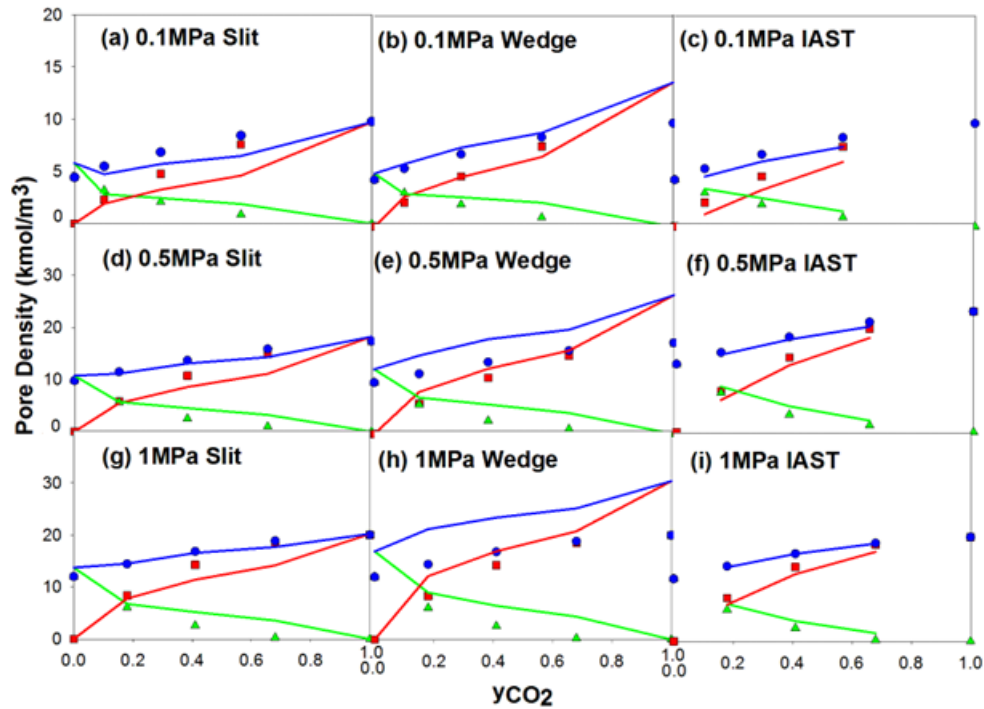


**Figure 5.12.** Adsorption isotherms of CO<sub>2</sub>/CH<sub>4</sub> mixture at  $T = 273\text{K}$  in a slit pore, wedge pore and predicted values from IAST for the pressures of 0.1, 0.5 and 1MPa, and the adsorbed amounts of CO<sub>2</sub> and CH<sub>4</sub> from their mixture [blue: total adsorbed amount of CO<sub>2</sub> and CH<sub>4</sub>, red: adsorbed amount of CO<sub>2</sub>, green: adsorbed amount of CH<sub>4</sub>].

Thus, we can see from Figures 5.12 and 5.13 that at the concentrations of  $y_{\text{CO}_2} > 20\%$  for binary isotherms, CO<sub>2</sub> has higher adsorbed amounts than CH<sub>4</sub>. It is worth to note that the total amount of adsorbates increases with the concentration of CO<sub>2</sub> in the bulk mixture (Buss 1995; Goetz et al. 2006). In comparison between both temperatures, the adsorbed amount at 273K is larger than that at 298K due to the fact of exothermic process as discussed in previous section.

From the analysis of Figures 5.12 and 5.13, the slit pore model well-predicted experimental data comparable with IAST predictions. The wedge pore model showed better fitted results with experimental data at low pressure (0.1MPa) and comparable with IAST predictions. IAST failed to fit the experimental data at low pressure (0.1 MPa) and performed well in fitting the experimental data at high pressure ( $\leq 0.5$  MPa). The slit pore model underestimated the isotherms at low pressure (0.1MPa) and better predicted total

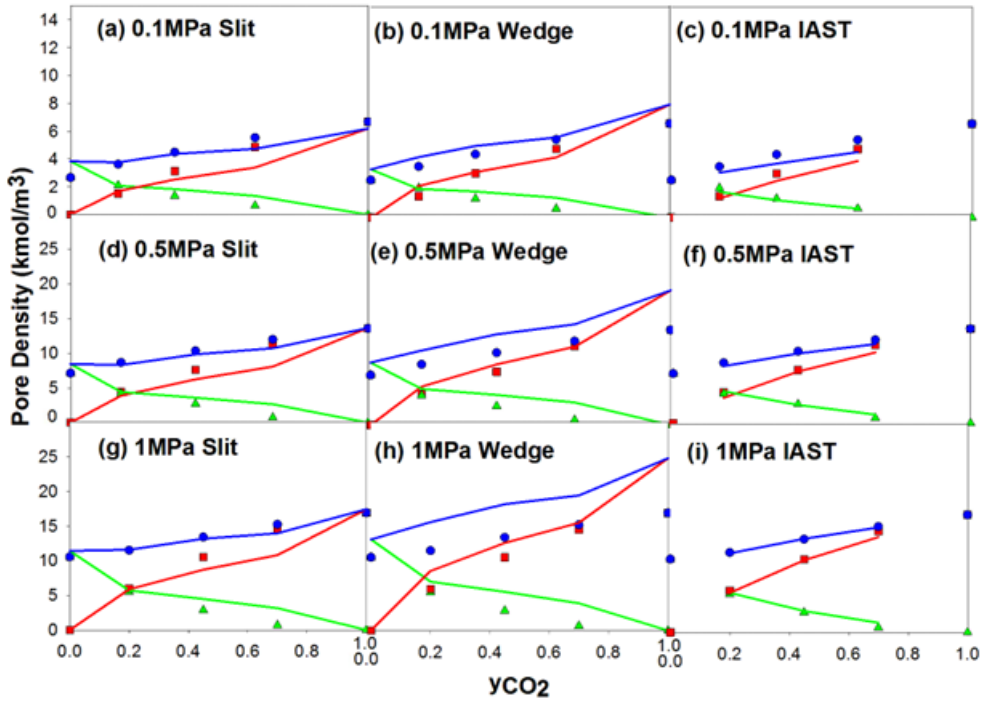


**Figure 5.13.** Adsorption isotherms of  $\text{CO}_2/\text{CH}_4$  mixture at  $T = 298\text{K}$  in a slit pore, wedge pore and predicted values from IAST for the pressures of 0.1, 0.5 and 1MPa, and the adsorbed amounts of  $\text{CO}_2$  and  $\text{CH}_4$  from their mixture [blue: total adsorbed amount of  $\text{CO}_2$  and  $\text{CH}_4$ , red: adsorbed amount of  $\text{CO}_2$ , green: adsorbed amount of  $\text{CH}_4$ ].

adsorbed amounts at high pressures (0.5 and 1MPa). The slit pore model showed better results in predicting total ( $\text{CO}_2 + \text{CH}_4$ ) adsorbed amounts for experimental data in comparison with the IAST predictions and the wedge pore. However, the overall performance of IAST is good, especially well fitted the adsorbed amount of  $\text{CH}_4$  at 298K (see Figures 5.13(c)(f)(i)). On the other hand, the wedge pore model presented reasonable predictions in overall (especially for adsorbed amount of  $\text{CO}_2$  at both temperatures (see Figures 5.12(e)(f))). This might be explained by using the real molecular shape of  $\text{CO}_2$  and this is better fit quality to the  $\text{CO}_2$  adsorption data. The spherical shape of  $\text{CH}_4$  considered in this work could be the contributing factor for the less accurate adsorption data of  $\text{CH}_4$ . At low pressure (0.1MPa), the surface coverage is higher in a  $\text{CO}_2/\text{CH}_4$  system. The interactions in the adsorbed phase become dominant and decrease the applicability of the IAST model Buss (1995). At high pressure, the surface is filled with adsorbate and

therefore, the IAST model presented the better fits at higher pressures (0.5 and 1.0 MPa) in Figure 5.12. Same discussion applies for the CO<sub>2</sub>/CH<sub>4</sub> adsorption at 298k as presented in Figure 5.13.

### Selectivity of CO<sub>2</sub> over CH<sub>4</sub>

An interesting remark is that an increase of temperature results in a decrease of selectivity. However, the selectivity increases along with the increase of partial loading of CO<sub>2</sub>, pressures and mole fraction of CO<sub>2</sub> in the gas mixture. A high selectivity can be clearly seen at a high partial loading of CO<sub>2</sub> on the carbon. The CH<sub>4</sub> gas has a low selectivity in the gas mixture containing CO<sub>2</sub>. The reason is due to its weaker intermolecular force on carbon surface compared to the intermolecular force between carbon surface and CO<sub>2</sub> molecule. Calculation with IAST and molecular simulation in slit and wedge pore has also predicted the selectivity. As shown in Figure 5.14, the calculated results and the experimental data at  $T = 273$  and 298K, and pressure up to 1 MPa. Generally, the slit and wedge pore can achieve satisfactory predictions of the selectivity of gas mixtures for the conditions where interactions between the adsorbed molecules are essential. IAST fails to predict the selectivity as it does not consider the interactions between the adsorbed molecules.

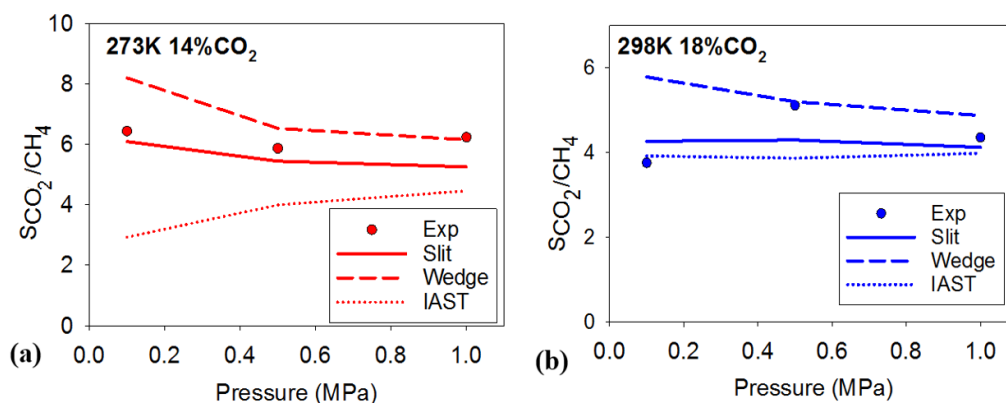


**Figure 5.14.** Selectivity of CO<sub>2</sub> over CH<sub>4</sub> at  $T =$  (a) 273K and (b) 298K on AC Norit RB2 at approximately 20% CO<sub>2</sub>.

## 5.4 Summary

Adsorption isotherms of pure CO<sub>2</sub>, CH<sub>4</sub>, N<sub>2</sub> and their binary mixtures were simulated with GCMC, by considering both uniform slit pore and wedge

pore models, to mimic the real activated carbon. The simulated results were evaluated with experimental data at 273 and 298K for the selected ACs, and compared against the predictions made by the IAST method. This chapter discussed the competition for active adsorption sites and preferential adsorption for CO<sub>2</sub> over CH<sub>4</sub> or N<sub>2</sub>, due to higher affinity. The CO<sub>2</sub> exhibited higher adsorbed amounts and selectivity to AC than CH<sub>4</sub> and N<sub>2</sub>. The molecular simulation in the slit and wedge pore can predict the selectivity well. However, the IAST provided poor predictions, particularly at higher pressures and when the inter-adsorbate interaction is dominant. At high pressure ( $\geq 0.5$ MPa), the combination of the slit pore model fitted the experimental data mostly well and agrees well with the IAST. However, at low pressure ( $< 0.5$ MPa), the predictions of single and binary equilibria with a single wedge pore model showed better agreement with the experimental data and were comparable with those predicted using the IAST method, which implies the presence of dead end in ACs does impact the adsorption at low pressure region, and this cannot be captured with the uniform slit pore model. Therefore, the wedge pore model can be treated as an alternative model for representing the non-uniform pore size distribution in the AC. However, how to define the topographic properties of the AC need further exploration, as in this chapter, the wedge pore was constructed in such a way that it has the same accessible volume as the selected set of slit pores, by fixing the small end width SH, but varying the tilt angle and pore length.





# Chapter 6

## Conclusions and Recommendations

This research addresses the fundamental mechanism of CO<sub>2</sub> adsorption within AC, which plays an important role in natural gas purification. In this chapter, the main contributions and significance of Chapters 3 to 5 are summarised in Sect. 6.1. Some possible areas for future research are described in Sect. 6.2.

### 6.1 Conclusions

The objective of this research was to examine the mechanisms of CO<sub>2</sub> adsorption in the AC that are associated with its separation and removal from natural gas mixtures. Thus, the respective mechanisms were explained in Chapters 3 to 5 for facilitating the development of technology of CO<sub>2</sub> adsorption and removal in natural gas separation. Monte Carlo simulation was performed to understand the underlying mechanism.

The main contributions of Chapters 3 to 5 are described as follows:

1. In Chapter 3, a systematic study of CO<sub>2</sub> in wedge pores under subcritical conditions were conducted with GCMC simulation. The effects of various factors: temperature, pore geometry (i.e., pore width, length, tilt angle and corrugation), on the formation of stepwise isotherms, were particularly investigated. The occurrence of this stepwise adsorption behaviour is correlated to the alternate packing between the commensurate and incommensurate along the pore axis direction. The steps faded with temperature, due to the adsorbates are less structured

and gradually receded mainly from the wide end where the weakest potential exerted to the fluids. The number of steps on desorption branch depends on the number of junctions and domains formed. The particles accumulating at the narrow end in open wedge pore play a role analogy to the closed end. Moreover, having corrugation on the interior solid surface also results different mechanisms illustrated in the stepwise behaviour due to the change in the actual pore size distribution and the interference to the force field inside the pore.

2. In Chapter 4, a systematic Monte Carlo simulation was conducted to evaluate the performance of two commonly used potential models of CO<sub>2</sub>, i.e. the simple 1C-LJ and the TraPPE 3C-LJ+3Q models, in different scenarios including bulk phase, adsorption on graphite surface and in carbonaceous pores. And a special investigation on the occurrence of step-wised hysteresis in wedge shaped pore that has been observed with other simple gases. It reveals the consideration of shape and quadrupole of CO<sub>2</sub> plays an important role in the description on the phase equilibria and adsorption behavior, especially at temperatures below the triple point.
3. In Chapter 5, a systematic Monte Carlo simulation was conducted to study the adsorption of binary mixtures containing CO<sub>2</sub> with CH<sub>4</sub> or N<sub>2</sub> at the ambient temperatures (i.e., 273 K – 298 K) in slit and wedge-shaped pores with graphitic surfaces. The results were also be compared with experimental data and with the predicted values using IAST method. Good agreement was found with the wedge pore model at low pressure ( $\geq 0.5$  MPa) for single and multicomponent adsorption of experimental data and IAST predictions while the combination of slit pore also well fitted or were close to the experimental data and was comparable to IAST predictions. When interadsorbate interactions become significant, IAST fails especially in predicting selectivity. The wedge pore model used mimics the presence of dead end in the ACs, which does impact the adsorption at low pressure region, and this cannot be captured with the uniform slit pore model. Therefore, the wedge pore model can be treated as an alternative model for representing the non-uniform pore size distribution in the AC.

The significance of this research are as follows:

1. The adsorption behaviours of pure CO<sub>2</sub> at subcritical conditions in the AC can be better elaborated with the application of a more realistic pore model. This application can facilitate the characterization of the physical properties of AC, including the surface area and pore size distributions.
2. The systematic study of the thermodynamic properties of CO<sub>2</sub> in bulk phase and adsorbed phase helps to evaluate and calibrate the thermal properties of the selected CO<sub>2</sub> potential model, which are the foundation for future theoretical studies of CO<sub>2</sub>.
3. It provides a fundamental understanding of the adsorption of CO<sub>2</sub> from natural gas mixtures containing CH<sub>4</sub> and N<sub>2</sub> at the molecular level for the AC. The information are essential for designing and optimizing the AC materials for adsorption and purification processes in industrial.

## 6.2 Recommendations

This research has provided microscopic perspectives on adsorption behaviours of pure and binary gas mixtures containing CO<sub>2</sub> in activated carbon and can be important compensation to experimental measurement, especially for certain conditions that are hard to accomplish. However, there are some possibilities for extending the results by considering the following:

1. Consider roles of molecular shape of CH<sub>4</sub> and N<sub>2</sub> on binary adsorption containing CO<sub>2</sub> in the AC.
2. Consider ternary or more mixture gases adsorption for comparison purposes.
3. Consider multiple wedge pore models for more realistic comparison purposes and to explore the connectivity between pores.
4. Consider roles of thiophene-type, sulfone and/or sulfoxide-containing functional groups on CO<sub>2</sub> and binary adsorption in the AC.



# References

- Allen, M. and D. Tildesley (1989). *Computer Simulation of Liquids*. New York: Oxford University Press.
- Bell, J. G., M. J. Benham, and K. M. Thomas (2021). Adsorption of carbon dioxide, water vapor, nitrogen, and sulfur dioxide on activated carbon for capture from flue gases: Competitive adsorption and selectivity aspects. *Energy & Fuels* 35(9), 8102–8116.
- Billemont, P., B. Coasne, and G. De Weireld (2011). An experimental and molecular simulation study of the adsorption of carbon dioxide and methane in nanoporous carbons in the presence of water. *Langmuir* 27(3), 1015–1024.
- Billemont, P., B. Coasne, and G. De Weireld (2013). Adsorption of carbon dioxide, methane, and their mixtures in porous carbons: Effect of surface chemistry, water content, and pore disorder. *Langmuir* 29(10), 3328–3338.
- Birkett, G. R. and D. Do (2004). PVT behaviour of fluids with potential models optimised for phase equilibria. *Fluid Ph. Equilibria* 224(2), 199–212.
- Bojan, M. and W. Steele (1988). Computer simulation of physisorption on a heterogeneous surface. *Surf. Sci.* 199(3), L395–L402.
- Bojan, M. and W. Steele (1993). Computer simulation of physical adsorption on stepped surfaces. *Langmuir* 9(10), 2569–2575.
- Bottani, E., V. Bakaev, and W. Steele (1994). A simulation/experimental study of the thermodynamic properties of carbon dioxide on graphite. *Chem. Eng. Sci.* 49(17), 2931–2939.

- Brennan, J. K., T. J. Bandosz, K. T. Thomson, and K. E. Gubbins (2001). Water in porous carbons. *Colloids Surf. A Physicochem. Eng. Asp.* 187-188, 539 – 568.
- Bruschi, L., G. Mistura, P. Phadungbut, D. D. Do, D. Nicholson, Y. Mayamei, and W. Lee (2015). Adsorption on ordered and disordered duplex layers of porous anodic alumina. *Langmuir* 31(17), 4895–4905.
- Bui, M., C. S. Adjiman, A. Bardow, E. J. Anthony, A. Boston, S. Brown, P. S. Fennell, S. Fuss, A. Galindo, L. A. Hackett, J. P. Hallett, H. J. Herzog, G. Jackson, J. Kemper, S. Krevor, G. C. Maitland, M. Matuszewski, I. S. Metcalfe, C. Petit, G. Puxty, J. Reimer, D. M. Reiner, E. S. Rubin, S. A. Scott, N. Shah, B. Smit, J. P. M. Trusler, P. Webley, J. Wilcox, and N. Mac Dowell (2018). Carbon capture and storage (CCS): the way forward. *Energy Environ. Sci.* 11, 1062–1176.
- Burgess, C. G. V., D. H. Everett, and S. Nuttall (1989). Adsorption hysteresis in porous materials. *Pure Appl. Chem.* 61(11), 1845–1852.
- Buss, E. (1995). Gravimetric measurement of binary gas adsorption equilibria of methane-carbon dioxide mixtures on activated carbon. *Gas Sep. Purif.* 9(3), 189–197.
- Chen, B., J. I. Siepmann, and M. L. Klein (2001). Direct gibbs ensemble monte carlo simulations for solidvapor phase equilibria: Applications to lennardjonesium and carbon dioxide. *J. Phys. Chem. B* 105(40), 9840–9848.
- Chen, G., J. Zhang, and S. Lu (2016). Adsorption behavior of hydrocarbon on illite. *Energy Fuels* 30, 9114.
- Cheng, S., T. Du, Y. Long, L. Liu, and G. Li (2020). Value added utilization of ferronickel slags as raw materials of 4A zeolite for CO<sub>2</sub> reduction. *Adsorption* 26, 1113–1126.
- Choi, B.-U., D.-K. Choi, Y.-W. Lee, B.-K. Lee, and S.-H. Kim (2003). Adsorption equilibria of methane, ethane, ethylene, nitrogen, and hydrogen onto activated carbon. *J. Chem. Eng. Data* 48(3), 603–607.

- Cochran, T., R. Kabel, and R. Danner (1985). Vacancy solution theory of adsorption using Flory-Huggins activity coefficient equations. *AIChE J.* *31*(2), 268–277.
- Cracknell, R. F., D. Nicholson, S. R. Tennison, and J. Bromhead (1996). Adsorption and selectivity of carbon dioxide with methane and nitrogen in slit-shaped carbonaceous micropores: Simulation and experiment. *Adsorption* *2*, 193–203.
- Dantas, S., K. C. Struckhoff, M. Thommes, and A. V. Neimark (2019). Phase behavior and capillary condensation hysteresis of carbon dioxide in mesopores. *Langmuir* *35*(35), 11291–11298.
- Dantas, S., K. C. Struckhoff, M. Thommes, and A. V. Neimark (2021). Pore size characterization of micro-mesoporous carbons using CO<sub>2</sub> adsorption. *Carbon* *173*, 842–848.
- de Boer, J. (1973). The structure and texture of a physical adsorbent. *Colloques Internationaux du CNRS* *201*, 407.
- de Oliveira, J. C. A., A. L. Galdino, D. V. Gonçalves, P. F. G. Silvino, C. L. Cavalcante, M. Bastos-Neto, D. C. Azevedo, and S. M. P. Lucena (2021). Representative pores: An efficient method to characterize activated carbons. *Front. Chem.* *8*, 1–9.
- de Tomas, C., A. Aghajamali, J. L. Jones, D. J. Lim, M. J. López, I. Suarez-Martinez, and N. A. Marks (2019). Transferability in interatomic potentials for carbon. *Carbon* *155*, 624–634.
- Diao, R., C. Fan, D. Do, and D. Nicholson (2015). On the 2D-transition, hysteresis and thermodynamic equilibrium of Kr adsorption on a graphite surface. *J. Colloid Interface Sci.* *460*, 281–289.
- Diao, R., C. Fan, D. Do, and D. Nicholson (2016). Monte Carlo simulation of adsorption-induced deformation in finite graphitic slit pores. *J. Phys. Chem. C* *120*(51), 29272–29282.
- Do, D. (1998). *Adsorption Analysis: Equilibria And Kinetics*. London: Imperial College Press.

- Do, D. and H. Do (2003). Pore characterization of carbonaceous materials by DFT and GCMC simulations: A review. *Adsorption Sci. Technol.* *21*(5), 389–424.
- Do, D. and H. Do (2005). Effects of potential models in the vapor–liquid equilibria and adsorption of simple gases on graphitized thermal carbon black. *Fluid Ph Equilibria* *236*(1), 169–177.
- Do, D. and H. Do (2006a). Effects of potential models on the adsorption of carbon dioxide on graphitized thermal carbon black: GCMC computer simulations. *Colloids Surf. A* *277*(1-3), 239–248.
- Do, D. and H. Do (2007). Appropriate volumes for adsorption isotherm studies: The absolute void volume, accessible pore volume and enclosing particle volume. *J. Colloid Interf. Sci.* *316*(2), 317 – 330.
- Do, D., S. Junpirom, D. Nicholson, and H. Do (2010). Importance of molecular shape in the adsorption of nitrogen, carbon dioxide and methane on surfaces and in confined spaces. *Colloids Surf. A* *353*(1), 10–29.
- Do, D. D. and H. D. Do (2006b). Adsorption of carbon tetrachloride on graphitized thermal carbon black and in slit graphitic pores: Five-site versus one-site potential models. *J Phys Chem B* *110*(19), 9520–9528.
- Do, D. D., H. D. Do, and D. Nicholson (2009). Molecular simulation of excess isotherm and excess enthalpy change in gas-phase adsorption. *J. Phys. Chem. B* *113*(4), 1030–1040.
- Do, D. D., L. Herrera, C. Fan, A. Wongkoblapp, and D. Nicholson (2010). The role of accessibility in the characterization of porous solids and their adsorption properties. *Adsorption* *16*, 3–15.
- Dong, K., F. Zeng, J. Jia, C. Chen, and Z. Gong (2019). Molecular simulation of the preferential adsorption of CH<sub>4</sub> and CO<sub>2</sub> in middle-rank coal. *Mol. Simul.* *45*, 15.
- Dreisbach, F., R. Staudt, and J. Keller (1999). High pressure adsorption data of methane, nitrogen, carbon dioxide and their binary and ternary mixtures on activated carbon. *Adsorption* *5*, 215–227.



- El Oufir, Z., H. Ramézani, N. Mathieu, and S. Delpoux (2021). Impact of adsorbent carbons and carbon surface conductivity on adsorption capacity of CO<sub>2</sub>, CH<sub>4</sub>, N<sub>2</sub> and gas separation. *Comput. Mater. Sci.* 199, 110572.
- Fan, C., D. Do, and D. Nicholson (2012). A new and effective Bin–Monte Carlo scheme to study vapour–liquid equilibria and vapour–solid equilibria. *Fluid Phase Equilib* 325, 53–65.
- Fan, C., D. Do, and D. Nicholson (2013). Condensation and evaporation in capillaries with nonuniform cross sections. *Ind. Eng. Chem. Res.* 52(39), 14304–14314.
- Fan, C., D. Do, D. Nicholson, and E. Ustinov (2013). A novel application of kinetic Monte Carlo method in the description of N<sub>2</sub> vapour–liquid equilibria and adsorption. *Chem Eng Sci* 90, 161–169.
- Foster, A. G. (1951). Sorption hysteresis. I. Some factors determining the size of the hysteresis loop. *J Phys Chem* 55(5), 638–643.
- Frenkel, D. and B. Smit (2002). *Understanding molecular simulation* (2 ed.). New York: Academic press.
- Frenkel, D., B. Smit, J. Tobochnik, S. McKay, and W. Christian (1997). Understanding molecular simulation. *Comput. Phys.* 11(4), 351–354.
- Gao, G. and W. Wang (1997). Gibbs ensemble Monte Carlo simulation of binary vapor-liquid equilibria for CFC alternatives. *Fluid Ph Equilibria* 130(1-2), 157–166.
- Goetz, V., O. Pupier, and A. Guillot (2006). Carbon dioxide-methane mixture adsorption on activated carbon. *Adsorption* 12, 55–63.
- Golebiowska, M., L. Firlej, B. Kuchta, and R. Fabianski (2009). Structural transformations of nitrogen adsorbed on graphite: Monte Carlo studies of spatial heterogeneity in multilayer system. *J. Chem. Phys.* 130(20), 204703.
- Guillot, A. and F. Stoeckli (2001). Reference isotherm for high pressure adsorption of CO<sub>2</sub> by carbons at 273 k. *Carbon* 39(13), 2059–2064.
- Guo, J., J. R. Morris, Y. Ihm, C. I. Contescu, N. C. Gallego, G. Duscher, S. J. Pennycook, and M. F. Chisholm (2012). Topological defects: Origin

- of nanopores and enhanced adsorption performance in nanoporous carbon. *Small* 8(21), 3283–3288.
- Hammonds, K., I. McDonald, and D. Tildesley (1990). Computational studies of the structure of carbon dioxide monolayers physisorbed on the basal plane of graphite. *Mol. Phys.* 70(2), 175–195.
- Han, J., A. K. Bogomolov, and E. Y. Makarova (2018). Molecular simulation of H<sub>2</sub>O, CO<sub>2</sub>, and CH<sub>4</sub> adsorption in coal micropores. *Russ. J. Phys. Chem. B* 12, 714.
- Han, S., S. Sang, J. Liang, and J. Zhang (2019). Supercritical CO<sub>2</sub> adsorption in a simulated deep coal reservoir environment, implications for geological storage of CO<sub>2</sub> in deep coals in the southern qinshui basin, china. *Energy Sci. Eng.* 7(2), 488–503.
- Hao, P., Y. Shi, S. Li, and N. Cai (2020). Hydrophobic activated carbon for elevated-temperature pressure swing adsorption. *Adsorption* 26, 1093–1100.
- Harris, J. G. and K. H. Yung (1995). Carbon dioxide’s liquid-vapor coexistence curve and critical properties as predicted by a simple molecular model. *J. Phys. Chem.* 99(31), 12021–12024.
- Heffelfinger, G. S., F. van Swol, and K. E. Gubbins (1988). Adsorption hysteresis in narrow pores. *J Chem Phys* 89(8), 5202–5205.
- Heuchel, M., G. M. Davies, E. Buss, and N. A. Seaton (1999). Adsorption of carbon dioxide and methane and their mixtures on an activated carbon: Simulation and experiment. *Langmuir* 15(25), 8695–8705.
- Hou, M., W. Qi, L. Li, R. Xu, J. Xue, Y. Zhang, C. Song, and T. Wang (2021). Carbon molecular sieve membrane with tunable microstructure for CO<sub>2</sub> separation: Effect of multiscale structures of polyimide precursors. *J. Membr. Sci.* 635, 119541.
- Huang, L., Z. Ning, and Q. Wang (2018). Effect of organic type and moisture on CO<sub>2</sub>/CH<sub>4</sub> competitive adsorption in kerogen with implications for CO<sub>2</sub> sequestration and enhanced CH<sub>4</sub> recovery. *Appl. Energy* 210, 28.

- Huang, L., L. Zhang, and Q. Shao (2007). Simulations of binary mixture adsorption of carbon dioxide and methane in carbon nanotubes: Temperature, pressure, and pore size effects. *J. Phys. Chem. C* 111, 11912.
- IEA (2022). Global energy review: Co2 emissions in 2021. Technical report, IEA Paris.
- Inagaki, M. and F. Kang (2014). *Materials science and engineering of carbon: Fundamentals*. Elsevier Science.
- IPCC (2021). Climate change 2021: The physical science basis. contribution of working group i to the sixth assesment report of the intergovernmental panel on climate change. Technical report, Cambridge University Press.
- Jagiello, J. and J. P. Olivier (2013). Carbon slit pore model incorporating surface energetical heterogeneity and geometrical corrugation. *Adsorption* 19(2-4), 777–783.
- Johnson, J. K., J. A. Zollweg, and K. E. Gubbins (1993). The Lennard-Jones equation of state revisited. *Mol. Phys.* 78(3), 591–618.
- Kidnay, A., W. Parrish, and D. McCartney (2019). *Fundamentals of Natural Gas Processing*. USA: CRC Press.
- Kirk, R. and D. Othmer (2004). *Encyclopedia of Chemical Technology*. Number 493-527. Chichester: Wiley & Sons.
- Kirkwood, J. G. and F. P. Buff (1949). The statistical mechanical theory of surface tension. *J. Chem. Phys.* 17(3), 338–343.
- Klomkliang, N., D. Do, and D. Nicholson (2014). Hysteresis loop and scanning curves of argon adsorption in closed-end wedge pores. *Langmuir* 30(43), 12879–12887.
- Kofke, D. A. (1993). Direct evaluation of phase coexistence by molecular simulation via integration along the saturation line. *J Chem Phys* 98(5), 4149–4162.
- Kohmuean, P., W. Inthomya, A. Wongkoblaph, and C. Tangsathitkulchai (2021). Monte Carlo simulation and experimental studies of CO<sub>2</sub>, CH<sub>4</sub> and their mixture capture in porous carbons. *Molecules* 26(9), 2413.

- Kouetcha, D. N., H. Ramézani, N. Mathieu-Cohaut, and S. K. Bhatia (2018). Carbon dioxide adsorption through carbon adsorbent structures: Effect of the porosity size, chemical potential and temperature. *Comput. Mater. Sci.* 151, 255–272.
- Kowalczyk, P., P. A. Gauden, A. P. Terzyk, S. Furmaniak, and P. J. F. Harris (2012). Displacement of methane by coadsorbed carbon dioxide is facilitated in narrow carbon nanopores. *J. Phys. Chem.* 116(25), 13640–13649.
- Kuchta, B. and R. D. Etters (1987). Calculated properties of monolayer and multilayer N<sub>2</sub> on graphite. *Phys. Rev. B* 36, 3400–3406.
- Kurniawan, Y., S. K. Bhatia, and V. Rudolph (2005). Simulation of binary mixture adsorption of methane and CO<sub>2</sub> at supercritical conditions in carbons. *AIChE J.* 52(3), 957–967.
- Kurniawan, Y., S. K. Bhatia, and V. Rudolph (2006). Simulation of binary mixture adsorption of methane and CO<sub>2</sub> at supercritical conditions in carbons. *AIChE J.* 52(3), 957–967.
- I. Vortler, H., O. N. IV, and M. Lisal (1997). The exp-6 potential fluid at very high pressures: computer simulations and theory. *Mol Phys* 92(5), 813–824.
- Lemmon, E., M. McLinden, and D. Friend (2018). *Thermophysical Properties of Fluid System in NIST Chemistry WebBook*. Gaithersburg, MD: NIST Standard Reference Database Number 69.
- Linse, P. (1987). Monte carlo simulation of liquid–liquid benzene–water interface. *J. Chem. Phys.* 86(7), 4177–4187.
- Liu, X., C. Fan, and D. Do (2019). Microscopic characterization of xenon adsorption in wedge pores. *Adsorption* 25, 1043–1055.
- Liu, X., C. Fan, D. Do, and C. F. Leong (2020). On the hysteresis of low temperature adsorption of xenon in graphitic wedge pore. *Chem Eng J* 390, 124499.
- Liu, X., C. Fan, D. Do, V. Pareek, and P. Yang (2020). A temperature-dependent potential model for mercury in the description of vapour-liquid equilibrium & adsorption in activated carbon. *Chem Eng Sci* 215, 115453.

- Loi, Q., L. Prasetyo, J. Tan, D. Do, and D. Nicholson (2020a). Wedge pore modelling of gas adsorption in activated carbon: Consistent pore size distributions. *Carbon* 166, 414–426.
- Loi, Q. K., L. Prasetyo, S. Tan, D. Do, and D. Nicholson (2020b). Order-disorder transition of an argon adsorbate in graphitic wedge pores. *Chem. Eng. J.* 384, 123286.
- Lotfi, A., J. Vrabec, and J. Fischer (1992). Vapour liquid equilibria of the Lennard-Jones fluid from the NpT plus test particle method. *Mol. Phys.* 76(6), 1319–1333.
- Lozano-Castelló, D., D. Cazorla-Amorós, and A. Linares-Solano (2004). Usefulness of CO<sub>2</sub> adsorption at 273 K for the characterization of porous carbons. *Carbon* 42(7), 1233–1242.
- Madden, D. G., R. Babu, J. S.-A. T. C. Ceren Çamur, Nakul Rampal, and D. Fairen-Jimenez (2021). Monolithic metal–organic frameworks for carbon dioxide separation. *Faraday Discuss.* 231, 51–65.
- Malbrunot, P., D. Vidal, J. Vermesse, R. Chahine, and T. K. Bose (1992). Adsorption measurements of argon, neon, krypton, nitrogen, and methane on activated carbon up to 650 MPa. *Langmuir* 8(2), 577–580.
- Malbrunot, P., D. Vidal, J. Vermesse, R. Chahine, and T. K. Bose (1997). Adsorbent helium density measurement and its effect on adsorption isotherms at high pressure. *Langmuir* 13(3), 539–544.
- Marsh, H. and F. Reinoso (2006). *Activated Carbon*. United Kingdom: Elsevier Ltd.
- Masel, R. (1996). *Principles of Adsorption and Reaction on Solid Surfaces*. Wiley Series in Chemical Engineering. USA: John Wiley & Sons.
- McDonald, I. (1972). NPT-ensemble Monte Carlo calculations for binary liquid mixtures. *Mol. Phys.* 23(1), 41–58.
- Mick, J. R., M. Soroush Barhaghi, B. Jackman, K. Rushaidat, L. Schwiebert, and J. J. Potoff (2015). Optimized Mie potentials for phase equilibria: Application to noble gases and their mixtures with n-alkanes. *J Chem Phys* 143(11), 114504.

- Mohamedali, M., A. Henni, and H. Ibrahim (2019). Investigation of CO<sub>2</sub> capture using acetate-based ionic liquids incorporated into exceptionally porous metal–organic frameworks. *Adsorption* 25, 675–692.
- Möller, D. and J. Fischer (1994). Determination of an effective intermolecular potential for carbon dioxide using vapour-liquid phase equilibria from NpT + test particle simulations. *Fluid Ph. Equilibria* 100, 35–61.
- Morales-Ospino, R., Y. Goltzman, A. E. B. Torres, E. Vilarrasa-García, M. Bastos-Neto, C. L. C. Jr, D. C. S. Azevedo, C. R. M. Marques, T. F. de Aquino, and V. R. de Oliveira (2020). Assessment of the potential use of zeolites synthesized from power plant fly ash to capture CO<sub>2</sub> under post-combustion scenario. *Adsorption* 26, 1153–1164.
- Morali, U., H. Demiral, and S. Sensoz (2019). Synthesis of carbon molecular sieve for carbon dioxide adsorption: Chemical vapor deposition combined with Taguchi design of experiment method. *Powder Technol.* 355, 716–726.
- Morishige, K. and Y. Nakamura (2004). Nature of adsorption and desorption branches in cylindrical pores. *Langmuir* 20(11), 4503–4506.
- Morishige, K., M. Tateishi, F. Hirose, and K. Aramaki (2006). Change in desorption mechanism from pore blocking to cavitation with temperature for nitrogen in ordered silica with cage-like pores. *Langmuir* 22(22), 9220–9224.
- Mosher, K., J. He, Y. Liu, E. Rupp, and J. Wilcox (2013). Molecular simulation of methane adsorption in micro- and mesoporous carbons with applications to coal and gas shale systems. *Int. J. Coal Geol.* 109-110, 36.
- Mountain, R. and D. Thirumalai (1994). Quantative measure of efficiency of monte carlo simulations. *Phys. A* 210(3-4), 453–460.
- Mukherjee, A., J. A. Okolie, A. Abdelrasoul, C. Niu, and A. K. Dalai (2019). Review of post-combustion carbon dioxide capture technologies using activated carbon. *J. Environ. Sci.* 83, 46 – 63.
- Murthy, C., S. O’Shea, and I. McDonald (1983). Electrostatic interactions in molecular crystals lattice dynamics of solid nitrogen and carbon dioxide. *Mol. Phys.* 50(3), 531–541.

- Myers, A. and J. Prausnitz (1965). Thermodynamics of mixed-gas adsorption. *AIChE J.* 11(1), 121–127.
- Nguyen, C. and D. D. Do (1999). A new method for the characterization of porous materials. *Langmuir* 15(10), 3608–3615.
- Nguyen, P., C. Fan, D. Do, and D. Nicholson (2013). On the cavitation-like pore blocking in ink-bottle pore: Evolution of hysteresis loop with neck size. *J. Phys. Chem. C* 117(10), 5475–5484.
- Nguyen, T. X. and S. K. Bhatia (2004). Characterization of pore wall heterogeneity in nanoporous carbons using adsorption: the slit pore model revisited. *J. Phys. Chem B* 108(37), 14032–14042.
- Nguyen, V. T., C. Fan, M. A. Razak, D. Do, D. Nicholson, and E. Ustinov (2013). Development of kinetic Monte Carlo and bin-Monte Carlo schemes for simulation of mixtures – vapor–liquid equilibria & adsorption. *Chem Eng Sci* 102, 220–226.
- Nguyen, V. T., T. Horikawa, D. Do, and D. Nicholson (2013). On the relative strength of adsorption of gases on carbon surfaces with functional groups: fluid–fluid, fluid–graphite and fluid–functional group interactions. *Carbon* 61, 551–557.
- Nicholson, W., D. Nicholson, and N. Parsonage (1982). *Computer Simulation and the Statistical Mechanics of Adsorption*. United Kingdom: Academic Press.
- Norman, G. and V. Filinov (1969). Investigation of phase transitions by a Monte Carlo method. *High Temperature (USSR)*, 216–222.
- Okumura, H. and F. Yonezawa (2000). Liquid–vapor coexistence curves of several interatomic model potentials. *J Chem Phys* 113(20), 9162–9168.
- Palmer, J. C., J. D. Moore, T. J. Roussel, J. K. Brennan, and K. E. Gubbins (2011). Adsorptive behavior of CO<sub>2</sub>, CH<sub>4</sub> and their mixtures in carbon nanospace: a molecular simulation study. *Phys. Chem. Chem. Phys.* 13, 3985–3996.
- Pan, J., Q. Niu, K. Wang, X. Shi, and M. Li (2016). The closed pores of tectonically deformed coal studied by small-angle X-ray scattering and liquid nitrogen adsorption. *Microporous Mesoporous Mater.* 224, 245–252.

- Panagiotopoulos, A. Z. (1987). Direct determination of phase coexistence properties of fluids by Monte Carlo simulation in a new ensemble. *Mol Phys* 61(4), 813–826.
- Panagiotopoulos, A. Z. (1992). Direct determination of fluid phase equilibria by simulation in the gibbs ensemble: A review. *Mol Simul* 9(1), 1–23.
- Panagiotopoulos, A. Z. (1996). Current advances in Monte Carlo methods. *Fluid Ph Equilibria* 116(1), 257–266.
- Panagiotopoulos, A. Z. (1999). Monte Carlo methods for phase equilibria of fluids. *J. Phys. Condens. Matter* 12(3), R25–R52.
- Potoff, J. and J. Siepmann (2001). Vapor-liquid equilibria of mixtures containing alkanes, carbon dioxide, and nitrogen. *AIChE J.* 47(7), 1676–1682.
- Potoff, J. J., J. R. Errington, and A. Z. Panagiotopoulos (1999). Molecular simulation of phase equilibria for mixtures of polar and non-polar components. *Mol Phys* 97(10), 1073–1083.
- Prasetyo, L., T. Horikawa, P. Phadungbut, S. J. Tan, D. Do, and D. Nicholson (2016). A GCMC simulation and experimental study of krypton adsorption/desorption hysteresis on a graphite surface. *J. Colloid Interface Sci.* 478, 402–412.
- Rai, N. and J. I. Siepmann (2007). Transferable potentials for phase equilibria. 9. Explicit hydrogen description of benzene and five-membered and six-membered heterocyclic aromatic compounds. *J Phys Chem B* 111(36), 10790–10799.
- Rasmussen, C. J., A. Vishnyakov, M. Thommes, B. M. Smarsly, F. Kleitz, and A. V. Neimark (2010). Cavitation in metastable liquid nitrogen confined to nanoscale pores. *Langmuir* 26(12), 10147–10157.
- Ravikovitch, P. I., S. C. O. Domhnaill, A. V. Neimark, F. Schueth, and K. K. Unger (1995). Capillary hysteresis in nanopores: Theoretical and experimental studies of nitrogen adsorption on MCM-41. *Langmuir* 11(12), 4765–4772.
- Ravikovitch, P. I. and A. V. Neimark (2002a). Density functional theory of adsorption in spherical cavities and pore size characterization of templated



- nanoporous silicas with cubic and three-dimensional hexagonal structures. *Langmuir* 18(5), 1550–1560.
- Ravikovitch, P. I. and A. V. Neimark (2002b). Experimental confirmation of different mechanisms of evaporation from ink-bottle type pores: Equilibrium, pore blocking, and cavitation. *Langmuir* 18(25), 9830–9837.
- Ravikovitch, P. I., A. Vishnyakov, and A. V. Neimark (2001). Density functional theories and molecular simulations of adsorption and phase transitions in nanopores. *Phys. Rev. E* 64, 011602.
- Ravikovitch, P. I., A. Vishnyakov, R. Russo, and A. V. Neimark (2000). Unified approach to pore size characterization of microporous carbonaceous materials from N<sub>2</sub>, Ar, and CO<sub>2</sub> adsorption isotherms. *Langmuir* 16(5), 2311–2320.
- Rosalind, E. F. (1951). Crystallite growth in graphitizing and non-graphitizing carbons. *Proc. R. Soc. London, Ser. A* 209, 196–218.
- Rouquerol, J., D. Avnir, C. W. Fairbridge, D. H. Everett, J. M. Haynes, N. Pernicone, J. D. F. Ramsay, K. S. W. Sing, and K. K. Unger (1994). Recommendations for the characterization of porous solids. *Pure Appl. Chem.* 66(8), 1739–1758.
- Ruthen, D. M. (1984). *Principles of Adsorption and Adsorption Processes*. New York: Wiley.
- Sánchez-Zambrano, K. S., E. Vilarrasa-García, D. A. S. Maia, M. Bastos-Neto, E. Rodríguez-Castellon, and D. C. S. Azevedo (2020). Adsorption microcalorimetry as a tool in the characterization of amine-grafted mesoporous silicas for CO<sub>2</sub> capture. *Adsorption* 26, 165–175.
- Santiago, R. G., R. M. Siqueira, C. A. Alves, E. Vilarrasa-García, D. A. S. Maia, M. Bastos-Neto, and D. C. S. de Azevedo (2020). Evaluation of the thermal regeneration of an amine-grafted mesoporous silica used for CO<sub>2</sub>/N<sub>2</sub> separation. *Adsorption* 26, 203–215.
- Sha, H., S. Zhang, and R. Faller (2018). Molecular investigation of gas adsorption, separation, and transport on carbon nanoscrolls: A combined grand canonical Monte Carlo and molecular dynamics study. *Carbon* 132, 401.

- Sholl, D. and J. Steckel (2011). *Density Functional Theory: A Practical Introduction*. USA: John Wiley & Sons.
- Siegelman, R. L., E. J. Kim, and J. R. Long (2021). Porous materials for carbon dioxide separations. *Nat. Mater.* *20*, 1060–1072.
- Simon, C., B. Smit, and M. Haranczyk (2016). PyIAST: Ideal adsorbed solution theory (IAST) Python package. *Comput. Phys. Commun* *200*, 364–380.
- Sizova, A. A., V. V. Sizov, and E. N. Brodskaya (2018). Molecular mechanisms of the effect of water on CO<sub>2</sub>/CH<sub>4</sub> mixture adsorption in slit like carbon pores. *Colloid J.* *80*, 439.
- Speight, J. G. (2019). *Natural Gas (Second Edition)* (Second Edition ed.). Boston: Gulf Professional Publishing.
- Spencer, W. B., C. H. Amberg, and R. A. Beebe (1958). Further studies of adsorption on graphitized carbon blacks. *J. Phys. Chem.* *62*(6), 719–723.
- Steele, W. A. (1973a). The physical interaction of gases with crystalline solids: I. Gas-solid energies and properties of isolated adsorbed atoms. *Surf. Sci.* *36*(1), 317 – 352.
- Steele, W. A. (1973b). The physical interaction of gases with crystalline solids: II. Two-dimensional second and third virial coefficients. *Surf. Sci.* *39*(1), 149 – 175.
- Steele, W. A. (1996). Monolayers of linear molecules adsorbed on the graphite basal plane: Structures and intermolecular interactions. *Langmuir* *12*(1), 145–153.
- Sun, Y., D. Spellmeyer, D. A. Pearlman, and P. Kollman (1992). Simulation of the solvation free energies for methane, ethane, and propane and corresponding amino acid dipeptides: A critical test of the bond-PMF correction, a new set of hydrocarbon parameters, and the gas phase-water hydrophobicity scale. *J. Am. Chem. Soc.* *114*(17), 6798–6801.
- Suwanayuen, S. and R. Danner (1980). A gas adsorption isotherm equation based on vacancy solution theory. *AIChE J.* *26*(1), 68–76.

- Sweatman, M. B. and N. Quirke (2005). Modelling gas mixture adsorption in active carbons. *Mol. Simul.* 31(9), 667–681.
- Swisher, J., L.-C. Lin, J. Kim, and B. Smit (2013). Evaluating mixture adsorption models using molecular simulation. *AIChE J.* 59(8), 3054–3064.
- Tan, S., D. Do, and D. Nicholson (2020). Consistency of NVT, NPT,  $\mu$ VT and gibbs (NV<sup>2</sup>T and NPT) with kinetic Monte Carlo schemes. *Chem. Eng. J.* 401.
- Tan, S., D. D. Do, and D. Nicholson (2016). An efficient method to determine chemical potential of mixtures in the isothermal and isobaric bulk phase with kinetic Monte Carlo simulation. *Mol. Phys.* 114(2), 186–196.
- Tan, S. J., L. Liu, and J. W. Chew (2021). Competitive and synergistic adsorption of mixtures of polar and nonpolar gases in carbonaceous nanopores. *Langmuir* 37(22), 6754–6764.
- Terlain, A. and Y. Larher (1983). Phase diagrams of films of linear molecules with large quadrupole moments (CO<sub>2</sub>, N<sub>2</sub>O, C<sub>2</sub>N<sub>2</sub>) adsorbed on graphite. *Surface Science* 125(1), 304–311.
- Thommes, M., K. Kaneko, A. V. Neimark, J. P. Olivier, F. Rodriguez-Reinoso, J. Rouquerol, and K. S. Sing (2015). Physisorption of gases, with special reference to the evaluation of surface area and pore size distribution (iupac technical report). *Pure Appl. Chem.* 87(9-10), 1051–1069.
- Tompsett, G. A., L. Krogh, D. W. Griffin, and W. C. Conner (2005). Hysteresis and scanning behavior of mesoporous molecular sieves. *Langmuir* 21(18), 8214–8225.
- Trinh, T. T., K.-Q. Tran, Q.-V. Bach, and D. Q. Trinh (2016). A molecular dynamics simulation study on separation selectivity of CO<sub>2</sub>/CH<sub>4</sub> mixture in mesoporous carbons. *Energy Procedia* 86, 144 – 149.
- Vega, L., E. de Miguel, L. F. Rull, G. Jackson, and I. A. McLure (1992). Phase equilibria and critical behavior of square-well fluids of variable width by gibbs ensemble Monte Carlo simulation. *J Chem Phys* 96(3), 2296–2305.

- Velasco, L., R. Guillet-Nicolas, G. Dobos, M. Thommes, and P. Lodewyckx (2016). Towards a better understanding of water adsorption hysteresis in activated carbons by scanning isotherms. *Carbon* 96, 753–758.
- Vorokhta, M., J. Morávková, M. Dopita, A. Zhigunov, M. Šlouf, R. Pilař, and P. Sazama (2021). Effect of micropores on CO<sub>2</sub> capture in ordered mesoporous CMK-3 carbon at atmospheric pressure. *Adsorption* 27, 1221–1236.
- Walton, K. and D. Sholl (2015). Predicting multicomponent adsorption: 50 years of the ideal adsorbed solution theory. *AIChE J.* 61(9), 2757–2762.
- Wang, G., J. Jiang, K. Sun, and J. Wu (2018). An improved theoretical procedure for the pore-size analysis of activated carbon by gas adsorption. *Chin. J. Chem. Eng.* 26(3), 551–559.
- Widom, B. (1982). Potential-distribution theory and the statistical mechanics of fluids. *J. Phys. Chem.* 86(6), 869–872.
- Wood, W. W. (1968). Monte Carlo calculations for hard disks in the isothermal-isobaric ensemble. *J. Chem. Phys.* 48(1), 415–434.
- Wu, H., J. Chen, and H. Liu (2015). Molecular dynamics simulations about adsorption and displacement of methane in carbon nanochannels. *J. Phys. Chem. C* 119, 13652.
- Xiang, J., F. Zeng, H. Liang, B. Li, and X. Song (2014). Molecular simulation of the CH<sub>4</sub>/CO<sub>2</sub>/H<sub>2</sub>O adsorption onto the molecular structure of coal. *Sci. China Earth Sci.* 57(8), 1749–1759.
- Xiong, J., X. Liu, L. Liang, and Q. Zeng (2017). Methane adsorption on carbon models of the organic matter of organic-rich shales. *Energy Fuels* 31, 1489.
- Xu, H., K. Phothong, D. Do, and D. Nicholson (2021). Wetting/non-wetting behaviour of quadrupolar molecules (N<sub>2</sub>, C<sub>2</sub>H<sub>4</sub>, CO<sub>2</sub>) on planar substrates. *Chem. Eng. J.* 419, 129502.
- Xu, H., Y. Zeng, D. D. Do, and D. Nicholson (2019). On the nonwetting/wetting behavior of carbon dioxide on graphite. *J. Phys. Chem. C* 123(14), 9112–9120.

- Yang, L., X. Zhou, K. Zhang, F. Zeng, and Z. Wang (2018). Investigation of dynamical properties of methane in slit-like quartz pores using molecular simulation. *RSC Adv.* 8, 33798.
- Yang, Y., A. K. Narayanan Nair, and S. Sun (2020). Adsorption and diffusion of carbon dioxide, methane, and their mixture in carbon nanotubes in the presence of water. *J Phys Chem C* 124(30), 16478–16487.
- Yoshioka, T., T. Tsuru, and M. Asaeda (2004). Molecular dynamics study of gas permeation through amorphous silica network and inter-particle pores on microporous silica membranes. *Mol. Phys.* 102(2), 191–202.
- Yu, S., Z. Yan-ming, and L. Wu (2017). Macromolecule simulation and CH<sub>4</sub> adsorption mechanism of coal vitrinite. *Appl. Surf. Sci.* 396, 291.
- Zeng, Y., D. D. Do, and D. Nicholson (2015). Existence of ultrafine crevices and functional groups along the edge surfaces of graphitized thermal carbon black. *Langmuir* 31(14), 4196–4204.
- Zeng, Y., P. Phadungbut, D. D. Do, and D. Nicholson (2014). Anatomy of adsorption in open-end and closed-end slit mesopores: Adsorption, desorption, and equilibrium branches of hysteresis loop. *J Phys. Chem. C* 118(44), 25496–25504.
- Zeng, Y., L. Prasetyo, S. J. Tan, C. Fan, D. Do, and D. Nicholson (2017). On the hysteresis of adsorption and desorption of simple gases in open end and closed end pores. *Chem Eng Sci* 158, 462–479.
- Zhang, B., J. Kang, and T. Kang (2018). Monte carlo simulations of methane adsorption on kaolinite as a function of pore size. *J. Nat. Gas Sci. Eng.* 49, 410.
- Zhang, J., K. Liu, M. B. Clennell, D. N. Dewhurst, and M. Pervukhina (2015). Molecular simulation of CO<sub>2</sub>-CH<sub>4</sub> competitive adsorption and induced coal swelling. *Fuel* 160, 309.
- Zhou, W., H. Wang, Z. Zhang, H. Chen, and X. Liu (2019). Molecular simulation of CO<sub>2</sub>/CH<sub>4</sub>/H<sub>2</sub>O competitive adsorption and diffusion in brown coal. *RSC Adv.* 9, 3004.

Zhou, W., Z. Zhang, H. Wang, Y. Yan, and X. Liu (2018). Molecular insights into competitive adsorption of CO<sub>2</sub>/CH<sub>4</sub> mixture in shale nanopores. *RSC Adv.* 8, 33939.

*Every reasonable effort has been made to acknowledge the owners of copyright material. I would be pleased to hear from any copyright owner who has been omitted or incorrectly acknowledged.*

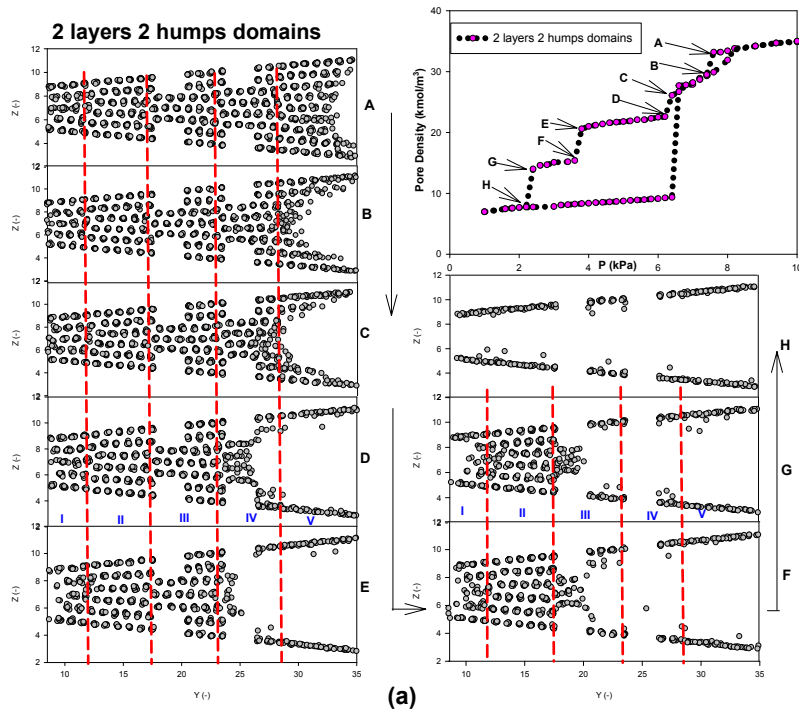
# Appendices





# Appendix A

## Two Layers Two Humps



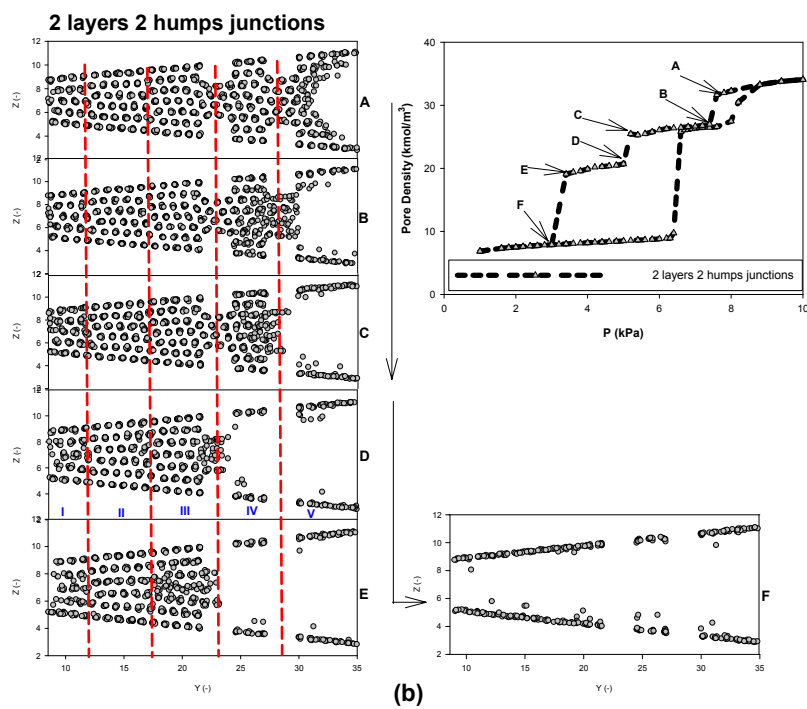
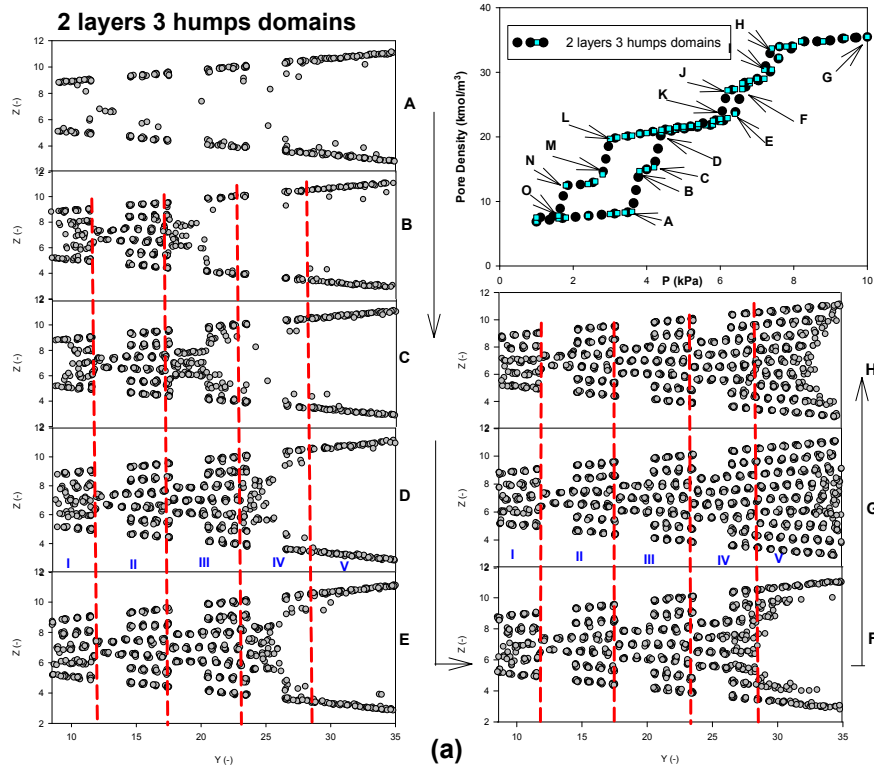


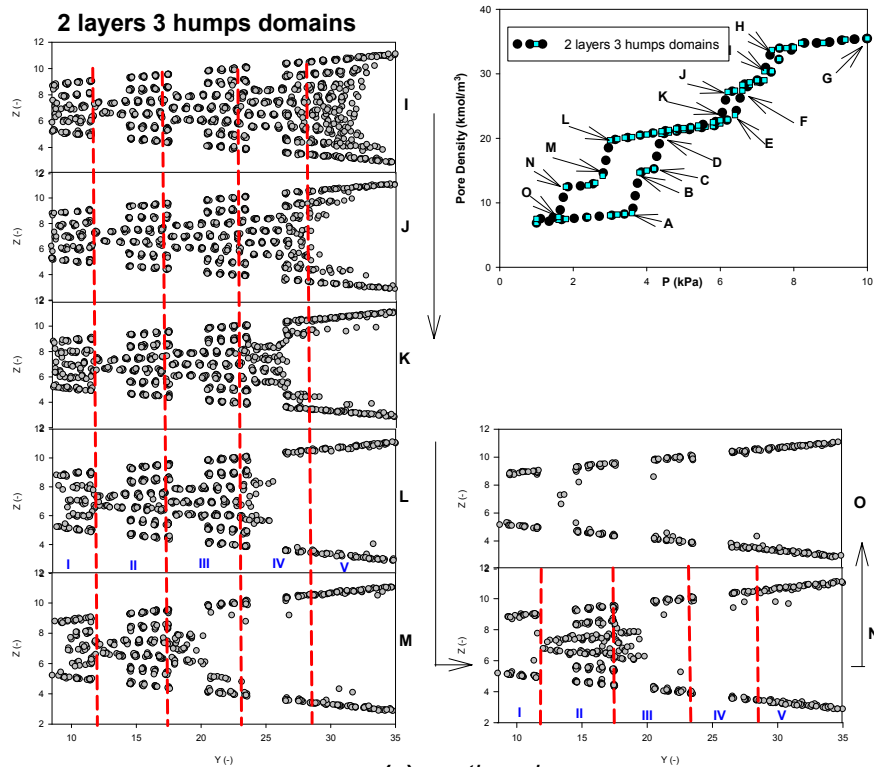
**Figure A.1.** Snapshots for CO<sub>2</sub> adsorption at 150K in wedge pore having two humps located (a) at domains; (b) at junctions; SH=2nm, L=10nm and  $\alpha=5^\circ$ .

# Appendix B

## Two Layers Three Humps



(a)



(a) continued

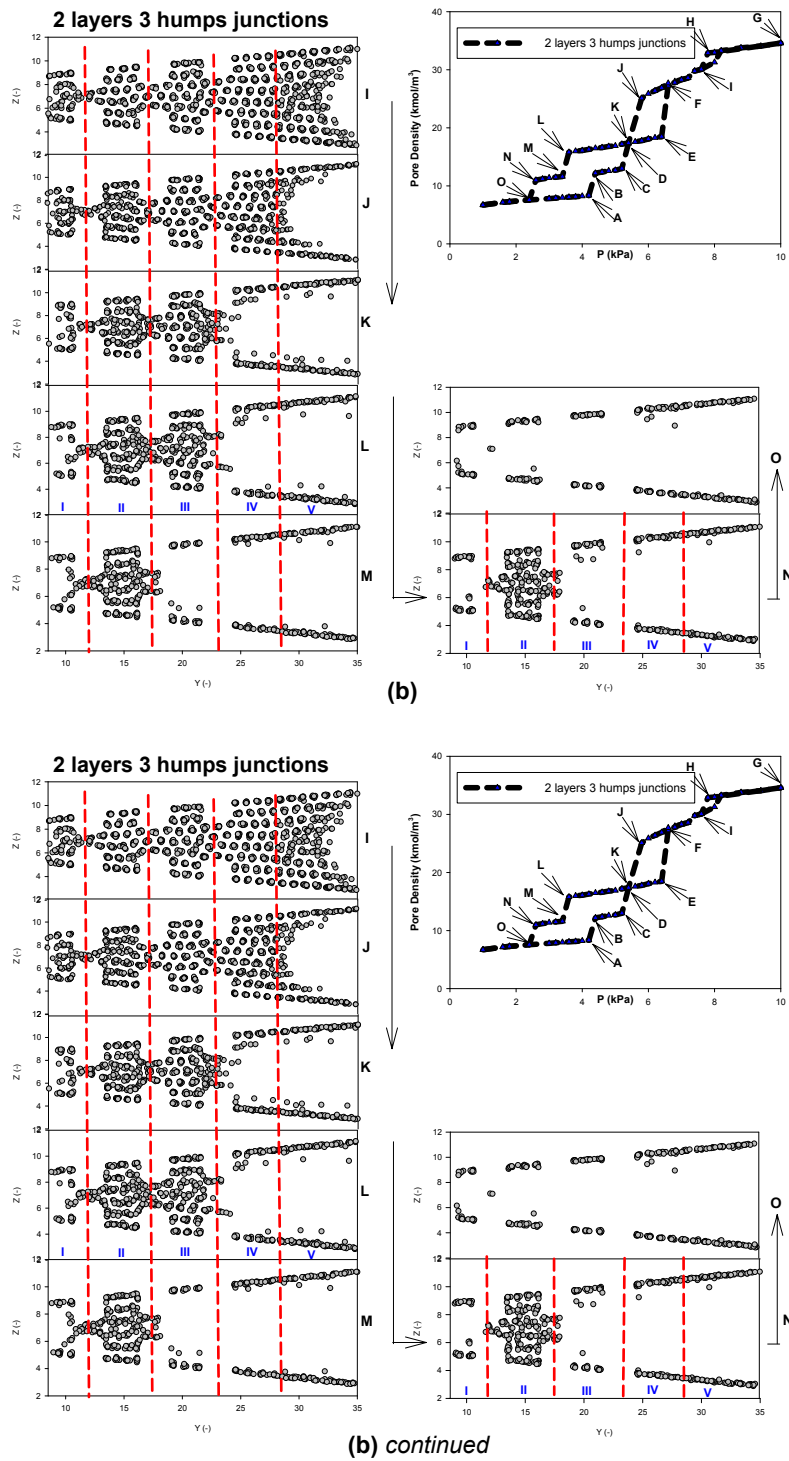



**Figure B.1.** Snapshots for  $\text{CO}_2$  adsorption at 150K in wedge pore having three humps located (a) at domains; (b) at junctions;  $\text{SH}=2\text{nm}$ ,  $\text{L}=10\text{nm}$  and  $\alpha=5^\circ$ .



# Appendix C

## Pore Size Distribution of Activated Carbon

 <p>ACS Publications Most Trusted. Most Cited. Most Read.</p>	<p>Characterization of Pore Wall Heterogeneity in Nanoporous Carbons Using Adsorption: the Slit Pore Model Revisited</p> <p>Author: Thanh X. Nguyen, Suresh K. Bhatia</p> <p>Publication: The Journal of Physical Chemistry B</p> <p>Publisher: American Chemical Society</p> <p>Date: Sep 1, 2004</p> <p>Copyright © 2004, American Chemical Society</p>
--	---

---

PERMISSION/LICENSE IS GRANTED FOR YOUR ORDER AT NO CHARGE

This type of permission/license, instead of the standard Terms and Conditions, is sent to you because no fee is being charged for your order. Please note the following:

- Permission is granted for your request in both print and electronic formats, and translations.
- If figures and/or tables were requested, they may be adapted or used in part.
- Please print this page for your records and send a copy of it to your publisher/graduate school.
- Appropriate credit for the requested material should be given as follows: "Reprinted (adapted) with permission from {COMPLETE REFERENCE CITATION}. Copyright {YEAR} American Chemical Society." Insert appropriate information in place of the capitalized words.
- One-time permission is granted only for the use specified in your RightsLink request. No additional uses are granted (such as derivative works or other editions). For any uses, please submit a new request.

If credit is given to another source for the material you requested from RightsLink, permission must be obtained from that source.

**Figure C.1.** Reprinted (adapted) with permission from T. X. Nguyen, S. K. Bhatia, Characterization of pore wall heterogeneity in nanoporous carbons using adsorption: the slit pore model revisited, J. Phys. Chem B 108 (37) (2004) 14032–14042. doi:10.1021/jp049048f. Copyright 2022 American Chemical Society.





# Appendix D

## Comparison of Potential Profiles

Infinite Steele potential model vs. Finite Bojan model with Three Graphene Layers

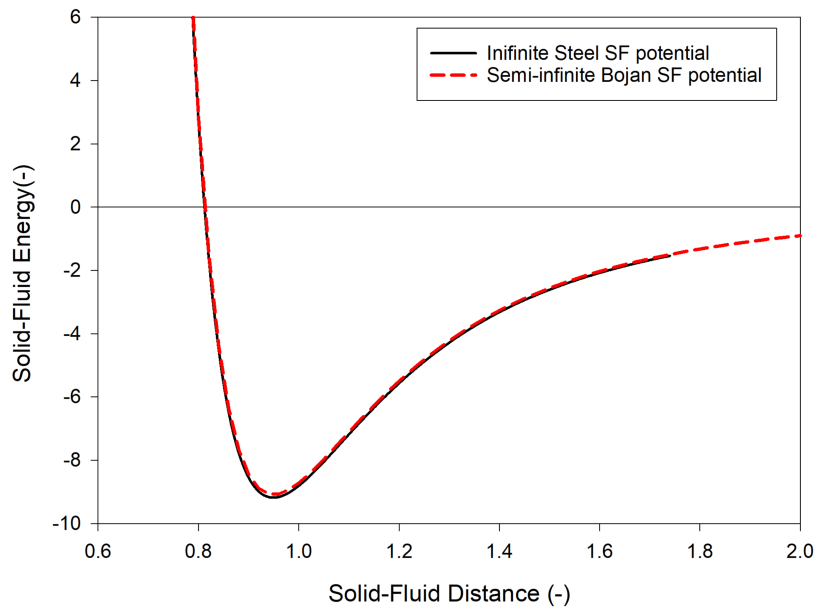


**Figure D.1.** The comparison of the potential profiles of a single Lennard-Jones fluid particle with the conventional Steele potential model and the Bojan potential, which is composed of three graphene layers, and with the same length as the pore models applied in Chapter 5, i.e.  $L=8.5\text{nm}$ .



# Appendix E

## Reprinted with Permission

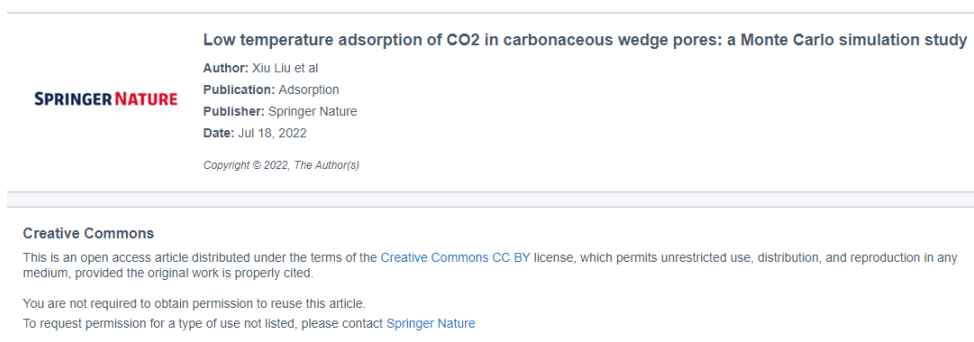


**Figure E.1.** Reprinted (adapted) with permission from Xiu Liu, Allan Hua Heng Sim & Chunyan Fan Low temperature adsorption of CO<sub>2</sub> in carbonaceous wedge pores: a Monte Carlo simulation study. Adsorption (2022). <https://doi.org/10.1007/s10450-022-00363-x>. Copyright 2022 Springer Nature.

The effects of potential model of CO<sub>2</sub> on its bulk phase properties and adsorption on surfaces and in pores

Author: Xiu Liu, , Allan Hua Heng Sim, et al  
Publication: Molecular Simulation  
Publisher: Taylor & Francis  
Date: Jun 15, 2022  
*Rights managed by Taylor & Francis*

---

**Thesis/Dissertation Reuse Request**

Taylor & Francis is pleased to offer reuses of its content for a thesis or dissertation free of charge contingent on resubmission of permission request if work is published.

[BACK](#) [CLOSE](#)

**Figure E.2.** Reprinted (adapted) with permission from Xiu Liu, Allan Hua Heng Sim & Chunyan Fan (2022) The effects of potential model of CO<sub>2</sub> on its bulk phase properties and adsorption on surfaces and in pores, Molecular Simulation, <https://doi.org/10.1080/08927022.2022.2086276>. Copyright 2022 Taylor & Francis

---

**Re: Obtain permission request - Journal (1291796) [220808-021079]**

**Rights and Permissions (ELS)** <Permissions@elsevier.com>  
Reply-To: "Rights and Permissions (ELS)" <Permissions@elsevier.com>  
To: sim.allan.hh@gmail.com

Wed, Aug 10, 2022 at 6:09 AM

Dear Mr Allan Hua Heng Sim Sim

We hereby grant you permission to reprint the material below at no charge in your thesis subject to the following conditions:

1. If any part of the material to be used (for example, figures) has appeared in our publication with credit or acknowledgement to another source, permission must also be sought from that source. If such permission is not obtained then that material may not be included in your publication/copies.

2. Suitable acknowledgment to the source must be made, either as a footnote or in a reference list at the end of your publication, as follows:

"This article was published in Publication title, Vol number, Author(s), Title of article, Page Nos, Copyright Elsevier (or appropriate Society name) (Year)."

3. Your thesis may be submitted to your institution in either print or electronic form.

4. Reproduction of this material is confined to the purpose for which permission is hereby given.

5. This permission is granted for non-exclusive world English rights only. For other languages please reapply separately for each one required. Permission excludes use in an electronic form other than submission. Should you have a specific electronic project in mind please reapply for permission.

6. As long as the article is embedded in your thesis, you can post/share your thesis in the University repository.

7. Should your thesis be published commercially, please reapply for permission.

8. Posting of the full article/ chapter online is not permitted. You may post an abstract with a link to the Elsevier website [www.elsevier.com](http://www.elsevier.com), or to the article on ScienceDirect if it is available on that platform.

Kind regards,

**Roopa Lingayath**  
Senior Copyrights Coordinator  
**ELSEVIER** | HCM - Health Content Management

Visit [Elsevier Permissions](#)

**Figure E.3.** Reprinted (adapted) with permission. This article was published in Carbon Capture Science & Technology, Vol. 4, Allan Hua Heng Sim, Xiu Liu & Chunyan Fan, Adsorptive Separation of Carbon Dioxide at Ambient Temperatures in Activated Carbon, 100062, Copyright Elsevier (2022).

